UNIVERSITY OF CRETE

DEPARTMENT OF PHYSICS

PhD THESIS

Demographics of X-ray binaries populations in nearby galaxies and connection with the stellar populations and intrinsic properties of their host galaxy

Charalampos Politakis

Advisor: *Prof.* Andreas Zezas - University of Crete

University of Crete
Department of Physics

PhD THESIS

Doctor of Philosophy
in
ASTROPHYSICS

Charalampos Politakis

Demographics of X-ray binaries populations in nearby galaxies and connection with the stellar populations and intrinsic properties of their host galaxy

Committee

Professor	Andreas Zezas	University of Crete
Professor Emeritus	Nick Kylafis	University of Crete
Professor	Iosif Papadakis	University of Crete
Professor	Vasileios Charmandaris	University of Crete
Assistant Professor	Vassiliki Pavlidou	University of Crete
Research Director	Pablo Reig	Institute of Astrophysics/FORTH
Associate Researcher	Ioannis Antoniadis	Institute of Astrophysics/FORTH

Date of the defence:
9/06/2023

This page intentionally left blank

Abstract

In this thesis, we study the population of discrete X-ray sources in nearby galaxies and in particular, close binary systems emitting in X-rays (X-ray Binaries - XRBs).

It consists of two parts, the first of which studies the distribution of XRBs with a massive stellar companion (HMXBs) in the closest to the Milky Way edge-on galaxy NGC 55, in correlation with the regions of star formation within the galaxy. The result is the estimation of the center of mass transverse velocity of HMXBs as they are displaced from their birth place. Such estimation is the first for a galaxy located outside the Local Group.

The second part studies the population of XRBs in a large sample of nearby galaxies, included in the catalogue of observations from the *Chandra* space observatory. The sample is comprised of 10.099 X-ray sources in 319 nearby galaxies of all morphological types and intrinsic properties such as metallicity, star formation rate and stellar mass. We construct the X-ray Luminosity function (XLF) of XRBs, and using power-law models we estimate the emerging scaling relations with the intrinsic properties of the host galaxies.

This is the most complete study of populations of XRBs in the literature, containing the largest sample of X-ray sources and galaxies. The results presented in the thesis, also affect the binary population synthesis models in constraining the parameter space of the physical processes involved in the evolution of XRBs.

Της παγε ιντεντιοναλλψ λεφτ βλανκ

Περίληψη

Στη διατριβή αυτή μελετώνται οι πηγές εκπομπής ακτίνων-Χ σε κοντινούς γαλαξίες και ειδικότερα σε κοντινά διπλά συστήματα εκπομπής ακτίνων-Χ (X-ray binaries - XRBs).

Αποτελείται από δυο μέρη, το πρώτο από τα οποία αναφέρεται στη μελέτη της κατανομής των XRBs με συνοδό μεγάλης μάζας (HMXBs) στο γαλαξία NGC 55 σε σχέση με τη κατανομή των περιοχών αστρογέννεσης του γαλαξία. Η μελέτη αυτή οδήγησε στην εκτίμηση της μέσης ταχύτητας απομάκρυνσης των συστημάτων αυτών από τις περιοχές δημιουργίας τους. Αυτή είναι η πρώτη τέτοια εκτίμηση σε γαλαξία εκτός της τοπικής ομάδας γαλαξιών.

Το δεύτερο μέρος της διατριβής αφορά τη συστηματική μελέτη των πληθυσμών διπλών συστημάτων εκπομπής ακτίνων-Χ σε ένα μεγάλο δείγμα κοντινών γαλαξιών με βάση τον κατάλογο πηγών ακτίνων-Χ από το διαστημικό παρατηρητήριο *Chandra*. Το συνολικό δείγμα αποτελείται από περισσότερες από 10.099 πηγές σε 319 γαλαξίες που καλύπτουν όλο το εύρος μορφολογικών τύπων, μεταλλικότητας, ρυθμού αστρογέννεσης και αστρικών μαζών που απαντώνται στο κοντινό μας Σύμπαν.

Με βάση αυτά τα δεδομένα, κατασκευάζεται η κατανομή λαμπρότητας των διπλών συστημάτων εκπομπής ακτίνων-Χ σε γαλαξίες διαφορετικών μορφολογικών τύπων και μοντελοποιείται με νόμους δύναμης, από όπου προκύπτουν οι σχέσεις του αριθμού των διπλών συστημάτων εκπομπής ακτίνων-Χ με τον ρυθμού αστρογέννεσης, της αστρικής μάζας και της μεταλλικότητας των γαλαξιών.

Αυτή είναι η πιο ολοκληρωμένη μελέτη του είδους της χρησιμοποιώντας το μεγαλύτερο δυνατό δείγμα γαλαξιών και πηγών ακτινών-Χ και αποτελεί σημείο αναφοράς για μελέτες των πληθυσμών διπλών συστημάτων εκπομπής ακτίνων-Χ. Αποτελεί επίσης σημείο αναφοράς και στην αξιολόγηση των θεωρητικών μοντέλων σχηματισμού και εξέλιξης διπλών συστημάτων εκπομπής ακτίνων-Χ δίνοντας σημαντικές πληροφορίες στο κατά πόσο τέτοιου είδους μετρικές μπορούν να χρησιμοποιηθούν για να καταννοήσουμε τους μηχανισμούς εξέλιξης πληθυσμών διπλών συστημάτων εκπομπής ακτίνων-Χ.

This page intentionally left blank

Dedication

To my wife and soul mate Κική and to my beautiful daughters Έλλη, Δήμητρα, Λήδα. Sources of immense happiness and hope.

This page intentionally left blank

Declaration

I hereby declare that the work in this thesis is that of the candidate alone, except where indicated below.

Chapter 2: is published in the *"Monthly Notices of the Royal Astronomical Society"* as: *Vertical distribution of HMXBs in NGC 55: constraining their centre-of-mass velocity, Babis Politakis, Andreas Zezas, Jeff J Andrews, Stephen J Williams, Monthly Notices of the Royal Astronomical Society, Volume 493, Issue 4, April 2020, Pages 5369–5381*

and in the *"Proceedings of the International Astronomical Union"* as:
High-mass X-ray Binaries: Illuminating the Passage from Massive Binaries to Merging Compact Objects. Proceedings of the International Astronomical Union, Volume 346, pp. 358-361

Chapter 3: Is a paper in preparation, co-authored with *Andreas Zezas*

This page intentionally left blank

Acknowledgments

I thank professor Andreas Zezas for his guidance and support. A pillar of wisdom.

I also thank the Astrophysics and Space Physics section of the Department of Physics at the University of Crete for providing and promoting an intellectual haven.

This page intentionally left blank

Contents

This page intentionally left blank

List of Tables

This page intentionally left blank

List of Figures

This page intentionally left blank

Abbreviations

AGN	Active galactic nuclei
BH	Black hole
CCSN	Core Collapse supernova
CO	Compact Object
CSC	*Chandra* Source Catalogue
HMXB	High-Mass X-ray binary
IMXB	Intermediate-mass X-ray binary
LMXB	Low-mass X-ray binary
NS	Neutron star
RLO	Roche-lobe Overflow
SFH	Star Formation History
SN	Supernova
SFR	Star-formation rate
sSFR	Specific star-formation rate
XLF	X-ray luminosity function
XRB	X-ray Binaries

This page intentionally left blank

1 Introduction

1.1 Importance of XRBs

X-ray binaries (XRBs) are close binary systems (close enough that their gravitational attraction causes them to orbit each other around a common center of mass and under specific circumstances exchange mass) identified by their emission in the X-ray region of the spectrum. The one member (primary) of the X-ray binary is a compact object (white dwarf, neutron star, black hole) accreting material from its companion member (secondary), a non-degenerate star.

An XRB is therefore the evolutionary outcome of two interacting stars engaged in a series of astrophysical phenomena that lead to the emission of X-rays. The observation of XRBs and the subsequent estimation of their orbital and physical characteristics (e.g. orbital period, eccentricity, inclination, masses of stars, distance from star-forming regions, space velocity) provides a unique laboratory for understanding the nature of astrophysical objects and extreme physical processes such as: The evolution of binary

systems (since the majority of stars are members of such systems), the fundamental physics that governs compact objects, accretion and emission of high-energy radiation, compact object mergers that lead to the emission of Gamma Ray Bursts (GRB) and Gravitational Waves (GW), heating of the intergalactic medium (IGM) and formation of galaxies.

The statistical analysis of XRB populations in nearby galaxies in correlation with the properties of the stellar populations of their host galaxy, is useful in binary population synthesis models. These models follow the evolution of a very large population of individual binary systems and examine the parameter space of all the physical processes involved. The outcome is the production of various metrics such as: the X-ray Luminosity Function (XLF) of the population of XRBs (normalised to the star formation rate or the stellar mass of the host galaxy) as a function of X-ray luminosity, the compact object mass distribution, the distribution of the orbital period and the eccentricity, the number of XRBs.

1.2 Categories and characteristics of XRBs

XRBs are "typically" classified according to the mass of the secondary (companion) star. XRBs with a companion mass above $\sim 8\ M_{\odot}$ are classified as High Mass X-ray Binaries (HMXBs), while those with a companion mass less than $\sim 1\ M_{\odot}$ are classified as Low Mass X-ray Binaries (LMXBs). XRBs with a companion mass greater than $\sim 1\ M_{\odot}$ and less than $\sim 8\ M_{\odot}$ are classified as Intermediate Mass X-ray Binaries (IMXBs) the population of which, is theoretically expected and observationally confirmed to be much scarcer.

XRBs are detected from the X-ray emission of the material that is lost from the secondary and accreted from the primary (compact object) according to two mechanisms, **Roche-lobe overflow** (RLOF) and **wind-driven accretion**.

The orbital characteristics of close binary systems are determined by the masses of the stars and by the forces due to the mutual gravitational interaction and orbital motion. The two aforementioned forces are described by the Roche model which defines equipotential surfaces (lobes) around the stars and Lagrangian points where forces cancel out. If material from one star fills its Roche lobe, mass can flow through the 1st Lagrangian point L1 located at the intersection of the lobes of the two stars, from one star to the other in a process named **Roche-lobe overflow** (RLOF). This is the driving mechanism for all LMXBs and for few HMXBs with very short orbital periods.The radius R_L of the Roche lobe as a function of the mass ratio q and the separation α between the two stars is given by (Eggleton 1983):

$$\frac{R_L}{\alpha} = \frac{0.49q^{2/3}}{0.6q^{2/3} + ln(1 + q^{1/3})} \tag{1.1}$$

The ratio q of the initial masses of a binary is defined as $q = M_2/M_1$ where M_1 ($>M_2$) is

(by definition) the mass with the greater value, of the star that evolves first and becomes the primary.

Even if the stars are not close enough for RLO to occur, material is lost from the secondary through stellar wind and captured by the primary in a process named **wind-driven accretion** (Bondi & Hoyle 1944). This mechanism is relevant for most HMXBs but not for LMXBs, because such winds are driven by radiation pressure on absorption lines and are strong enough for massive O and B type stars. The wind of material leaving uniformly in all directions from the secondary's surface will accrete onto the primary only if it is within a critical distance r_{acc} of the compact object, thereby forming an accretion cylinder. The accretion radius r_{acc} is calculated by noting that material will only be accreted if it has a kinetic energy less than the potential energy in the vicinity of the compact object M_c (Frank *et al.* 2002):

$$r_{acc} = \frac{2GM_c}{v_{rel}^2} \tag{1.2}$$

where $v_{rel}^2 = v_{orb}^2 + v_w^2$ is the relative velocity of the accreted material with respect to the compact object, v_{orb} is the orbital velocity of the compact object, and v_w is the wind velocity.

The compact object primary in XRBs is either a neutron star or a black hole. Observations and theoretical calculations of dense matter indicate that neutron stars cannot be more massive than $\sim 2.5\ M_\odot$ (Lattimer 2012), therefore compact objects with masses larger than $2.5\ M_\odot$ are considered as black holes. Neutron stars in XRBs have magnetic fields among the highest found in the Universe, high enough to influence the accretion process. For HMXBs, observations estimate magnetic fields B $\sim 10^{11}$ to 10^{12} G, and for LMXBs magnetic fields B $\sim 10^8$ to 10^{10} G, significantly smaller than those found in HMXBs (Revnivtsev & Mereghetti 2015).

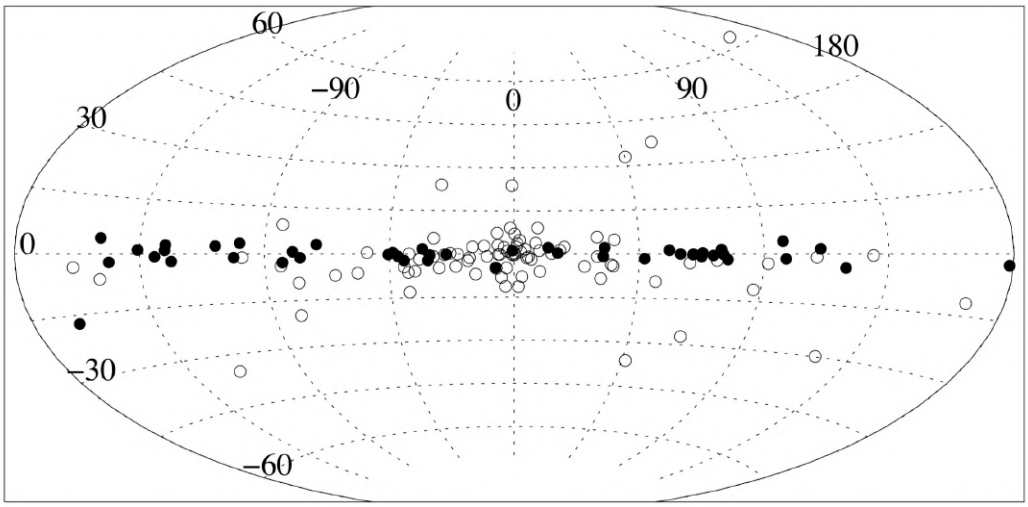

Figure 1.1: Distribution of LMXBs (open circles) and HMXBs (filled circles) in the Galaxy. HMXBs are concentrated towards the Galactic Plane and LMXBs are clustering in the Galactic bulge (Grimm *et al.* 2002)

.

HMXBs are typically located in star-forming regions (Grimm *et al.* 2003, Fabbiano 2006, Persic & Rephaeli 2007), such as galaxy spiral arms, galaxy disks and massive, young stellar clusters and are associated with the young stellar population of the galaxy. LMXBs are located in greater galactic latitudes, in the bulge and in globular clusters, an indication that they are associated with the older stellar population of the galaxy. Figure 1.1 shows the distribution of Galactic HMXBs and LMXBs. HMXBs are concentrated towards the Galactic plane where there is increased star formation activity, and LMXBs are clustering in the Galactic bulge (Grimm *et al.* 2002).

1.2.1 HMXBs

There are two main types of HMXBs, the first type, discovered by Schreier *et al.* (1972) and Webster & Murdin (1972), is that of the **supergiant HMXBs** (SGXRBs). In SGXRBs the companions are massive stars that have evolved from the main sequence. They have mass-loss rates between 10^{-6} and 10^{-8} $M_{\odot}$ yr^{-1}, while the compact object is either a neutron star or a black hole. From the catalogue of Liu *et al.* (2006) for the

XRBs in the Milky Way, the average mass of the companion stars in SGXRBs is ~ 20 $M_{\odot}$, while the average orbital period of SGXRBs is 8.5 days.

They are persistent X-ray sources, powered by the capture of matter from the strong stellar wind of the supergiant companion (wind-driven accretion). There are also a few systems undergoing stable RLOF with higher mass transfer rates than their wind-fed analogs, resulting in generally higher X-ray luminosities compared to wind-fed systems. Table 1.1 presents the observed orbital characteristics of 10 SGXRBs. The first three (LMC X-4, Cen X-3, and SMC X-1) due to their relatively high X-ray luminosity and small P_{orb} are considered prime candidates for being RLOF systems.

The second type, is that of the **B-emission X-ray Binaries** (BeXRBs), discovered in 1975 with the Ariel V satellite, and first recognized and explained as a separate class by Maraschi *et al.* (1976). In BeXRBs, the companions are non-supergiant, fast-rotating main sequence O/B-type stars that do not fill their Roche lobes and show emission-line spectrum (Reig 2011). The origin of the optical emission lines is attributed to an equatorial decretion disk, fed from material expelled from the rapidly rotating Be-star (Porter & Rivinius 2003). X-ray outbursts are observed when the compact object passes through the Be-star disk, accreting from the low-velocity and high-density wind (Okazaki *et al.* 2013). The primary is typically a neutron star (the only verified black hole BeXRB is MWC 656, e.g. Casares *et al.* 2014) that receives a substantial kick at birth (see Section 1.3.4), as indicated by the large eccentricities of BeXRBs (Table 1.1). From the catalogue of Liu *et al.* (2006) for the XRBs in the Milky Way, the average mass of the companion stars in BeXRBs is ~ 14 $M_{\odot}$, while the average orbital period of BeXRBs is 89 days.

BeXRBs in comparison with SGXRBs (Table 1.1), have larger orbital periods and eccentricities while their X-ray luminosity is transient (modulated either by the periastron passage or the tidal disruption of the Be-star disk). Two types of X-ray outbursts are identified in BeXRBs (Figure 1.2):

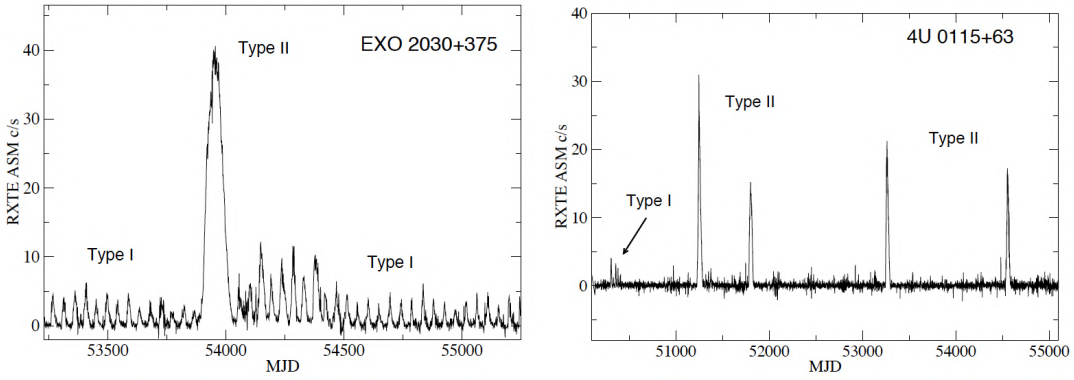

Figure 1.2: Types of X-ray outbursts from the light curves of two BeXRBs, EXO 2030+375 and 4U 0115+63 (Reig 2011)

- Type I, that are regular, (quasi-)periodic, and short-lived (covering a relatively small fraction of the orbital period, 0.2 – 0.3 P_{orb}). The X-ray flux increases by at least two orders of magnitude with respect to the non outburst state (Reig 2011).
- Type II, that are non-regular and long-lived, lasting for a large fraction of an orbital period or even for several orbital periods. The X-ray flux increases significantly with respect to the non outburst state (Reig 2011) and can be close or above the Eddington luminosity (see Section 1.3.6).

Table 1.1: Orbital parameters and characteristics of HMXBs

System	Spectral Type	P_{orb} (days)	α ($R_\odot$)	R_L/α	i (deg)	e	M_c ($M_\odot$)	M_s ($M_\odot$)	R_s ($R_\odot$)
SGXRBs	(1)	(2)	(3)	(4)	(5)	(6)	(7)	(8)	(9)
LMC X-4 (RLO)	O8III	1.4083	14.2	0.59	59.3	0.006	1.57	18	7.4
Cen X-3 (RLO)	O(6-7)II-III	2.0871	14.2	0.63	65.0	<0.0016	1.57	24	11.4
SMC X-1 (RLO)	$B0_{sg}$	3.8922	27.9	0.61	62.0	0.0009	1.21	18	15
4U 1700-377 (Wind)	O6.5Iaf	3.4115	35.0	0.69	62.0		1.96	46	22
4U 1538-522 (Wind)	B0.2Ia	3.7283	22.0	0.53	67.0	0.18	1.02	16	13
SAX J1802.7-2017 (Wind)	B1Ib	4.5696	33.0	0.61	72.0		1.57	22	18
XTE J18f55-026	B0Iaep (Wind)	6.0724	40.0	0.63	71.0	0.04	1.41	21	22
Vela X-1 (Wind)	B0.5Ia	8.9643	59.6	0.59	72.8	0.0898	2.12	26	29
EXO 1722-363 (Wind)	B0-B1Ia	9.7403	52.0	0.58	68.0	<0.19	1.91	18	26
OAO 1657-415 (Wind)	B0-6sg	10.4474	53.1	0.52	67.9	0.1033	1.74	17.5	25
BeXRBs									
4U 0352+309 (X Per)	O9.5IIIe-B0Ve	250				0.11		14.6	
GRO J1008-57	O9e-B1e	247.5				0.66		14.6	
4U 0115+634	B0.2 Ve	24.33				0.34		14	
XTE J1946+274	B0-1 IV-Ve	169.2				0.33		13	
EXO 2030+375	B0e	46.03				0.41		14.5	

Column description: (1) Spectral type of the companion, (2) Orbital period in days, (3) Separation of the two stars, (4) Ratio between the Roche-lobe radius and the separation of the two stars, (5) Inclination angle of the system, (6) Eccentricity, (7) Mass of compact object (primary), (8) Mass of the secondary (companion), (9) Radius of the secondary.

1.2.2 LMXBs

In LMXBs, the secondaries are faint low-mass evolved stars of spectral type G, K, or M that are less massive than the primary compact object. LMXBs have shorter orbital periods than HMXBs. For the XRBs in the Milky Way, the average orbital period of LMXBs is $\sim$ 2 days (Liu *et al.* 2006) and in contrast with HMXBs where the compact object in the majority of the systems is a neutron star, there are many LMXBs harboring a black hole. The companion star has evolved to fill its Roche lobe and material is transferred through the inner Lagrangian point, L1, onto the compact object (RLOF). Table 1.2 presents the observed orbital characteristics for some of the LMXBs in the Ritter Low-Mass X-Ray Binaries Catalog (Ritter & Kolb 2003).

1.2.3 IMXBs

IMXBs are rare astrophysical objects, very few of which are discovered (and confirmed). The duration of the X-ray emission phase in IMXBs is believed to be very short compared to HMXBs and LMXBs. This is because material is transferred via RLO (as in LMXBs) and due to the large mass of the secondary is thought to be unstable and therefore very rapid and possibly leads to a common envelope phase (see Section 1.3.3. Investigations into the IMXB evolutionary path, suggest that many of the current LMXBs descended from IMXBs (Podsiadlowski & Rappaport 2000) and also the observed population of binary millisecond pulsars with heavy CO or ONeMg white dwarf companions may have descended from the evolutionary channel of IMXBs (Tauris *et al.* 2000). Table 1.3 presents three candidate IMXBs, including Her X-1 which is considered the prototype for IMXBs. The orbital periods are short (comparable to LMXBs) and the compact object in the case of 3XMMJ004301.4+413017 and Her X-1 is a neutron star which is less massive than the companion star. XTE J1819.3-2525 is a black hole IMXB with a relatively massive companion.

Table 1.2: Orbital parameters and characteristics of LMXBs

System	Spectral Type	P_{orb} (days)	i (deg)	M_c ($M_\odot$)	M_s ($M_\odot$)
	(1)	(2)	(3)	(4)	(5)
V822 Cen	K5-M1/5	0.6291	39	1.14	0.230
LZ Aqr	K7-8/5	0.2482	72.5	1.30	0.600
AC 211		0.7130	90	1.40	0.150
V395 Car	K0/3	9.0026	82.2	1.44	0.350
V1341 Cyg	A8-F0/3	9.8445	62.5	1.71	0.580
GR Mus		0.1639	69	1.92	0.650
V691 CrA		0.2321	82.5	1.97	0.500
V518 Per	M0-2/5	0.2122	45	3.97	0.460
MM Vel	K7-M0/5	0.2852	78	4.40	0.600
V616 Mon	K5/5	0.3230	51	6.64	0.400
V2107 Oph	K5/5	0.5210	70	6.65	0.450
GU Mus	K3-4/5	0.4326	54	6.95	0.850
KV UMa	K5/5	0.1699	73.5	7.29	0.180
QZ Vul	K3-6/5	0.3441	64	7.50	0.330
BW Cir	G0-5/3	2.5445	79	7.60	0.900
V381 Nor	K3/3	1.5420	74.7	9.10	0.300
V404 Cyg	K3/3	6.4714	56	10	0.650
V1487 Aql	K/3	33.9000	66	10.1	0.470

Column description: (1) Spectral type of the companion, (2) Orbital period in days, (3) Inclination angle of the system, (4) Mass of compact object, (5) Mass of the secondary. All values derived from the Ritter Low-Mass X-Ray Binaries Catalog (Ritter & Kolb 2003).

Table 1.3: Orbital parameters and characteristics of IMXBs

System	Spectral Type	P_{orb} (days)	i (deg)	M_c ($M_\odot$)	M_s ($M_\odot$)	Refs.
	(1)	(2)	(3)	(4)	(5)	
XTE J1819.3-2525	B9 III	2.81730	60−71	8.7−11.7	5.49−8.14	[1]
3XMMJ004301.4+413017		1.27		1.40	1.5	[2]
Her X-1	A9-B	1.7		1.40	~ 2	[3]

Column description: (1) Secondary spectral type, (2) Orbital period in days, (3) Inclination angle, (4) Compact object mass, (5) Secondary mass.
References: [1] Orosz *et al.* (2001) [2] Karino (2016) [3] Bildsten *et al.* (1997)

1.3 Observations of the evolutionary stages of XRBs

The X-ray emission phase of a close binary system is the outcome of several evolutionary stages. Collecting observational data for X-ray binaries in different stages, provides the necessary insight for understanding the physical processes involved in each stage and create the model that optimally describes the evolution of XRBs. In this section we focus on the observational data of the corresponding evolutionary stages of XRBs, as well as aspects of the fundamental theoretical background.

1.3.1 Evolution of LMXBs and HMXBs

Figure 1.3 and Figure 1.4 show the evolutionary stages of HMXBs and LMXBs respectively, from the initial binaries at ZAMS (Zero Age Main Sequence), to the X-ray emission stage, and further on until both stars have evolved and the binaries are comprised of two compact objects (adopted from Tauris & van den Heuvel 2006).

For the HMXB evolution in Fig. 1.3, the starting point is a binary system with main-sequence massive stars having an initial orbital period of 100 days. The more massive star (primary) evolves more rapidly and after core H-burning expands to become a supergiant, filling its Roche lobe and initiating RLOF conservative mass transfer to the secondary. The outcome of the first stage of mass transfer is a binary in which the almost naked helium core of the primary is in a wide orbit (the orbital period has increased) around a secondary that has gained appreciably in mass and angular momentum. The core of the primary continues its evolution, and after a short time explodes as a supernova, leaving a neutron star of 1.4 $M_{\odot}$. The sudden mass loss increases the orbital period and eccentricity of the binary. The massive secondary evolves, finishes core H-burning, and expands to become an O/B supergiant driving a strong stellar wind that is accreted from the neutron star (wind-fed accretion) and the binary appears as an HMXB. Mass transfer proceeds at such a huge rate that the neutron star is totally engulfed by the

expanding envelope of the secondary, wherein the neutron star and the He-core of the secondary spiral in towards each other inside a common envelope (see Section 1.3.3). Friction transfers angular momentum and energy from the orbital motion to the common envelope which is sufficient to expel the envelope. After the common envelope phase the binary consists of the primary neutron star in a very close orbit (at $\sim 10^{-1}$ days, dramatically reduced from $\sim 10^{3}$ days before the common envelope stage) around the He-core of the secondary. Continued evolution of the He core of the secondary will fill its Roche lobe and leads to a second supernova explosion, which in turn leads to the formation of a radio pulsar binary like PSR1913 + 16, consisting of two neutron stars in an eccentric orbit.

For the LMXB evolution in Fig. 1.4, the starting point is a binary system with main-sequence stars with a very small mass ratio $q = M_2/M_1 = 1.6/15.0 \sim 0.1$ having an initial large orbital period of 1,500 days. The massive star (primary) evolves rapidly and after core H-burning expands to become a supergiant, filling its Roche lobe and initiating RLO conservative mass transfer to the secondary. The primary keeps on overflowing its own Roche lobe with its envelope continuing to expand engulfing the secondary, thus forming a common envelope. After the common envelope is expelled, the binary consists of the He-core of the primary in a very close orbit (at 0.75 days, dramatically reduced from the 1930 days before the common envelope stage) around the secondary 1.6 $M_{\odot}$ main-sequence star which is hardly affected by the spiral-in process, and emerges pretty much as it entered. The He-core of the primary continues its evolution, and after a short time explodes as a supernova, leaving a neutron star of 1.3 $M_{\odot}$. The sudden mass loss increases the orbital period and eccentricity of the binary. The secondary evolves away from the main sequence, expands into a (sub)giant in a time scale $>$ 2 Gyr, filling its Roche lobe and initiating mass transfer, where the material is accreted from the primary neutron star (RLOF accretion) and the binary appears as an LMXB. The end of the LMXB mass transfer stage which lasts $\sim 4\times 10^{8}$ yr, leads to

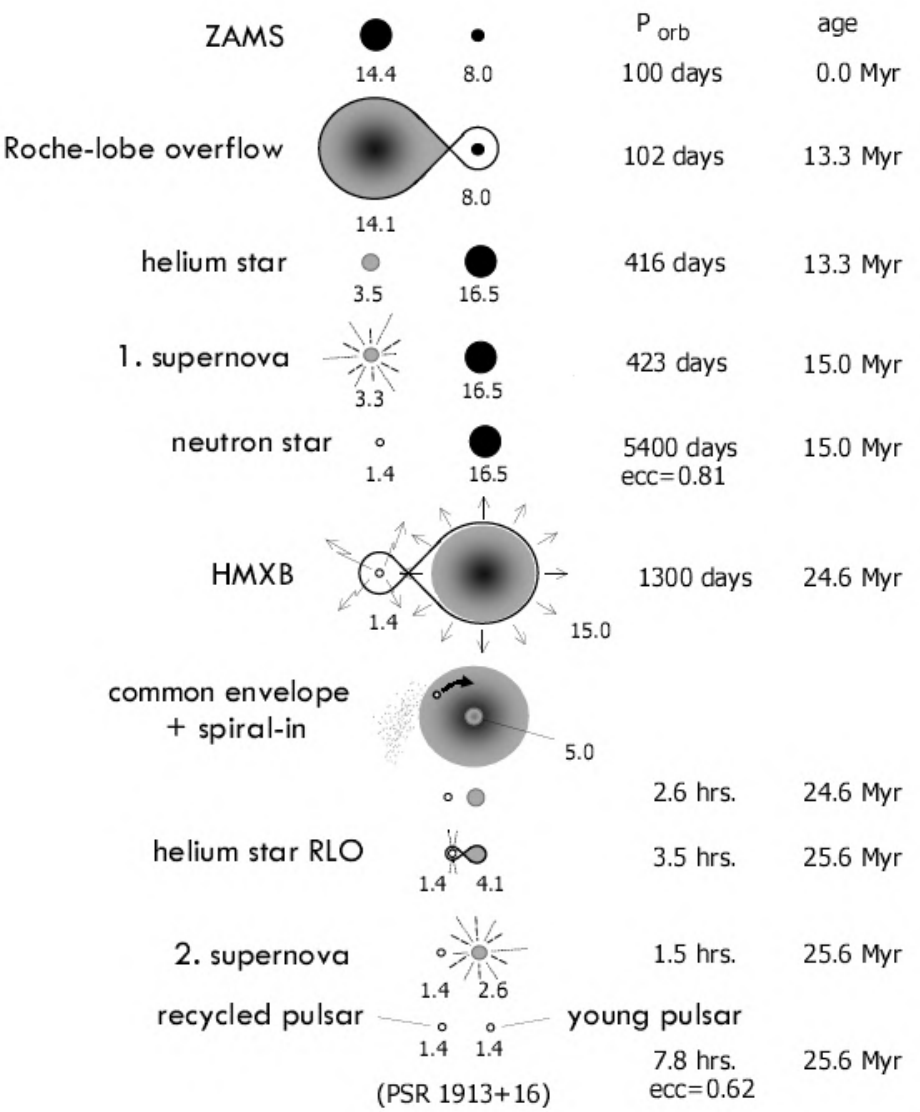

Figure 1.3: Evolutionary stages of a HMXB (Tauris & van den Heuvel 2006)

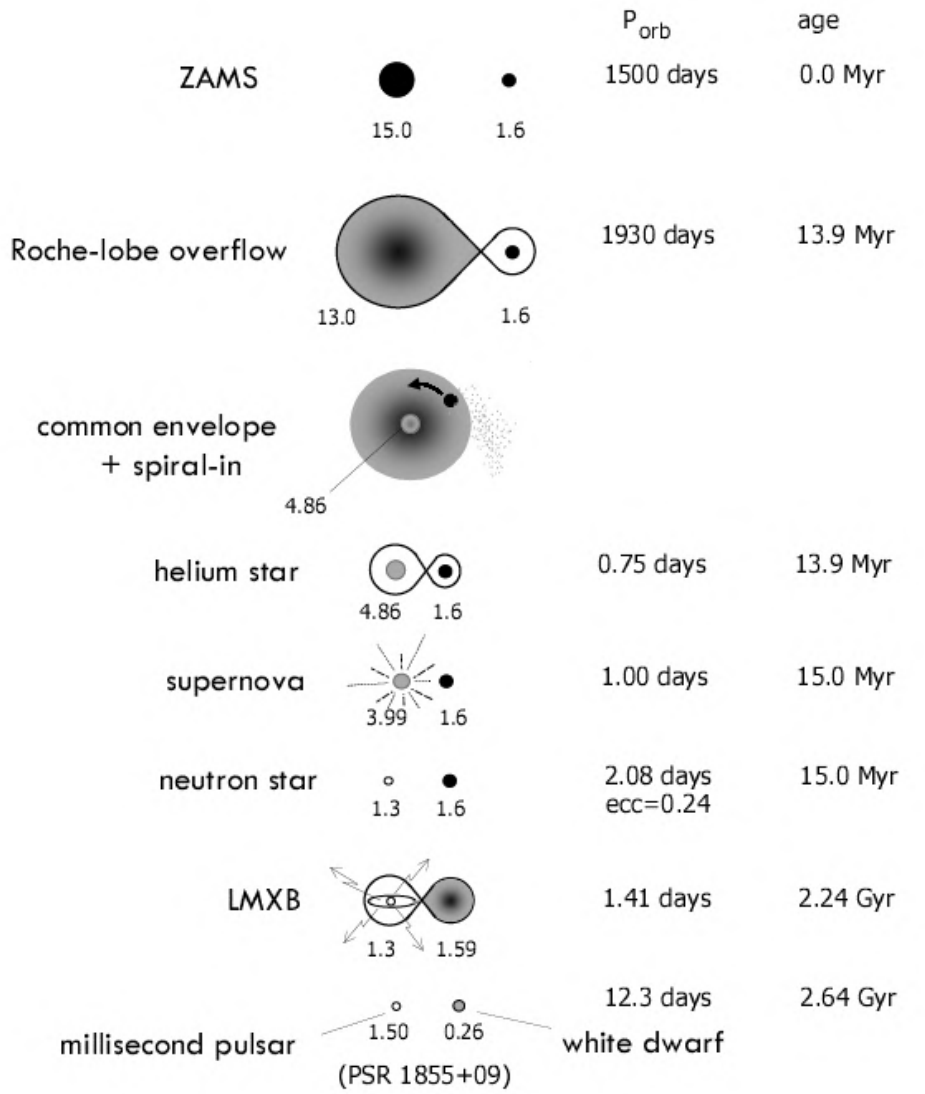

Figure 1.4: Evolutionary stages of a LMXB (Tauris & van den Heuvel 2006)

the formation of a binary binary like PSR 1855+09 comprised of a millisecond pulsar (which is the primary neutron star that has gained mass and angular momentum) and a low-mass white dwarf companion (the remnant of the secondary) in a wide, circular orbit.

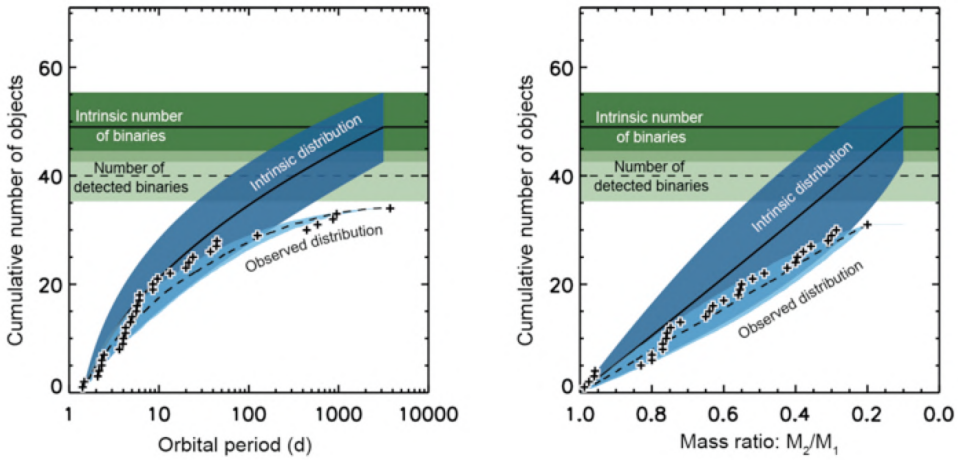

Figure 1.5: Cumulative distribution of orbital periods (left panel) and of mass ratios (right panel). The horizontal solid lines and the associated dark green areas indicate the most probable intrinsic number of binaries (49 in total) and the 1σ uncertainty. The horizontal dashed lines and the associated dark green areas indicate the most probable simulated number of detected binaries which agrees with the observed number of binaries (40 in total). Crosses show the observed systems with known periods (34 in total) and mass-ratios (31 in total) (Sana *et al.* 2012)

.

1.3.2 Initial binaries

The initial mass of the primary (from which the compact object is formed) in XRBs, is that of a massive O or B type star. The initial mass of the secondary can be of any value, from $\sim$1 $M_{\odot}$ up to the mass of the primary. In order to quantify the fraction of massive stars involved in a binary interaction and identify the mass ratios and orbital periods of the binaries, Sana *et al.* (2012) observed massive Galactic O type stars, with the results (Figure 1.5) indicating that:

- 71% of all stars born as O-type interact with a companion.
- There is a strong preference for close pairs.
- There is a preference for a uniform distribution of the mass ratio for binaries with orbital periods up to about nine years.

1.3.3 Expansion of the primary

Depending on the size of their stellar radii compared with the size of their Roche lobes, the binary systems can be characterized as:

- Detached: both stars are within their Roche lobes.
- Semi-detached: one star has expanded to fill its Roche lobe.
- Contact: both stars expand and fill their Roche lobes, touching at the L1 point. A common envelope is created that extends up to L2.

When the radius of the more massive star (that evolves first since it has the shortest nuclear timescale) reaches the value of R_L (see Eq. 1.1) then the star fills its Roche lobe (and the system becomes a semi-detached binary), hydrostatic equilibrium is no longer possible in the vicinity of the inner Lagrangian point L1 and material is transferred into the Roche lobe of the secondary.

Depending on the evolutionary stage of the primary when it fills its Roche lobe, three cases of mass transfer can be distinguished for the expanding star: it expands while on the main sequence (Case A), it expands after hydrogen exhaustion (Case B), it expands after helium exhaustion (Case C). The respective changes in the radius of the expanding star are shown in Figure 1.6 for a $5M_{\odot}$ star.

In a **Case A** scenario, for the primary star to fill its Roche-lobe while on the main sequence, the separation α with the secondary must be small (and consequently the orbital period of the system must be very short) since the increase of the radius at the latter stages of core hydrogen burning is small compared with cases B and C (Figure 1.6). Assuming conservative mass transfer (i.e. that no mass or angular momentum is removed from the system), it is possible to determine the mass transfer rate (or the mass loss of the primary) $\dot{M}_1$, if the mass and the period derivative $\dot{P}$ can be measured.

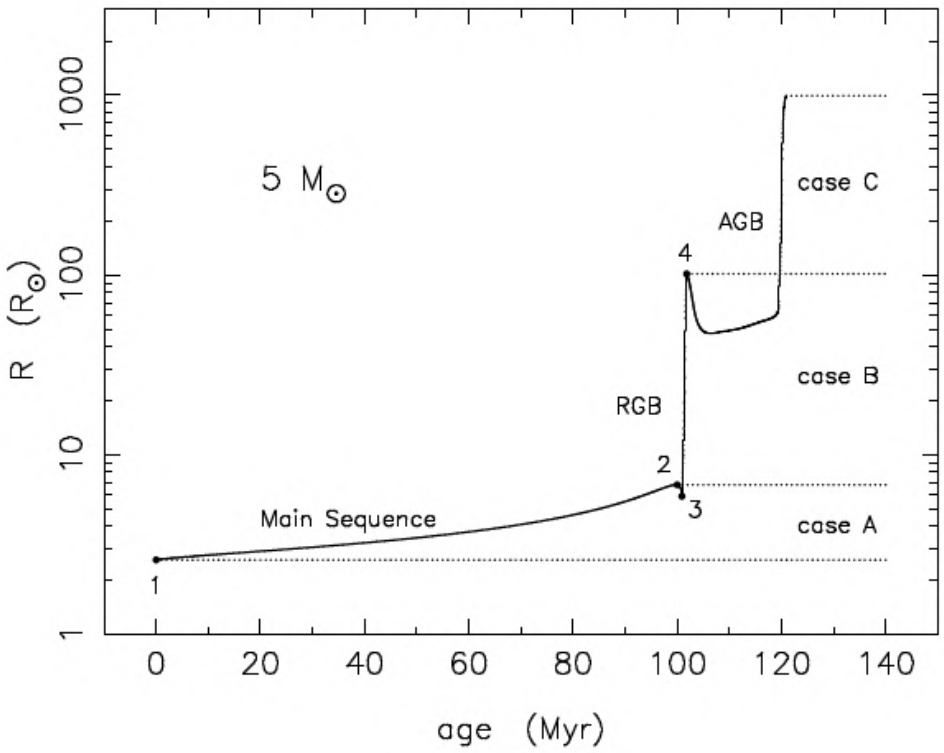

Figure 1.6: Evolutionary change of the radius of a $5M_{\odot}$ star according to cases A, B and C Adopted from Tauris & van den Heuvel (2006)

Using Kepler's law:

$$\frac{\dot{P}}{P} = 3\left(\frac{M_1}{M_2} - 1\right)\frac{\dot{M}_1}{M_1} \tag{1.3}$$

The aforementioned scenario is observed in Algol-variable binaries some of which are presented in Table 1.4. In almost all systems the less massive primary has the largest radius. For S Equ where observations for the period derivative $\dot{P}$ are available, the derived mass transfer rate $\dot{M}_1$ is $3.97\times\ 10^{-8}\ M_{\odot}\ \mathrm{yr}^{-1}$ (Soydugan *et al.* 2007).

In a **Case B** scenario, the primary is more extended (than in Case A) since its radius increases significantly (Figure 1.6). As a result, mass is transferred at a fairly high rate until the ignition of helium, at which point it stops and the primary contracts and

Table 1.4: Orbital parameters and characteristics of Algol variables

System	Spectral Type	P_{orb} (days)	$\dot{P}$ (s/yr)	M_1 ($M_\odot$)	M_2 ($M_\odot$)	R_1 ($R_\odot$)	R_2 ($R_\odot$)	α ($R_\odot$)
	(1)	(2)	(3)	(4)	(5)	(6)	(7)	(8)
β Per	B8V + K0IV	2.87		0.70	3.17	3.48	2.73	39.36
S Equ	B8V + G8IV	3.43	0.102	0.45	3,24	3.24	2.74	14.8
TT Au	B2V + B4	1.33		5.4	8.1	4.2	3.9	12.14
U CrB	B6V + F8III	3.45		1.46	4.74	4.83	2.79	17.6
U Her	B2.5V + B8IV	2.05		2.79	7.88	4.26	4.93	14.95
RW Tau	B8Ve + K0IV	2.77		0.6	2.43	3.00	2.27	11.94
U Cep	B8Ve + G8IV	2.49		2.5	4.04	4.68	2.57	14.46
AQ Cas	B0.5II + B3II	11.72		12.56	17.63	23.55	13.48	67.59
RZ Sct	B2II + A0II	15.190	1	2.49	15.8	15.9	15.8	62.43

Column description: (1) Spectral type of stars, (2) Orbital period in days, (3) Period derivative (4) Mass of primary, (5) Mass of secondary, (6) Radius of primary (7) Radius of secondary, (8) semi-major axis
References [row number]: [1] Baron *et al.* 2012, [2] Soydugan *et al.* 2007, [3] Surkova & Svechnikov 2004, [4] Yerli *et al.* 2003, [5] Kolbas *et al.* 2015, [6] Malkov 2020, [7] Surkova & Svechnikov 2004,[8] Sipahi *et al.* 2013, [9] Erdem & Öztürk 2014

Table 1.5: Orbital parameters and characteristics of β Lyr variables

System	Spectral Type	P_{orb} (days)	M_1 ($M_\odot$)	M_2 ($M_\odot$)	R_1 ($R_\odot$)	R_2 ($R_\odot$)	α ($R_\odot$)
	(1)	(2)	(3)	(4)	(5)	(6)	(7)
β Lyr	B6-8II + B	12.94	2.97	13.16	15.2	6	
μ^1Sco	B0V + B2V	1.44	4.6	8.3	4.6	3.9	12.6
V716 Cen	B5.5V + A2V	1.49	2.39	5.68	3.36	4.08	11.0
V Pup	B1V + B3	1.45	6.11	12.45	4.59	5.78	14.31
TU Mus	O7V + O8V	1.39	16.8	10.5	7.2	5.7	17.34

Column description: (1) Spectral type of stars, (2) Orbital period in days, (3) Mass of primary, (4) Mass of secondary, (5) Radius of primary (6) Radius of secondary, (7) semi-major axis
References [row number]: [1] Mennickent *et al.* 2006, [2] Budding *et al.* 2015, [3] Bakis *et al.* 2010, [4] Erdem *et al.* 2021, [5] Penny *et al.* 2008

detaches from its Roche lobe. The primary has now become a helium star, almost entirely deficient of hydrogen. The duration of case B mass-transfer is very short compared to case A, therefore observed examples are rare. Candidate systems currently undergoing case B mass transfer, are β Lyrae binaries. The two component stars are extended giants or supergiants in a close orbit, with their shapes heavily distorted by mutual gravitation forces and there are extensive mass flows from one component to the other (Table 1.5).

In a **Case C** scenario a massive and initially very wide binary undergoes dynamically unstable mass transfer. The increase of the radius of the primary is so large (Figure 1.6) that the expanding envelope engulfs the secondary initiating a phase known as **common-envelope evolution** (CEE). Friction transfers angular momentum and energy from the orbital motion to the common envelope and as a result the orbit shrinks dramatically. The process continues until either enough energy is added to the envelope to expel it, or the orbit shrinks so much that the two stars merge. CEE is expected to be accompanied by a rise in luminosity and could be detected as a transient event, as in the case of the stellar merger V1309 Sco (Nakano *et al.* 2008). Furthermore, the short-lived phase of CEE is proposed as an evolutionary channel for very short-period LMXBs the formation of which requires a substantial loss of orbital energy and angular momentum.

1.3.4 Collapse of the primary

The He-core of the primary continues its evolution, and after a short time explodes as a Core Collapse supernova (CCSN). The envelope mass of the exploding star is expelled and a neutron star or black hole is formed. The binary receives a center of mass kick from mass loss (recoil velocity) that is sometimes referred to as the Blaauw kick (Blaauw 1961) and is given by:

$$v_B = \frac{\Delta M_1}{M'}\frac{M_2}{M} \times \left(\frac{GM}{\alpha}\right)^{1/2} \tag{1.4}$$

where $\Delta M_1 = M_1^{'}$ - M_1 is the difference in mass of the primary M_1, $M^{'} = M_1^{'}$ - $M_2^{'}$ is the post-supernova total mass of the binary and $M = M_1$ - M_2 is the pre-supernova total mass of the binary with separation α. The symmetric mass loss $\Delta M = M^{'}$ - M in a Blaauw kick will increase the eccentricity e and the separation α_f of the post-supernova orbit:

$$e = \frac{\Delta M}{M_1 + M_2 - \Delta M}, \qquad \alpha_f = \frac{1}{1-e}\alpha_i \tag{1.5}$$

For an asymmetric collapse of the core, due to asymmetric mass ejection and/or asymmetric neutrino emission, the newly formed neutron star also receives a (natal) kick that displaces the binary (Kalogera 1996; Brandt & Podsiadlowski 1995). The direction of the kicks is assumed to be isotropic and the kick magnitude is represented from the three Maxwellian distributions presented in Figure 1.7 (Voss & Tauris 2003).

Neutron stars formed in massive binaries are much easier to retain, since the kick momentum given to the neutron star is shared with a massive companion, leading to a much lower systemic velocity for the post-supernova binary. Small natal kicks are also expected when: i) the newly formed compact object is a black hole and ii) instead of

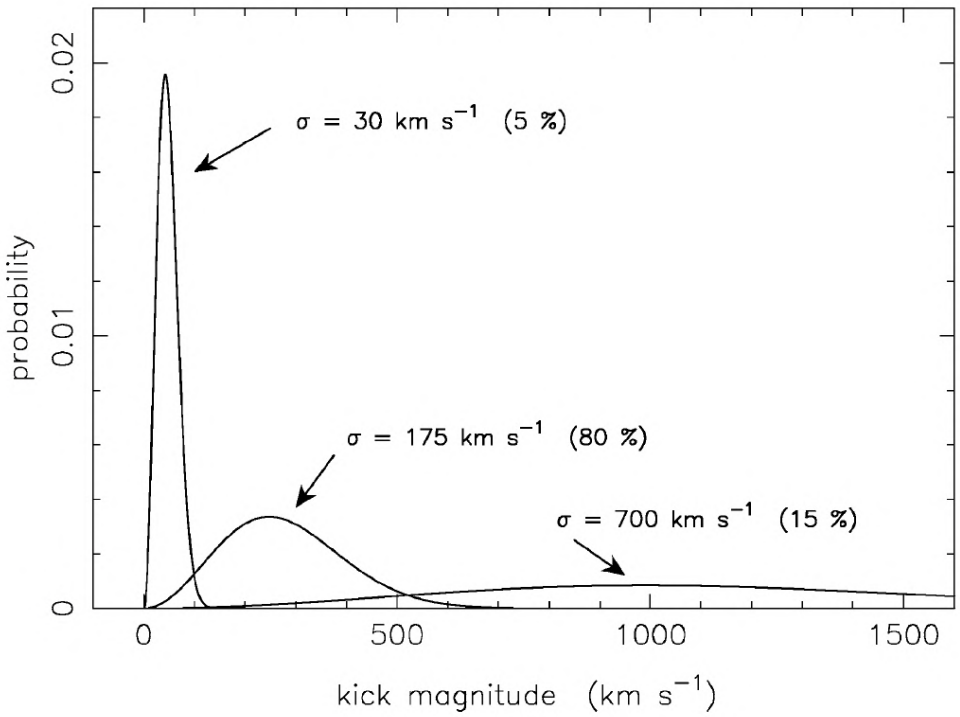

Figure 1.7: A momentum kick is assumed to be imparted to all new-born neutron stars. The kick magnitude is represented from the three Maxwellian distributions shown above (Voss & Tauris 2003)

core collapse, the supernova is caused by electron capture (Linden *et al.* 2009).

1.3.5 X-ray luminosity through accretion

The X-ray luminosity from XRBs completely dominates the X-ray output of galaxies over other discrete sources of X-ray emission within galaxies, such as supernova remnants (SNR), isolated pulsars, and coronally active stars.

If all the kinetic energy of matter that is infalling with mass rate $\dot{M}$ towards a neutron star of mass M and radius R_* is emitted as radiation at the stellar surface, then the accretion luminosity is:

$$L_{acc} = \frac{GM\dot{M}}{R_*} \tag{1.6}$$

In the case of **RLO accretion**, the matter being accreted possesses enough angular momentum that it cannot fall toward the accretor along a straight line and instead forms an accretion disk. For an optically thick disk, the luminosity is (Frank *et al.* 2002):

$$L_{disk} = \frac{1}{2}\frac{GM\dot{M}}{R_*} = \frac{1}{2}L_{acc} \tag{1.7}$$

At each radial distance R, an optically thick disk emits blackbody radiation with a continuous spectrum corresponding to the temperature $T(R)$ at that distance (Frank *et al.* 2002):

$$T(R) = \left\{\frac{3GM\dot{M}}{8\pi\sigma R^3}[1-\left(\frac{R_*}{R}\right)^{1/2}]\right\}^{1/4} = 6.3\times10^5\left(\frac{\dot{M}}{\dot{M}_{Edd}}\right)^{1/4} M_8^{-1/4}\left(\frac{R}{R_*}\right)^{-3/4} \tag{1.8}$$

where $\dot{M}_{Edd}$ is the mass rate for luminosity equal to Eddington luminosity (see Section 1.3.6).

In the case of **wind-driven accretion**, the amount of material accreted by the compact object is given by the amount inside the accretion cylinder that is formed (see Section 1.2) which, for wind material of density ρ and velocity v_w uniformly expelled (with a mass-loss rate $\dot{M}_w$) from a secondary of mass M in a binary with orbital radius α is given by (Frank *et al.* 2002):

$$\dot{M} = \pi r_{acc}^2 v_{rel}\rho = \left(\frac{M_c}{M}\right)^2 \frac{(v/v_w)^4}{[1+(v/v_w)^2]^{3/2}}\dot{M}_w \quad M_\odot yr^{-1} \tag{1.9}$$

1.3.6 Ultraluminous X-ray sources

A measure that provides the maximum emitted luminosity by an object and still remain in hydrostatic equilibrium is the Eddington luminosity L_{Edd}, also referred to as the

Eddington limit. If the luminosity exceeds the Eddington limit, then the radiation pressure drives an outflow that can reduce or cut off the accretion flow. For compact objects of mass M_c the Eddington luminosity is given by:

$$L_{Edd} = 1.3 \times 10^{38} \frac{M_c}{M_\odot} \quad ergs^{-1} \tag{1.10}$$

The mass transfer rate $\dot{M}_{Edd}$ to reach L_{Edd} for a radiative efficiency of the accretion flow $\eta = 0.1$ can be given as:

$$\dot{M}_{Edd} = \frac{L_{Edd}}{\eta c^2} = 2.3 \times 10^{-8} M_c \quad M_\odot yr^{-1} \tag{1.11}$$

For a neutron star with $M_c = 1.4\ M_\odot$, Eq. 1.10 and Eq. 1.11 give $L_{Edd} \sim 2 \times 10^{38}$ erg s^{-1} and $\dot{M}_{Edd} \sim 3.2 \times 10^{-8}\ M_\odot$ yr^{-1}. For a stellar black hole of $10M_\odot$, Eq. 1.10 and Eq. 1.11 give $L_{Edd} \sim 10^{39}$ erg s^{-1} and $\dot{M}_{Edd} \sim 2 \times 10^{-7}\ M_\odot$ yr^{-1}.

Objects that under the assumption of isotropic emission, exceed the Eddington luminosity for a neutron star or a $10M_\odot$ stellar black hole (super-Eddington accretion), are named **Ultraluminous X-ray sources** (ULXs). A question arises as to what are the physical processes for achieving such high values of L and $\dot{M}$?

Super-Eddington luminosities can be achieved in XRBs with black holes greater than $10M_\odot$ as Eq. 1.10 suggests. They are also possible as the result of geometrical beaming of the emitted radiation (therefore the assumption of isotropic emission does not hold) due to the formation of a funnel in the central part of the accretion thick disk (e.g. Kaaret *et al.* 2017).

In another scenario, the super-Eddington ULX luminosities are the result of geometrical beaming of the emitted radiation (therefore the assumption of isotropic emission does not hold) due to the formation of a funnel in the central part of the accretion thick disk (e.g. Kaaret *et al.* 2017).

Super-Eddington rates are possible in two scenarios. The first includes thermal timescale mass transfer in HMXBs (King *et al.* 2001), and the second long lasting transient outbursts in wide orbital separation LMXBs (such as GRS 1915+105, King 2002).

1.4 X-ray Luminosity Functions

As mentioned in Section 1.2, the timescales of evolution between HMXBs and LMXBs are very different. The very short timescale of HMXBs ($\sim 10^7$ yr) makes them a good tracer of recent star formation activity in a galaxy. On the other hand, due to their long timescale ($\sim 10^{10}$ yr), LMXBs display no direct association with to the star forming activity, but are rather associated with the total stellar content of a galaxy.

The first studies of the integrated galactic X-ray emission with the *Einstein Observatory* showed strong correlations between their X-ray luminosity and B-band or K-band luminosity tracing young and old stellar populations respectively (Fabbiano 1989). Subsequent studies with *ROSAT* showed strong correlation of the diffuse, thermal, X-ray luminosity of star-forming galaxies with their B-band luminosity (Stevens & Strickland 1998), also indicating a direct link with young stellar populations.

With the advent of *Chandra*, it became possible to study in detail the connection between the X-ray emission of galaxies and their stellar content. The *Chandra* data reported a linear correlation between the integrated X-ray luminosity from HMXBs and SFR, first in a sample of star-forming galaxies (Grimm *et al.* 2003) and subsequently in an expanded star-forming galaxies sample (e.g. Figure 1.8; Mineo *et al.* 2012a,b, 2014; Lehmer *et al.* 2010). A similar correlation between the integrated X-ray luminosity of LMXBs and stellar mass $M_\star$ in early-type galaxies was also reported (Gilfanov *et al.* 2004; Boroson *et al.* 2011; Zhang *et al.* 2012). Furthermore, joint relations between X-ray luminosity, SFR, and $M_\star$ were introduced, that account for both the HMXB and the LMXB population (Fragos *et al.* 2013b; Lehmer *et al.* 2016).

The spatial resolution of *Chandra* ($0.5''$), enabled the detection of discrete X-ray sources in the local universe and allowed the construction of **X-ray Luminosity Functions** (XLFs) that present the luminosity distribution of XRBs, and study their dependence on the intrinsic properties (star formation rate, stellar mass, metallicity) of the host galaxies. The XLF of HMXBs in star-forming galaxies when normalised by the

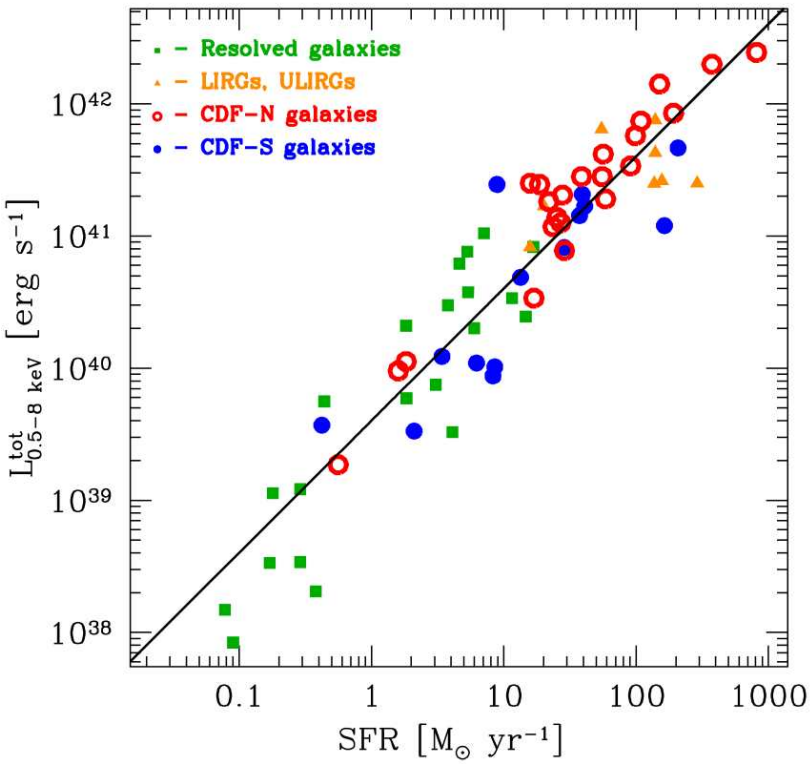

Figure 1.8: X-ray luminosity (0.5–8 keV) as a function of SFR. The solid line represents the scaling relation. Adopted from Mineo *et al.* (2014)

SFR of the host galaxies is described by a single power law model with an index in the range between 1.5 and 1.8 (e.g. Grimm *et al.* 2003; Zezas *et al.* 2007; Mineo *et al.* 2012a; Wang *et al.* 2018; Lehmer *et al.* 2019) and a normalisation constant giving the number of HMXBs per SFR.

The XLF of LMXBs in early-type galaxies when normalised by the $M_\star$ is described by a broken power-law with typical indices between 1.5 and 2.5 above a luminosity break-point L_b at $\sim 3.0 \times 10^{38}$ erg s^{-1}, between 2.0 and 3.0 at lower luminosities and a normalisation constant giving the number of LMXBs per $M_\star$. (e.g. Gilfanov *et al.* 2004; Kim & Fabbiano 2010; Zhang *et al.* 2012; Peacock & Zepf 2016; Lehmer *et al.* 2019).

At the same time, binary population synthesis models which are a key tool for studying the formation and evolution of individual and populations of XRBs, provide

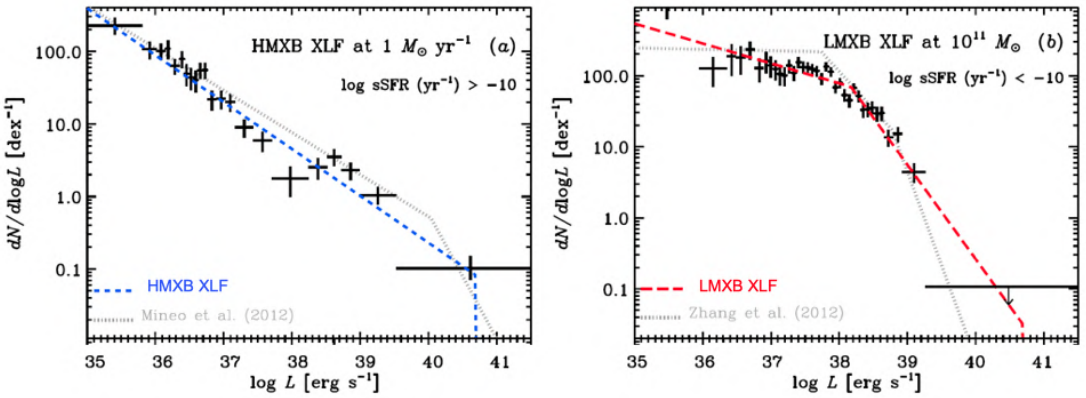

Figure 1.9: Left panel: The blue dashed line presents the completeness-corrected and CXB subtracted HMXB XLF from Lehmer *et al.* (2019). The grey dotted line is the corresponding HMXB XLF from Mineo *et al.* (2012a). Right panel: The red dashed line presents the LMXB XLF from Lehmer *et al.* (2019). The grey dotted line is the corresponding LMXB XLF from Zhang *et al.* (2012). The figure is adopted from Lehmer *et al.* (2019)

theoretical insights based on the observational data. The approach followed in most X-ray binary population synthesis codes (e.g. Belczynski *et al.* 2008) is to follow the evolution of a very large population of individual binary systems with initial parameters (e.g. mass ratio, orbital separation, rotation) sampled from appropriate distributions. In order to predict the X-ray binary populations of a galaxy these models are then convolved with its star-formation history (e.g. Belczynski *et al.* 2004; Belczynski *et al.* 2008; Tzanavaris *et al.* 2013; Olejak *et al.* 2020). Studies began comparing predictions from X-ray binary population synthesis models for different assumptions of initial parameters (e.g. initial mass ratio distribution) or binary evolution parameters (supernova kick velocity distribution, common envelope ejection efficiency, etc.) with the XLFs of X-ray binaries in nearby galaxies. Belczynski *et al.* (2004) constructed the first synthetic XLF of X-ray binary populations for direct comparison with the XLF of NGC 1569, while Fragos *et al.* (2009) constructed the synthetic XLF of LMXBs to compare with observations from the elliptical galaxies NGC 3379 and NGC 4278, using the population synthesis code *StarTrack* (Belczynski *et al.* 2008). Tzanavaris *et al.* (2013) compared synthetic with observed XLFs from a sample of 12 nearby, late-type galaxies, while Zuo

et al. (2013) produced synthetic XLFs of HMXBs in star-forming galaxies. Recently developed models, provide more efficient study of individual systems using state-of-the-art statistical methods and spatially resolved star-formation histories (e.g. *Dart Board* Andrews *et al.* 2018). The aforementioned studies showed that it is possible to constrain X-ray binary evolution parameters, and that generally models for similar parameter values are consistent with the observed XLFs even for different galaxies. In addition, while the population synthesis models depend on several parameters, the comparison with the observed XLFs can constrain only a few of them (most notably the common envelope ejection efficiency and the distribution of binary initial separation).

The XLF constructed from observational data presents the X-ray luminosity emitted from XRBs correlated with stellar populations of varying ages (HMXBs correlated with young and LMXBs with old stellar populations). A question arises as to how the XLF evolves with age. Binary population synthesis models predict that X-ray emission in stellar populations up to $\sim 100\,\mathrm{Myr}$ originates in HMXBs, while older stellar populations are dominated by a declining population of LMXBs (e.g. Figure 1.10, Fragos *et al.* 2013a).

Spatially resolved studies of individual spiral galaxies showed that the XLF of XRBs in different regions of the galaxy become steeper with increasing distance from the center (e.g. Soria & Wu 2003 for the inner and outer disk regions of NGC 5236), which is interpreted as a signature of the 'aging' of the X-ray binary populations. When Lehmer *et al.* (2017) investigated NGC 5194 by dividing the galaxy into regions based on the local mean stellar age, indicated that the normalization of the XLF declines with age, while the overall XLF slope steepens. Furthermore, Zhang *et al.* (2012) investigated the dependence of the LMXB population in early-type galaxies and showed that older galaxies tend to possess about 50% more LMXBs (per unit stellar mass) than the younger ones and that the overall shape of the XLF for young galaxies is flatter than that of the old ones.

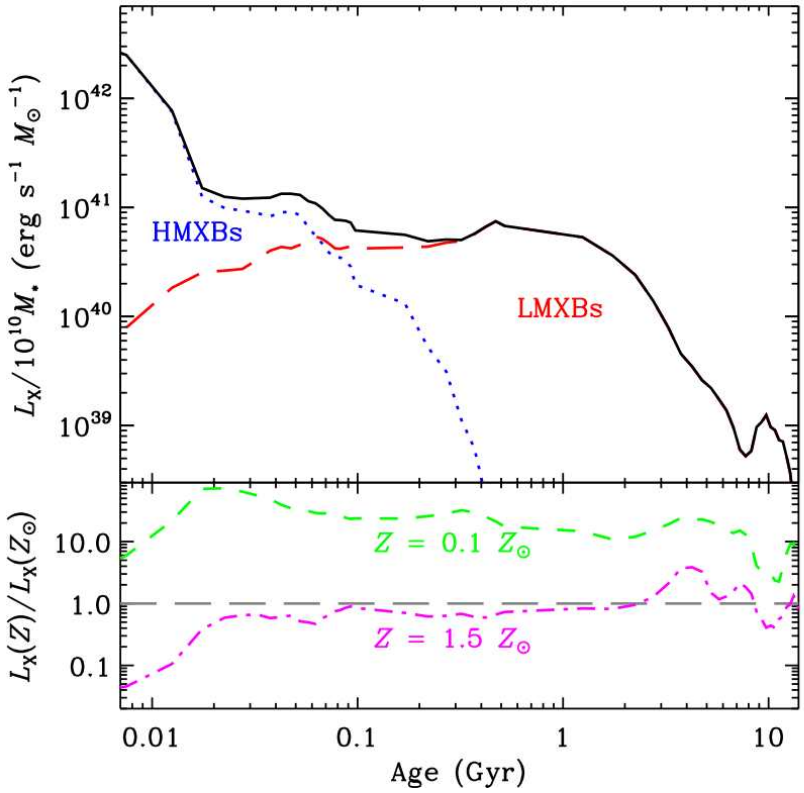

Figure 1.10: Top panel: Evolution of an XRB population formed in a single star-burst. The solid black line represents the total X-ray emission as a function of time. The dashed red, and blue dotted line represent the separate contribution of HMXBs, and LMXBs. Bottom panel: XRB evolution in respect with metallicity. Adopted from Fragos *et al.* (2013a)

Apart from the SFR, $M_\star$ and age, another factor that affects the populations of XRBs and their X-ray emission is stellar metallicity (Z). Binary population synthesis models suggest that galaxies of low (subsolar) metallicity should host more massive and more luminous compact objects, resulting in increased production of HMXBs with higher luminosities. In general agreement with these predictions, it has been observed that low-metallicity galaxies do host a larger number of luminous HMXBs at fixed SFR compared to high-metallicity galaxies (Brorby *et al.* 2014; Douna *et al.* 2015; Lehmer *et al.* 2019; Ponnada *et al.* 2019) and that ULXs are more common in low-metallicity galaxies (Kaaret *et al.* 2017).

1.5 Scope of thesis

In this thesis, we study the population of XRBs in nearby galaxies. It consists of two parts, in the first (Chapter 2) we study the vertical distribution of HMXBs in the closest to the Milky Way edge-on galaxy NGC 55, in correlation with the distribution of star formation within the galaxy. The goal is the estimation of the center of mass transverse velocity of HMXBs as they are displaced from their birth place, providing constrains on the kick velocities of the compact objects. Such estimation is the first for a galaxy located outside the Local Group.

In the second part (Chapter 3), we study the population of XRBs in all nearby galaxies. We use specific catalogues such as the *HECATE* (Kovlakas *et al.* 2021), and the *Chandra Source Catalogue 2.0 (CSC 2.0)* (Evans *et al.* 2020) that contain science ready data products estimated with homogeneous procedures. The X-ray source and galaxy samples are comprised of 10.099 X-ray sources in 319 nearby galaxies of all morphological types, covering a wide range of values in their intrinsic properties (SFR, stellar mass, metallicity) and therefore representing all galactic environments. The goal is to construct the differential X-ray Luminosity function (XLF) of the different types of XRBs (LMXBs and HMXBs), and using power-law models to estimate the emerging scaling relations with the intrinsic properties of the host galaxies. This is the most complete study of populations of XRBs in the literature, containing the largest sample of X-ray sources and galaxies.

2

Vertical distribution of HMXBs in NGC 55

Although HMXBs are typically associated with star-forming regions (Grimm *et al.* 2003, Fabbiano 2006, Persic & Rephaeli 2007), such as galaxy spiral arms and massive, young stellar clusters, there is observational evidence for a population of HMXBs that are somewhat offset from star-forming regions (van Rensbergen *et al.* 1996, Zezas *et al.* 2002, Kaaret *et al.* 2004). The observed displacement may be due to kicks after an asymmetric supernova explosion during the formation of the compact object (e.g. Fryer & Kalogera 1997). These kicks have fundamental implications for the population of X-ray binaries since they determine the survival and the post-SN orbital parameters of the system (Pfahl *et al.* 2002, Podsiadlowski *et al.* 2004). If they are large enough, kicks will extend the vertical distribution of HMXBs, which can potentially be measured in nearby edge-on galaxies with high angular resolution X-ray telescopes. The extended vertical distribution of HMXBs can be used to estimate the transverse velocity of the binary systems. NGC 55, the edge-on galaxy nearest the Milky Way at a distance of 1.94 Mpc (Gieren *et al.* 2008) provides an excellent environment for studying the association

between HMXBs and star-forming regions.

2.1 The HMXB population in NGC55

NGC 55 with a total mass of $2 \times 10^{10} M_{\odot}$ (Westmeier *et al.* 2013), is classified as an SB(s)m galaxy viewed at an inclination of 80° with an optical extent of 18.2 × 3.2 kpc (de Vaucouleurs *et al.* 1991). The optical morphology of NGC 55 is asymmetric, with the brightest region of the galactic disk located at 1.7 kpc west from the geometrical centre of the galaxy and along the galactic plane (de Vaucouleurs *et al.* 1991). The main properties of NGC 55 are presented in Table 2.1.

The population of X-ray sources in NGC 55 has been analysed as part of the Chandra Local Volume Survey (Binder *et al.* 2015) using archival ACIS data from the *Chandra* X-ray Observatory (ObsIDs 2255 and 4744). The source list consists of 154 X-ray sources down to a flux of 7×10^{-16} erg s^{-1} cm^{-2} ($L_x = 0.3 \times 10^{36}$ erg s^{-1} at a distance of 1.94 Mpc). Binder *et al.* (2015) classified the X-ray sources on the basis of either their optical associations with stars using *Hubble Space Telescope (HST)* fields selected from the ACS Nearby Galaxy Survey Treasury (Dalcanton *et al.* 2009), or their X-ray properties (hardness ratios): 65 as Active Galactic Nuclei (AGN), 10 as foreground stars, 11 as Supernova Remnants (SNRs) and 67 as XRBs, among which 24 as LMXBs and 43 as HMXBs.

Figure 2.1 shows the location of XRBs and AGN superimposed on a *GALEX* NUV (2267 Å) image (Gil de Paz *et al.* 2007). The sources are colour-coded according to their classification by Binder *et al.* (2015): XRBs in yellow and cyan (for candidate and verified HMXBs respectively - see Table 2.3), while background AGN in red. The footprints of the *HST* fields are shown with the orange boxes. Only 16 of the 43 X-ray sources classified as HMXBs have optical counterparts identified using *HST* data. The other 27 HMXB candidates extend beyond the *HST* fields and were classified based on X-ray hardness ratios alone, making them much less certain.

Table 2.1: NGC 55 properties

Parameter	Value
Morphological Type	SB(s)m: edge-on [1]
RA (hh:mm:ss)	00:14:53.60 [2]
Dec (± dd:mm:ss)	−39:11:47.9 [2]
Distance (Mpc)	1.94 ± 0.03 [3]
Major axis (2a arcsec; kpc)	1942; 18.2 [1]
Minor axis (2b arcsec; kpc)	338; 3.2 [1]
Position angle (degrees)	108 [1]
Inclination (degrees)	80 [1]
E(B-V) (mag)	0.01 [4]
Radial velocity (km s^{-1})	131 ± 2 [5]
Rotational velocity (km s^{-1})	90.6 ± 2.5 [5]
Stellar mass ($M_\odot$)	1.9×10^9 [11]
HI mass ($M_\odot$)	$(1.7 \pm 0.1) \times 10^9$ [5]
Total mass ($M_\odot$)	$(2.0 \pm 0.4) \times 10^{10}$ [5]
L_{TIR} ($L_\odot$) (3-1100 μm)	1.6×10^9 [4]
SFR ($M_\odot$ yr^{-1})	$0.137^{+0.023}_{-0.021}$ [6]
Metallicity [Fe/H]	-0.3 [7]
Scale $height_{Far\ IR}$ (kpc)	0.32 - 0.49 [8]
Scale $height\ optical_{F818W}$ (kpc)	0.24 [9]
Scale $height_{H\alpha}$ (kpc)	0.37 - 0.45 [10]

Notes: [1]de Vaucouleurs *et al.* (1991), [2]Jarrett (2000), [3]Gieren *et al.* (2008), [4]Dale *et al.* (2009), [5]Westmeier *et al.* (2013), [6]Weisz *et al.* (2011), [7]Davidge (2005), [8]Engelbracht *et al.* (2004),[9]Seth *et al.* (2005), [10]Miller & Veilleux (2003), [11]Kudritzki *et al.* (2016)

2.1.1 Contamination with background AGN

We first examine if the population of XRBs as classified by Binder *et al.* (2015) is contaminated with background AGN. We use the cumulative number counts of X-ray point sources published in the Chandra Multi-wavelength Project (*ChaMP*; Kim *et al.* 2007) down to the limiting flux of the *Chandra* observations for NGC 55. Figure 2.2 shows the *Chandra* field of view (FOV) for ObsID 2255 (red) and ObsID 4744 (blue). The FOV covers an area of 0.078 $degrees^2$, therefore the expected number of AGN based on *ChaMP* is approximately 78.

Alternatively, the AGN density can be determined empirically from the number

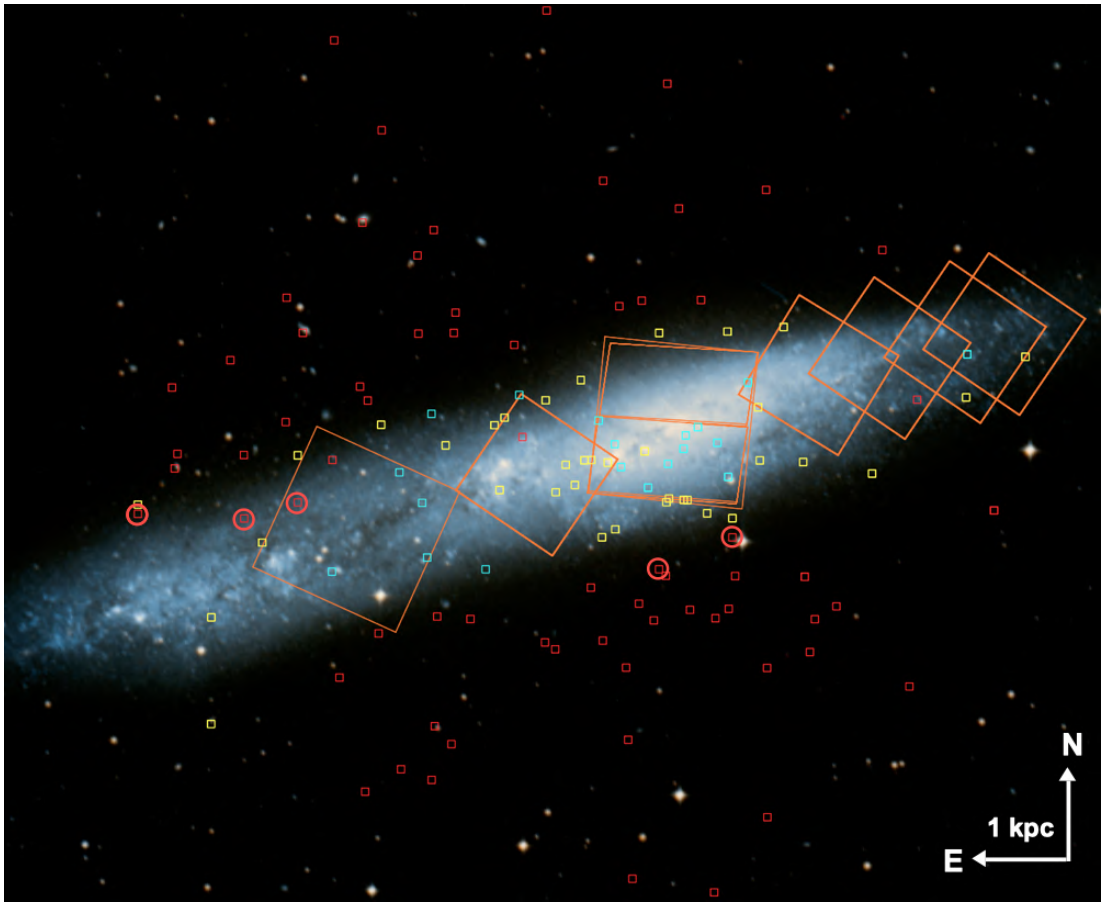

Figure 2.1: Population of X-ray sources in NGC 55 superimposed on a *GALEX* NUV (2267 Å) image (Gil de Paz *et al.* 2007). The X-ray soungcrces are colour-coded as follows: Candidate and verified HMXBs in yellow and cyan respectively, AGN in red (Binder *et al.* 2015). The footprints of the *HST* fields are shown as orange boxes.The five AGN encircled in red were initially classified as HMXBs (Binder *et al.* 2015) but based on our analysis in Section 2.1.1, we reclassify these as background AGN.

counts of background AGN in regions far off the plane of NGC 55, since most of the X-ray sources close to the plane and within the D_{25} (green ellipse in Figure 2.2) are categorised as candidate XRBs. The result for the AGN density is approximately 80 X-ray sources within the *Chandra* FOV, in close agreement with the estimation using the expected AGN number density from *ChaMP*.

Since there are 59 X-ray sources classified as AGN by Binder *et al.* (2015) within the *Chandra* FOV for observation 2255, we estimate that there may be ∼20 background

AGN among the 67 sources classified as XRBs.

We also quantify the percentage of contamination by looking at the distribution of all X-ray sources classified as AGN. A Kolmogorov-Smirnov (K-S) test across vertical bins of 0.1 kpc from the plane, derives that at a confidence level of 95%, their distribution does not follow a uniform one. On the other hand, if we exclude the bins corresponding to the D_{25} of the galaxy where most of the X-ray sources are categorised as candidate XRBs and perform a KS test across the rest of the bins, at a confidence level of 95%, the distribution of AGN derives from a uniform one. In order to estimate the number of background AGN among candidate XRBs in the D_{25} region, we modify the distribution of all X-ray sources classified as AGN by adding sources at random locations within the D_{25}. Each time a new source is added, a K-S test across all bins determines if the distribution derives from a uniform one. The number of sources within the D_{25} required for the distribution of AGN to derive to high confidence from a uniform one, is between 14 and 23, in agreement with the previous estimation for $\sim$20 background AGN.

We next investigate the characterisation of the X-ray sources as HMXBs, by supplementing their classification with mid-IR photometry of NGC 55 from *Spitzer* IRAC (Williams & Bonanos 2016). We crossmatch the list of X-ray sources in Binder *et al.* (2015) with the list of mid-IR sources in Williams & Bonanos (2016) using only those mid-IR sources that have been detected in all four *Spitzer* IRAC channels. This results in 21 matches presented in Table 2.2, from which 9 are classified as HMXBs and 12 as AGN in Binder *et al.* (2015).

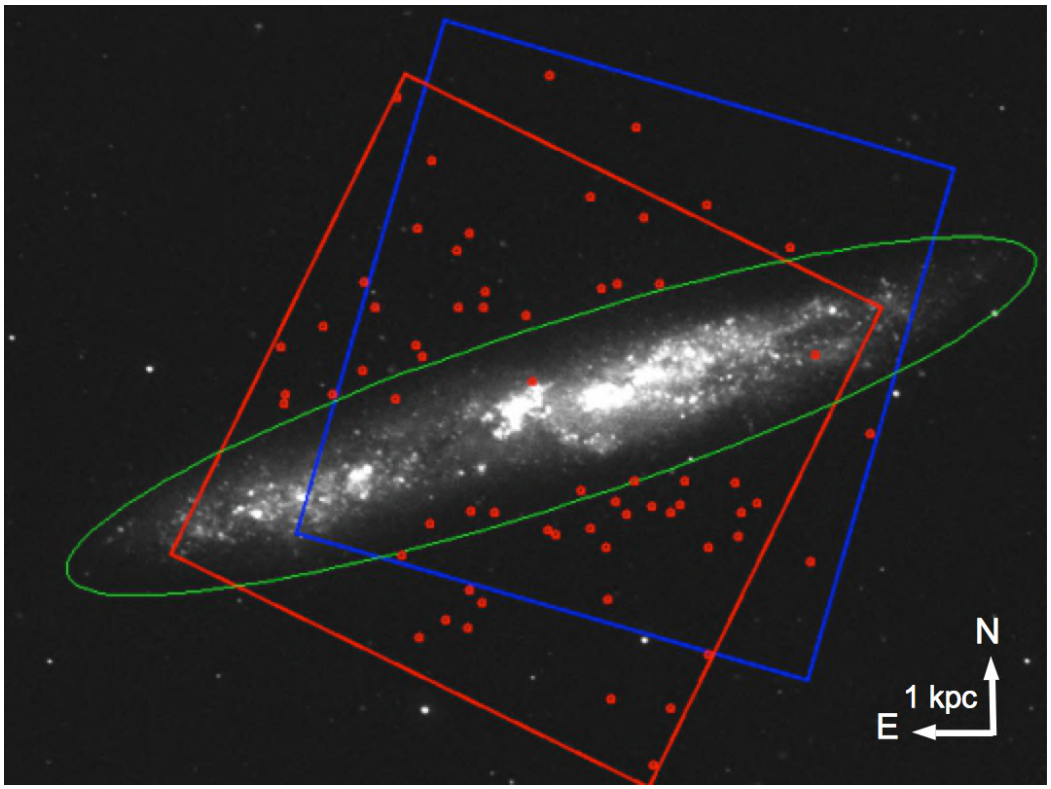

Figure 2.2: Location of AGN (red circles) in the *Chandra* FOV for ObsID 2255 (red) and ObsID 4744 (blue). The D_{25} of NGC 55 is shown as a green ellipse. The number counts of background AGN far off the plane of NGC 55 is used for empirically determining the AGN density within the *Chandra* FOV.

Table 2.2: Mid-IR properties of X-ray sources

X-ray source number	RA	Dec	Classification	Separation	[3.6]	[4.5]	[5.8]	[8.0]
(1)	(2)	(3)	(4)	(5)	(6)	(7)	(8)	(9)
2	00:15:02.1	−39:16:46.2	AGN	0.23	16.27	17.20	16.14	14.85
11	00:14:56.1	−39:16:18.6	AGN	0.26	17.00	16.58	15.60	14.89
60	00:14:29.2	−39:07:52.5	AGN	0.69	17.27	16.31	15.52	14.29
67	00:14:50.6	−39:09:01.1	AGN	0.07	16.51	15.80	15.32	14.31
68	00:14:42.9	−39:06:30.6	AGN	0.54	16.57	16.09	15.20	14.09
90	00:15:19.4	−39:09:18.3	AGN	0.64	18.06	17.48	15.97	15.26
95	00:15:23.8	−39:09:46.8	AGN	0.35	16.37	15.69	14.93	14.14
104	00:15:45.9	−39:10:22.8	AGN	0.43	16.68	16.08	15.74	15.24
108	00:15:39.4	−39:11:47.4	AGN	0.75	18.07	17.18	15.56	14.60
113	00:15:52.1	−39:12:30.6	AGN	0.24	16.08	15.62	15.29	14.54
152	00:15:08.9	−39:16:48.7	AGN	0.10	17.21	16.41	15.58	14.45
34	00:14:16.0	−39:13:47.8	AGN	0.98	17.24	16.66	16.03	14.47
75	00:15:02.7	−39:10:28.8	HMXB	0.64	16.92	16.29	15.76	14.90
79	00:15:04.0	−39:11:53.8	HMXB	0.20	17.12	16.57	15.66	14.29
80	00:15:04.6	−39:10:43.9	HMXB	0.20	16.98	15.84	14.80	13.25
92	00:15:11.9	−39:11:10.8	HMXB	0.54	16.94	16.87	16.03	15.57
101	00:15:20.0	−39:11:37.1	HMXB	0.34	17.82	16.71	14.92	13.91
103	00:15:22.3	−39:11:36.4	HMXB	0.22	17.49	16.76	15.65	15.34
110	00:15:44.3	−39:12:08.9	HMXB	0.11	15.36	14.82	14.34	13.32
130	00:15:33.9	−39:15:11.8	HMXB	0.99	16.90	16.51	13.85	11.45
140	00:15:15.9	−39:15:08.8	HMXB	0.26	17.89	17.37	16.57	16.25

Column description: (1) X-ray source number assigned by Binder *et al.* (2015) list, (2) RA (hh mm ss.ss) J2000, (3) Dec (−dd mm ss.ss) J2000, (4) X-ray classification according to Binder *et al.* (2015), (5) Separation between X-ray and mid-IR sources in arcsec, (6) 3.6 μm mag, (7) 4.5 μm mag, (8) 5.4 μm mag, (9) 8.0 μm mag

In order to identify the contaminating AGN among the matched HMXB sources, we apply a mid-IR diagnostic that enables the distinction between AGN and massive stars. The diagnostic we use is the [3.6]-[4.5] vs. [5.8]-[8.0] μm colour-colour diagram in which Stern *et al.* (2005) empirically defined the locus of AGN (the so-called "Stern wedge"), delineated by the dashed line in Figure 2.3. To check the credibility of the "Stern wedge" diagnostic we populate the [3.6]-[4.5] vs. [5.8]-[8.0] μm diagram with spectroscopically classified massive stars (bottom panel) from nearby galaxies, derived from the catalogues of Williams *et al.* (2015), Khan *et al.* (2015) and Castro *et al.* (2008). We see that the overlap of stars with the AGN locus is very small.

Figure 2.3 (top panel) shows the HMXBs (red stars) and AGN (blue filled circles) with mid-IR counterparts placed on a mid-IR [3.6]-[4.5] vs. [5.8]-[8.0] diagram. From the nine sources classified as an HMXB by Binder *et al.* (2015), five fall within the "Stern wedge". Four of these five sources are found at large distances from the plane of NGC 55 (encircled in red in Figure 2.1), which decreases the chance that these sources are associated with NGC 55. The four of the nine sources sources that do not fall within the "Stern wedge" and the diagnostic suggests are HMXBs, are placed on a mid-IR colour-magnitude diagram (Figure 2.4). The similarity of these optical associations with other spectroscopically classified massive O-type, B-type, A-type, and LBV stars in NGC 55 (Castro *et al.* 2008) further supports the nature of these X-ray sources as HMXBs. From the 12 sources classified as an AGN by Binder *et al.* (2015), all but one fall within the Stern wedge.

2.1.2 Counterparts of HMXBs

We also investigate the classification by Binder *et al.* (2015) as HMXBs for those sources with *HST* counterparts. We place them on an *HST* colour-magnitude diagram (Figure 2.5) with the absolute magnitude computed using the distance in Table 2.1 (distance modulus of 26.43 mag). We have also over-plotted the 100 Myr and 20 Myr isochrones

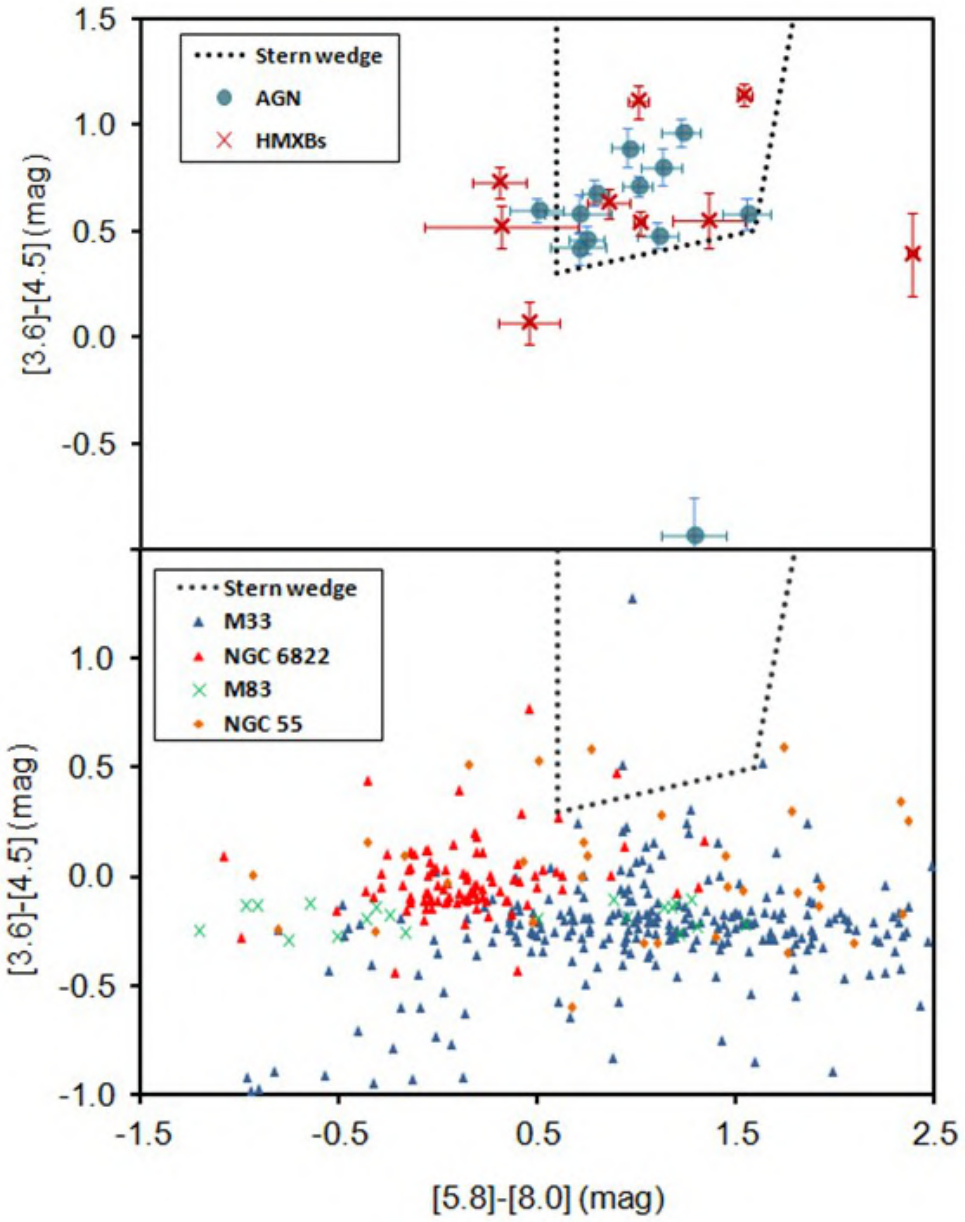

Figure 2.3: Colour-colour diagram for the identification of AGN based on mid-IR colours. The dashed line in both panels delineates the AGN locus ("Stern wedge", Stern *et al.* 2005). Top panel: X-ray sources in NGC55 with mid-IR counterparts. Sources classified as HMXBs (red stars) and AGN (blue filled circles) according to Binder *et al.* (2015). Five HMXBs are located within the AGN locus. Bottom panel: To check the credibility of the "Stern wedge" diagnostic, we populate the [3.6]-[4.5] vs. [5.8]-[8.0] μm diagram with spectroscopically resolved massive stars in NGC 55 and other nearby galaxies (Williams *et al.* 2015, Khan *et al.* 2015 and Castro *et al.* 2008). Very few massive stars have mid-IR colours consistent with the Stern wedge.

from the Geneva stellar models (Ekström *et al.* 2012). After applying a reddening correction of E(B-V)=0.01 (Table 2.1), all but two HMXBs, are bounded by the 100 Myr isochrone. We therefore conclude that the *HST* colour-magnitude diagram is consistent with the classification of the X-ray sources with *HST* counterparts as HMXBs by Binder *et al.* (2015). We note that due to the low X-ray luminosity ($<10^{37}$ erg s^{-1}) of the aforementioned sources, illumination of the companion star from the accretion disk around the compact object which may affect their location on the colour-magnitude diagram does not pose a problem.

To summarise, of the 67 XRBs identified by Binder *et al.* (2015), HST and Spitzer imaging confirms an early-type star as the counterpart to 19 sources, which form our sample of "verified HMXBs". For six of the remaining 48 XRBs, HST imaging suggest that they are LMXBs and are therefore not included in our analysis. That leaves 42 XRBs, for which statistics suggest that as many as 20 may be AGN. Using IR imaging, we identify five of the 42 XRBs as being AGN contaminants. The remaining 37 XRBs, from which as many as 15 (40%) may be AGN, form our sample of "candidate HMXBs".

Furthermore, if we consider the Grimm *et al.* (2003) relation for the number of expected HMXBs for the NGC 55 SFR (Table 2.1), we have ∼15 HMXBs with L_x brighter than 10^{36} erg s^{-1}. According to Table 2.3, the number of HMXBs with L_x $> 10^{36}$ erg s^{-1} is 26, seven in the "verified HMXBs" sample and 19 in the "candidate HMXBs" sample. Applying the estimated percentage (40%) for AGN contamination in the "candidate HMXBs" sample, we determine that the expected number of HMXBs with $L_x > 10^{36}$ erg s^{-1} is ∼18.

For the remainder of this work, we consider as HMXBs all 19 "verified HMXBs" as well as randomly selected combinations of 22 out of 37 "candidate HMXBs", thereby incorporating our estimated AGN contamination.

We note that none of these HMXBs are spectroscopically confirmed, and therefore are all only candidates (even the "verified" ones). Defining their nature requires further

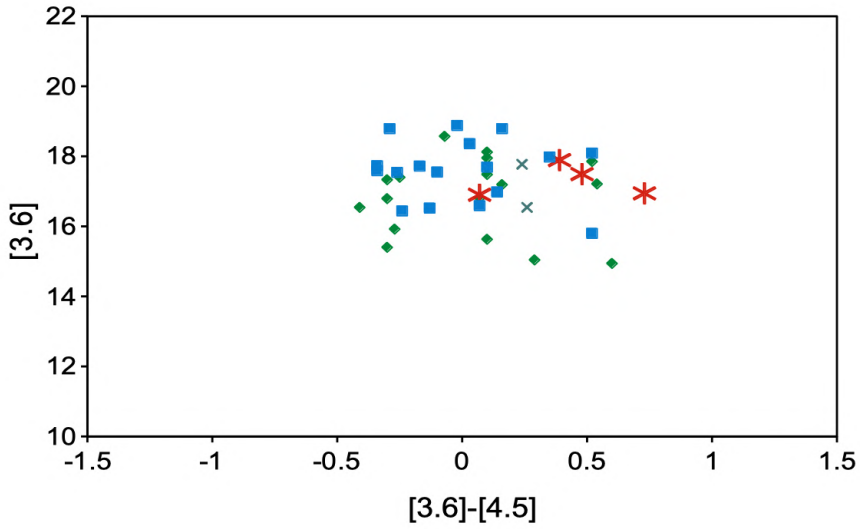

Figure 2.4: Mid-IR colour-magnitude diagram for spectroscopically classified massive stars in NGC 55 (Castro *et al.* 2008). The similarity of the IR colours between the four X-ray sources (magenta stars) falling outside the Stern wedge in the top panel of Figure 2.3 and the reference stars further supports their classification as HMXBs by Binder *et al.* (2015).

information (X-ray spectra, HST imaging, time variability) that is not yet available.

The list of HMXBs is presented in Table 2.3. Columns "RA" and "Dec" indicate the location of XRBs as provided by Binder *et al.* (2015). Column *"z"* presents the inclination corrected vertical distance of each XRB from the mid-plane of the galaxy in kpc. Column *"Flux"* provides the unabsorbed 0.35 - 8 keV flux (Binder *et al.* 2015). Column "L_x" presents the X-ray luminosity of each XRB in units of 10^{36} erg s^{-1} estimated from the relevant flux and the distance of NGC 55 in Table 2.1.

Table 2.3: HMXBs catalog

Verified HMXBs					candidate HMXBs				
RA	Dec	z	Flux	$L_{x,36}$	RA	Dec	z	Flux	$L_{x,36}$
(1)	(2)	(3)	(4)	(5)	(1)	(2)	(3)	(4)	(5)
00:14:19	−39:10:14	0.27	11.0	4.95	00 14 12	−39:10:17	0.43	9.0	4.05
00:14:45	−39:10:53	0.29	1.8	0.81	00 14 19	−39:11:13	0.78	255.0	114.77
00:14:47	−39:13:02	0.76	0.9	0.41	00 14 30	−39:12:57	1.24	18.7	8.42
00:14:48	−39:12:15	0.31	1.2	0.54	00 14 38	−39:12:42	0.84	7.1	3.20
00:14:50	−39:11:54	0.04	1.2	0.54	00 14 40	−39:09:37	0.87	10.7	4.82
00:14:52	−39:12:06	0.09	2.9	1.31	00 14 43	−39:12:40	0.69	5.6	2.52
00:14:52	−39:12:24	0.24	5.1	2.30	00 14 43	−39:11:27	0.00	3.3	1.49
00:14:54	−39:12:44	0.36	1.0	0.45	00 14 46	−39:13:58	1.26	5.0	2.25
00:14:56	−39:13:17	0.56	5.1	2.30	00 14 47	−39:09:44	0.99	2.0	0.90
00:14:59	−39:12:49	0.20	2.0	0.90	00 14 49	−39:13:52	1.11	1.3	0.59
00:15:00	−39:12:18	0.10	6.4	2.88	00 14 52	−39:13:34	0.84	1.9	0.86
00:15:02	−39:11:45	0.43	1.2	0.54	00 14 52	−39:13:34	0.83	1.6	0.72
00:15:11	−39:11:10	1.07	0.8	0.36	00 14 54	−39:13:32	0.75	0.9	0.41
00:15:15	−39:15:08	0.88	1.9	0.86	00 14 54	−39:13:37	0.81	1.2	0.54
00:15:22	−39:11:36	1.20	7.6	3.42	00 14 55	−39:09:46	1.25	1.4	0.63
00:15:22	−39:14:52	0.50	0.8	0.36	00 14 57	−39:12:27	0.07	1.3	0.59
00:15:23	−39:13:37	0.17	1.3	0.59	00 15 00	−39:14:14	0.92	1.1	0.50
00:15:26	−39:12:56	0.63	1.1	0.50	00 15 01	−39:12:43	0.06	1.0	0.45
00:15:33	−39:15:11	0.28	17.0	7.79	00 15 02	−39:14:25	0.97	2.9	1.31
					00 15 03	−39:12:39	0.00	4.8	2.16
					00 15 03	−39:12:41	0.00	0.8	0.36
					00 15 04	−39:12:39	0.42	1.5	0.68
					00 15 04	−39:10:50	1.00	4.1	1.85
					00 15 05	−39:13:13	0.24	4.7	2.12
					00 15 06	−39:12:46	0.07	0.8	0.36
					00 15 07	−39:13:23	0.22	2.0	0.9
					00 15 08	−39:11:18	0.94	1.1	0.5
					00 15 13	−39:11 41	0.85	5.7	2.57
					00 15 14	−39:13:20	0.04	3.0	1.35
					00 15 14	−39:11:51	0.81	0.7	0.32
					00 15 20	−39:12:19	0.79	1.2	0.54
					00 15 28	−39:11:51	1.29	2.0	0.9
					00 15 38	−39:12:32	1.25	17.5	7.88
					00 15 42	−39:14:31	0.35	2.8	1.26
					00 15 48	−39:16:13	0.34	7.1	3.2
					00 15 48	−39:18:39	1.68	47.0	21.15
					00 15 56	−39:13:39	1.30	11.6	5.22

Column description: (1) X-ray source number assigned by Binder *et al.* (2015) list, (2) RA (hh mm ss.ss) J2000, (3) Dec (−dd mm ss.ss) J2000, (4) X-ray classification according to Binder *et al.* (2015), (5) Separation between X-ray and mid-IR sources in arcsec, (6) 3.6 μm mag, (7) 4.5 μm mag, (8) 5.4 μm mag, (9) 8.0 μm mag

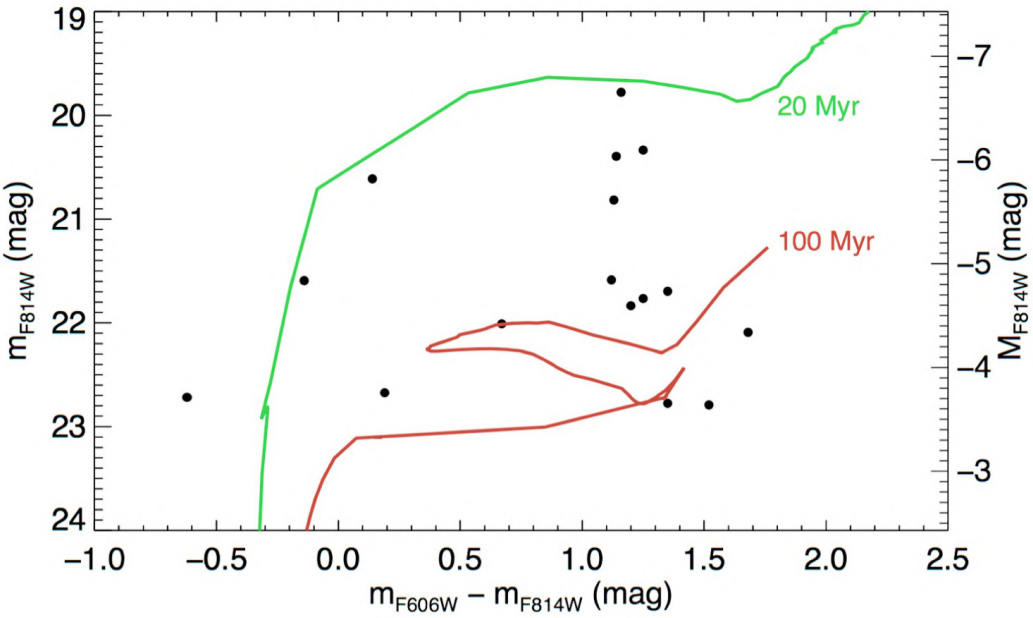

Figure 2.5: Reddening corrected *HST* colour-magnitude diagram of the optical counterparts of the X-ray sources (black dots) classified as HMXBs by Binder *et al.* (2015). 20 Myr and 100 Myr isochrones from the Geneva stellar models (Ekström *et al.* 2012) are over-plotted for reference. All but three stars are bounded by the 100 Myr isochrone, confirming their young age and the classification of the X-ray sources by Binder *et al.* (2015) as HMXBs.

2.2 Vertical distribution of HMXBs in NGC 55

In this section we measure the vertical distances of HMXBs from the mid-plane of NGC 55, compare their vertical distribution with the distribution of star-forming activity and estimate the centre-of-mass transverse velocity of the X-ray binary systems. We choose to measure the distance of HMXBs from the mid-plane, since due to the distance of NGC 55, the projected density of star-forming regions is too large to allow us to identify the possible birthplace of each individual HMXB among young star clusters or OB associations, as has been done in the SMC (Coe 2005), LMC (Antoniou & Zezas 2016) and the MW (Bodaghee *et al.* 2012). This is evident in Figure 2.6, which shows separate, representative HMXBs (indicated with an X) located at large distances from the mid-plane, superimposed on a starlight continuum subtracted Hα image of NGC 55 (Kopscacheili et al., in prep.) which traces star-forming regions. Around each HMXB we draw a 1 kpc radius circle (which, assuming a centre of mass velocity of 40 km s^{-1} corresponds to a travel time of 25 Myrs) with the radial vector pointing towards the mid-plane of the galaxy. We cannot correlate individual HMXBs with specific star-forming regions either because there are multiple possible regions or because there is no star-forming region nearby.

2.2.1 Vertical distance of HMXBs and SFR

We define as the mid-plane of NGC 55, the plane where star-formation rate (SFR) peaks. For this reason we use the highest resolution and least absorption-dependent SFR indicator we have available. This is the 8.0 μm IRAC image that traces polycyclic aromatic hydrocarbon (PAH) emission from the star forming regions and correlates almost linearly with the SFR if the small contribution from older stellar populations that also emit in the IR is removed (Calzetti 2008).

We use the publicly available SINGS IRAC images of NGC 55 (Dale *et al.* 2009)

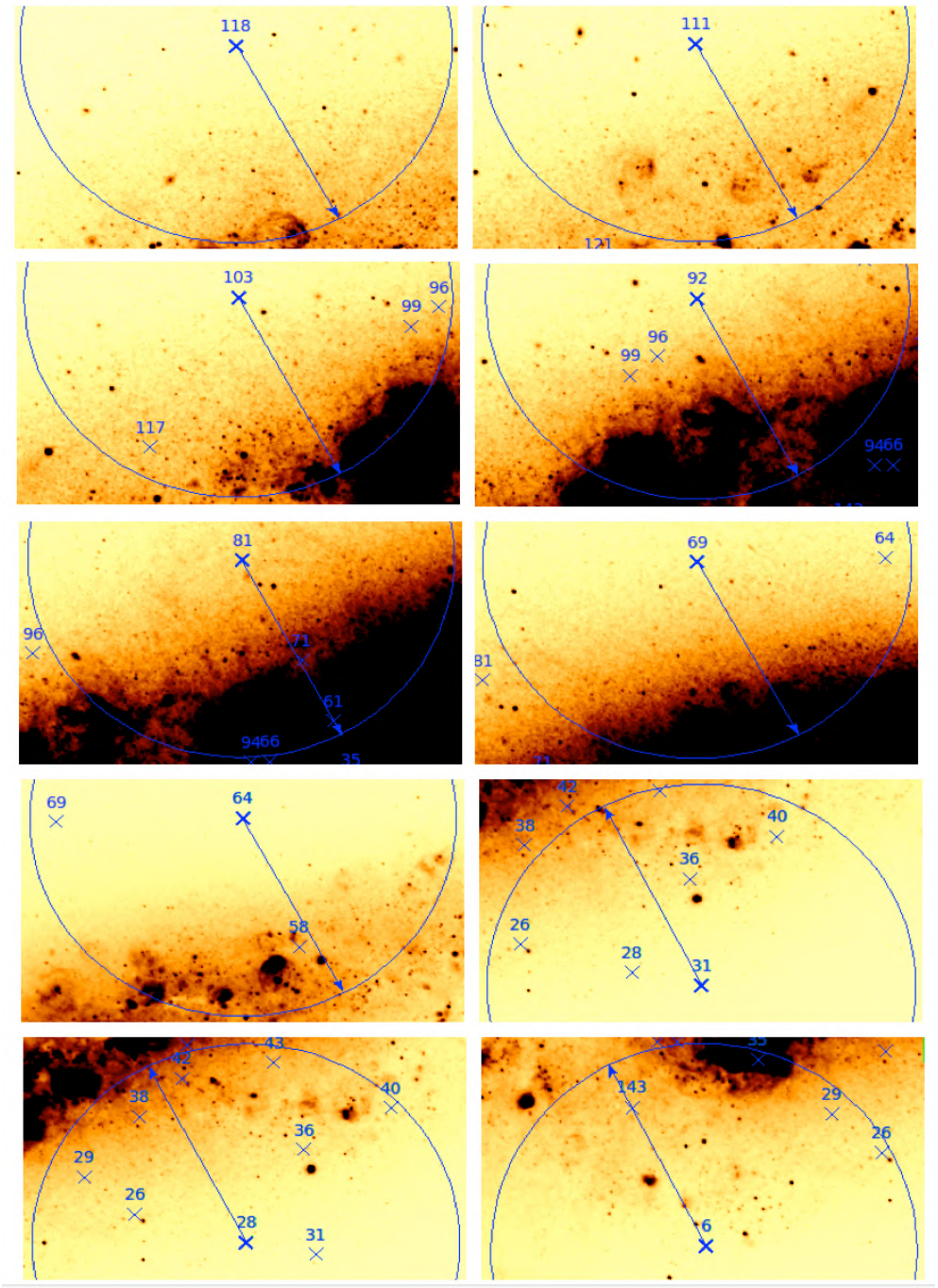

Figure 2.6: HMXBs located at large distances from the mid-plane superimposed on a starlight-subtracted Hα image that traces star-forming regions. Each HMXB is indicated with an X and is encircled by a 1 kpc radius circle with the radial vector pointing towards the mid-plane of the galaxy. Individual HMXBs may be associated with any one of several star-forming regions.

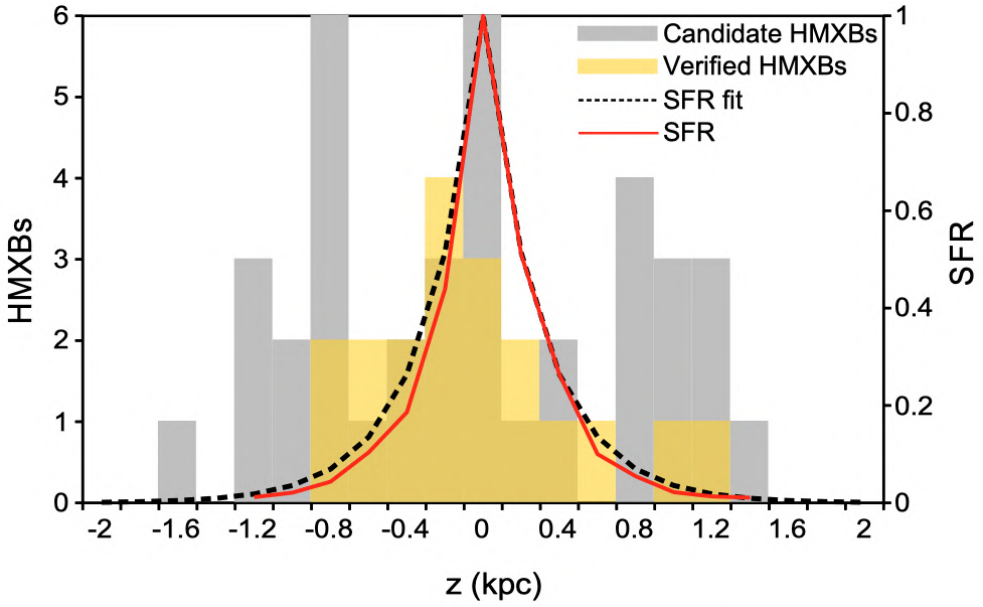

Figure 2.7: Vertical distribution of HMXB density in bins of 0.1 × 18 kpc (0.18′× 32′) from the mid-plane of NGC 55 (candidate and verified HMXBs in grey and yellow respectively). The red line indicates the vertical distribution of the 8.0μm-based SFR density with the black line showing its best-fit exponential profile. HMXBs extend beyond the star-forming region. North towards the positive values of z.

and we subtract the 3.6 μm image from the 8.0 μm image using a scaling factor of 0.26 (Wu *et al.* 2005) in order to remove the contribution from the non star-forming, stellar populations and create a "star-formation" 8.0 μm image.

We then take slices with length equal to the major axis of NGC 55, at an angle equal to the position angle of NGC 55 at 108° (de Vaucouleurs *et al.* 1991, Table 2.1). The thickness of each slice is 1.98″, equal to the FWHM of Spitzer's IRAC band 4 PSF*. We take as many slices as required to fully cover the extent of NGC 55 as defined by the D_{25} (Figure 2.2) and measure the surface brightness in each slice. The slice with the highest surface brightness is selected as the mid-plane of NGC 55 and is shown as the red line in all panels in Figure 2.8.

We measure the vertical distribution of the SFR density from the star-forming 8.0 μm image calculated in bins of the same size as in the case of HMXBs (yellow histogram

* (http://irsa.ipac.caltech.edu/data/SPITZER/docs/irac/ iracinstrumenthandbook/)

in Figure 2.7). We model the SFR density with an exponential profile:

$$S(z) = S_0 e^{-z/z_{\rm sfr}} \tag{2.1}$$

where $S(z)$ is the surface brightness along the z axis, S_0 is the surface brightness at the mid-plane of the galaxy and $z_{\rm sfr}$ is the vertical scale height. Fitting our data using a least-squares fit, we derive a star-formation scale height of $z_{\rm sfr}$=330±90 pc (red line in Figure 2.7).

2.2.2 Displacement of HMXBs from star-forming regions

We observe in Figure 2.7 that the star-forming activity is confined to the disk of NGC 55 with a scale height of 330±90 pc, whereas the HMXBs are substantially extended beyond the SFR density. This suggests a "puffed-up" population of HMXBs with respect to their birthplaces. The existence of a broadening in the spatial distribution of HMXBs is further shown in Figure 2.8, where we over-plot the location of HMXBs on images of NGC 55 that present different star-formation tracers. In the top panel we show the 8.0 μm image (Dale *et al.* 2009) with the contribution from non-star-forming, stellar populations subtracted, as discussed in the previous section. In the middle panel, we show a *GALEX* NUV (2267 Å) image (Gil de Paz *et al.* 2007) that traces light from young stars. On the bottom panel is a starlight continuum subtracted Hα image obtained with the 4-m Blanco telescope at CTIO (Kopsacheili et al., in prep.) tracing recent star formation. The positions of HMXBs are shown as green, white and blue circles in the top, middle and bottom panels, respectively. In all three images, a significant fraction of XRBs are located beyond the extent of star-formation activity and at large vertical offsets from the mid-plane.

We qualitatively examine this broadening in the spatial distribution of HMXBs by reconstructing the distribution of vertical offsets of HMXBs with respect to their

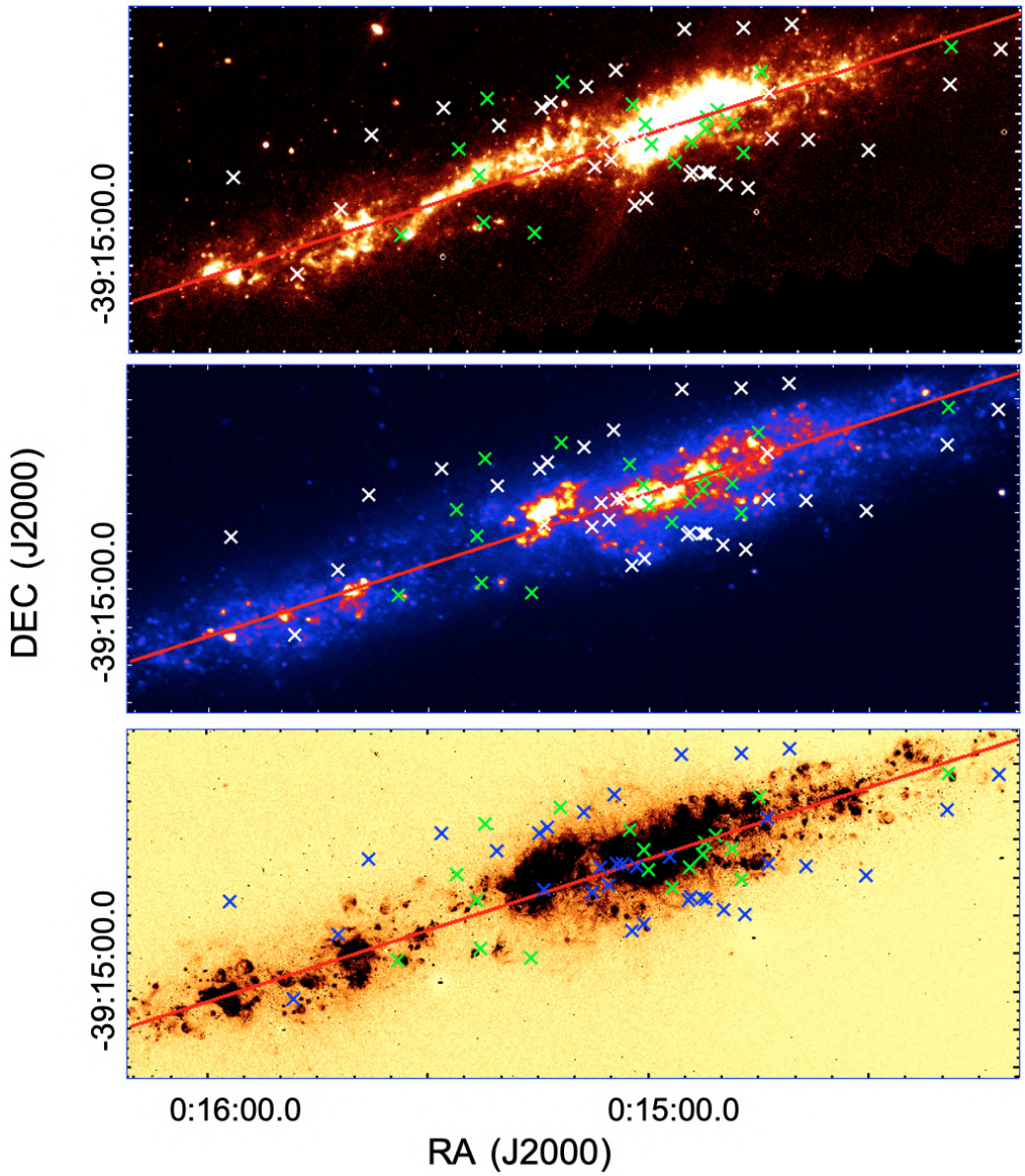

Figure 2.8: Locations of HMXBs and distribution of star-formation in NGC 55 based on different star-formation tracers. Top: 8.0μm image (Dale *et al.* 2009) with the contribution from non-star-forming, stellar populations subtracted. Middle: GALEX NUV (2267 Å) image (Gil de Paz *et al.* 2007) that traces light from young stars. Bottom: Starlight continuum subtracted Hα image (Kopsacheili et al., in prep.) tracing recent star formation. The red line depicts the mid-plane of NGC 55 as determined in Section 2.2.1. Candidate HMXBs are presented as white (top, middle panel) and blue (bottom panel) while verified HMXBs are presented as green in all panels. The HMXB population extends at large vertical offsets and at regions with relatively low star-forming activity.

birthplace by means of a Monte Carlo simulation. We sample randomly selected HMXB birth and current locations all drawn from the exponential distribution in equation 2.1, thereby creating virtual birthplaces and virtual locations of HMXBs. We measure the vertical offsets between virtual birthplaces and their nearest virtual HMXB location and produce a distribution that represents the null hypothesis, that HMXBs are co-located with their parent star-forming region. We also measure the vertical offsets between virtual birthplaces and the nearest HMXB location from our HMXB sample and produce a distribution that represents the hypothesis that HMXBs are displaced from their parent star-forming region. We perform 10,000 iterations and calculate the distributions in 0.1 kpc bins. In order to account for the AGN contamination of 15 out of the 37 "candidate HMXBs" (Table 2.3), in each iteration our HMXB sample consists of randomly selected combinations of 22 out of 37 "candidate HMXBs", in addition to the 19 "verified HMXBs" (Table 2.3) for which no AGN contamination is considered. The results are presented in Figure 2.9. The distribution under the hypothesis that HMXBs are displaced from their parent star-forming region (grey histogram) is extended compared with the distribution under the null hypothesis (yellow histogram). Furthermore, a K-S test indicates the two populations are different at the 99.8% confidence level. We next quantify the observed displacement of HMXBs, which is attributed to kicks after an asymmetric supernova explosion during the formation of the compact object (Fryer & Kalogera 1997). The contribution of natal kicks is treated as a Gaussian smearing function of standard deviation σ, that broadens the spatial distribution of HMXBs compared with their birth distribution. We simulate the vertical distribution of HMXBs from the mid-plane as the convolution $P(\mathrm{z}|\sigma,\mathrm{z}_{\mathrm{sfr}})$ between this Gaussian and the exponential distribution of SFR

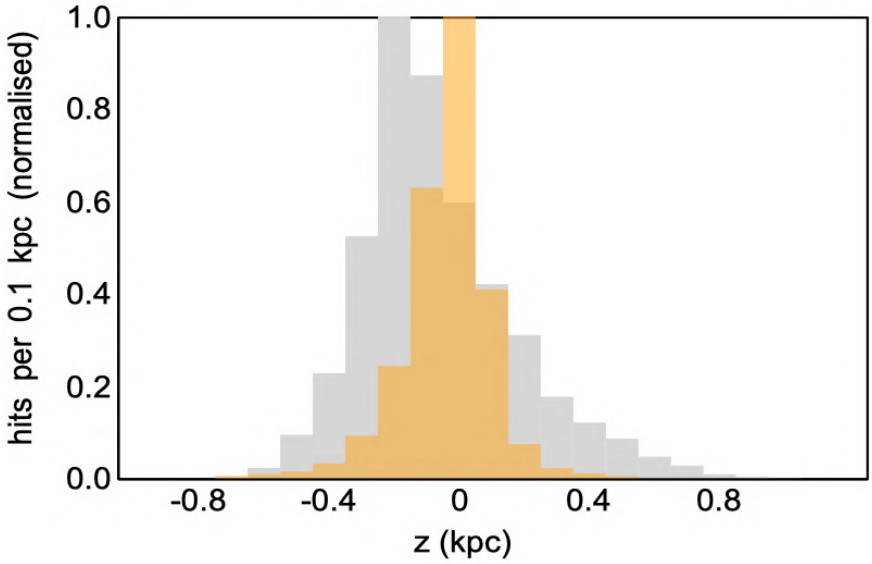

Figure 2.9: Distribution of HMXB vertical offsets calculated from Monte Carlo realisations of randomly selected birthplaces within the star-forming region. The distribution under the hypothesis that HMXBs are displaced from their parent star-forming region (grey histogram) is extended compared with the distribution under the null hypothesis (yellow histogram)

(equation 2.2) with a scale height of z_{sfr}=330 pc (Figure 2.11):

$$P(z|\sigma, z_{sfr}) = \sqrt{\frac{\pi\sigma^2}{2}}\mathbf{exp}\left(\frac{\sigma^2}{2z_{sfr}^2} - \frac{z}{z_{sfr}}\right) \times \left[\mathbf{erfc}\left[\sqrt{\frac{\sigma^2}{2}}\left(\frac{z}{\sigma^2} - \frac{1}{z_{sfr}}\right)\right] - \mathbf{exp}\left(\frac{2z}{z_{sfr}}\right)\mathbf{erfc}\left[\sqrt{\frac{\sigma^2}{2}}\left(\frac{z}{\sigma^2} + \frac{1}{z_{sfr}}\right)\right] - 2\right] \tag{2.2}$$

We apply the maximum likelihood method for finding the best estimate of the Gaussian smearing parameter σ. The likelihood function $L(\mathbf{z}|\sigma,z_{sfr})$ derived from the convolution P is:

$$L(\mathbf{z}|\sigma, z_{sfr}) = \prod_{i=1}^{N} P(z_i|\sigma, z_{sfr}) \tag{2.3}$$

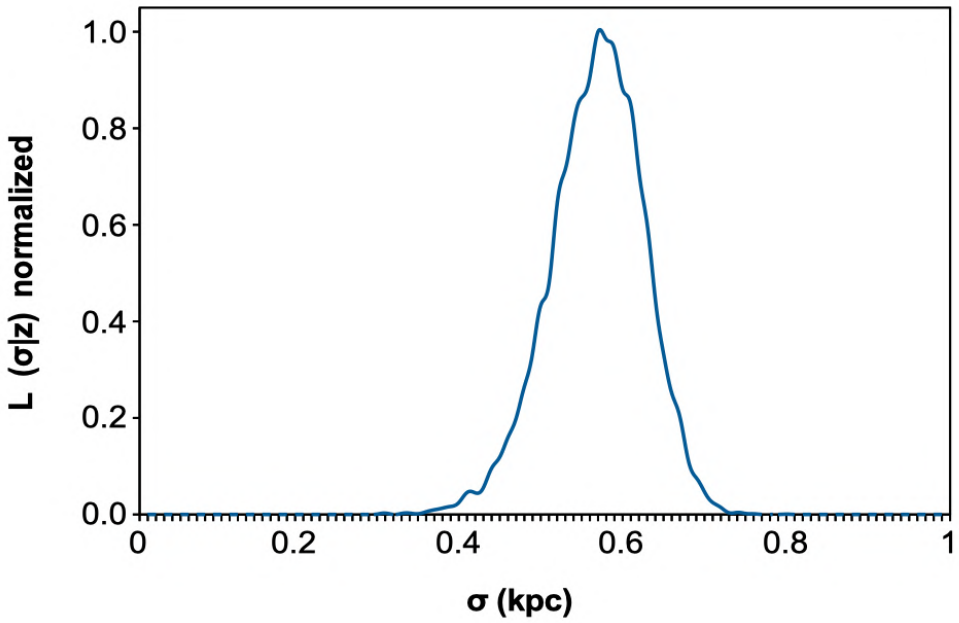

Figure 2.10: The likelihood of the dispersion of the Gaussian smearing function (normalised to the maximum likelihood σ), described in Section 2.2.2. The maximum at $\sigma = 0.57$ kpc is the scale height corresponding to the displacement between HMXBs and star-forming regions.

where N=41 is the number of HMXBs and z_i the vertical distance of the ith HMXB from the mid-plane of NGC 55. We perform 100,000 iterations and in order to account for the estimated AGN contamination, in each iteration our HMXB sample consists of all "verified HMXBs" (Table 2.3) as well as randomly selected combinations of 22 out of 37 "candidate HMXBs" (Table 2.3).

In Figure 2.10 we show the likelihood of the dispersion of the Gaussian smearing function (normalised to the maximum likelihood). The maximum at $\sigma = 0.57 \pm 0.07$ kpc is the difference between the scale height of the vertical distribution of HMXBs and the vertical distribution of star-forming activity.

2.2.3 Constraining the displacement of HMXBs

The result of the previous section provides an upper limit on the scale height of HMXBs. There are other factors such as contamination, incompleteness and in-situ formation of

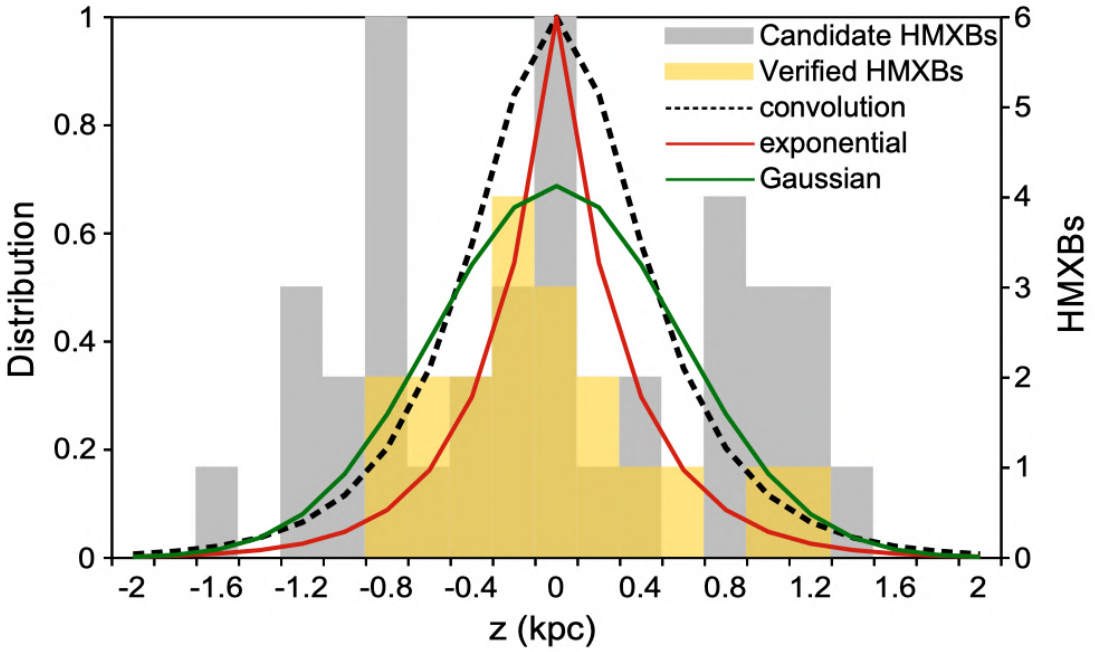

Figure 2.11: Simulated vertical distribution of HMXBs (black dashed) as the convolution between a Gaussian smearing function of standard deviation $\sigma = 0.57$ kpc (green) that represents the contribution of kicks, on top of the their birth distribution of 0.33 kpc (red). The grey and yellow histograms show the observed vertical distribution of candidate and verified HMXBs respectively.

HMXBs that bias the result of our analysis toward larger scale heights. We investigate these factors in an effort to constrain the lower limit on the scale height of HMXBs.

Although contamination from approximately 15 AGN interlopers from the "candidate HMXBs" sample has been incorporated in the estimation of the scale height of HMXBs, we can make additional assumptions that constrain its effect towards lower scale heights. We first consider as interlopers the 15 "candidate HMXBs" with the largest distances from the mid-plane. Repeating the analysis of Section 2.2.2 and excluding the "candidate HMXBs" with the largest distances from the mid-plane, the resulting scale height of the vertical distribution of HMXBs is no less than 0.33 kpc.

We then make the hypothesis that all "candidate HMXBs" are either AGN interlopers or misclassified LMXBs. By repeating the analysis of Section 2.2.2 including only the "verified HMXBs", we find that the scale height of the vertical distribution of HMXBs is

0.39 kpc.

The other factor that would bias the results toward larger scale heights, is incompleteness at the low luminosities. There are three major effects leading to incompleteness.

The first derives from the dependence of the point response function on the off-axis angle. We expect this effect to be important at angular distances larger than $8'$ from the aim-point (Wong *et al.* 2015). Since only four HMXBs from the sample of "candidate" and "verified" are located at distances larger than $8'$ from the aim-point, incompleteness due to off-axis angle will only have a minor effect on our results.

The second effect has to do with the presence of diffuse emission (emission from hot inter-stellar medium or from unresolved faint sources). Stobbart *et al.* (2006) investigated the diffuse emission of NGC 55 by extracting spectra representative of the residual disk emission and estimated the observed flux of the diffuse X-ray emission is at $\sim$3% of that of the resolved sources.

The third effect is caused by the high column density contours of 5×10^{21} cm^{-2} near the mid-plane (Stobbart *et al.* 2006) , which makes absorption a potentially significant problem for the detection of HMXB candidates. To determine the impact of such absorption, we investigate the distribution of all X-ray sources (AGN and XRBs) within the FOV in bins of 0.1 kpc from the mid-plane and perform a K-S test on the null hypothesis that their distribution is being drawn from a uniform one. At a confidence level of 95% the estimated p-value of 0.8% indicates that the distribution of all observed X-ray sources is not consistent with being flat, suggesting that the observed sources are not filling in for background ones that are not detected due to absorption, arguing for low incompleteness.

To quantitatively assess the effect of absorption through the edge-on star-forming gas disk of NGC 55, we assume that near the mid-plane at a distance of $\pm$1.2 kpc, which according to Davidge (2005), comprises the thin disk of NGC 55, most of the detected sources are those on the near side. To account for the sources on the far side that are

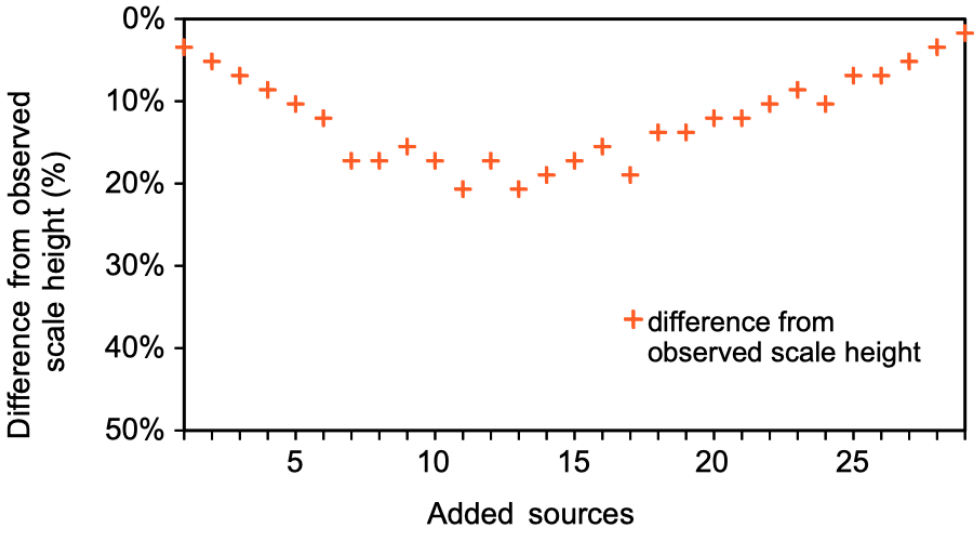

Figure 2.12: To account for the sources on the far side that are possibly undetected due to absorption, we add sources at the same distances from the mid-plane as the observed ones and calculate the variation in the determination of the scale height. The maximum deviation from the observed scale height is approximately 20% after the addition of 10 to 15 sources.

possibly undetected due to absorption, we add sources at the same distances from the mid-plane as the observed ones and calculate the variation in the determination of the scale height. The results are presented in Figure 2.12, where the maximum deviation from the observed scale height is approximately 20% after the addition of 10 to 15 sources.

We also assume that for the observed X-ray sources located within the thin disk and detected in both the soft (0.3 $\rightarrow$ 1 KeV) and hard (2 $\rightarrow$ 7 keV) X-ray bands, emission from hard X-rays is less affected by absorption. In Figure 2.13 we plot their luminosities in each band and in bins of 0.5 kpc vertical to the mid-plane. For the soft X-rays (orange line), there is a significant decrease towards the northern part (0.5 kpc) of the galaxy. Emission from hard X-rays (yellow line) is less affected and shows little variation as it passes through the thin disk. Assuming that the observed decrease in soft X-ray luminosity is caused by absorption, we quantify this at $\sim 3 \times 10^{37}$ erg s^{-1}. Since the average X-ray luminosity per source in the soft band is $\sim 2.5 \times 10^{36}$ erg s^{-1},

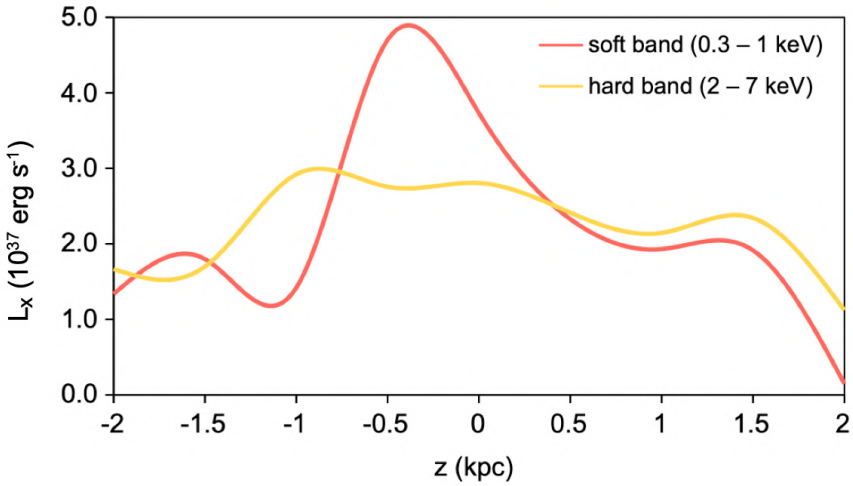

Figure 2.13: X-ray luminosities for sources detected in both the soft (0.3 → 1 KeV) and hard (2 → 7 keV) bands in bins of 0.5 kpc vertical to the mid-plane. For the soft X-rays (orange line), there is a significant decrease towards the northern part (0.5 kpc) of the galaxy which is estimated at $\sim 3 \times 10^{37}$ erg s^{-1}. Emission from hard X-rays (yellow line) is less affected and shows little variation as it passes through the thin disk.

the estimated absorption affects the emission from approximately 12 undetected X-ray sources, in agreement with our previous assumption.

Regarding the in situ formation of HMXBs in extra-planar regions, we concentrate on the population of early type stars in NGC 55, where most OB stars are found close to the mid-plane (Kudritzki *et al.* 2016) with very little star-forming activity outside the main body of the disk (Davidge 2005). We estimate the ratio of the relative Hα flux in extra-planar to planar regions as a measure of the fraction of early type stars in each region (assuming the same SFR history). Defining the regions as in (Davidge 2005), with the planar at a height of 2.2′ on either side of the mid-plane and the extra-planar falling between 2.2′ and 4.4′ off the mid-plane and using the starlight continuum subtracted Hα image of Section 2.2.2, the resulting ratio of only 6%, suggests it is unlikely that more than one or two HMXBs may have been formed in situ at large latitudes.

From the analysis of the issues that would bias the scale height of the vertical displacement of HMXBs, it occurs that the lower limit on the scale height is estimated at 0.33 kpc, as a result of the exclusion of the 15 “candidate HMXBs" with the largest

distances from the mid-plane as AGN interlopers. Furthermore, incompleteness can affect the upper and lower limits towards lower values by as much as 20%.

2.2.4 Center-of-mass transverse velocity of HMXBs

The companion stars of HMXBs are among the youngest stellar population in galaxies. Therefore the travel time and distance of HMXBs depend on the recent star formation history of the galaxy. Since there are no published star formation histories for NGC 55, we adopt HMXB travel times predicted by binary population synthesis codes for two different star formation history (SFH) models (shown in the top panel of Figure 2.14):

1. A flat model where stars are formed at a constant rate.
2. An exponentially declining model with a burst 100 Myr ago.

The star formation histories are displayed in the top panel of Figure 2.14 and are generated using a modified form of BSE, a binary population synthesis code described in Hurley *et al.* (2002) with updates found in Andrews *et al.* (2018) and its references. Default parameterisations and prescriptions are used. We use the statistical wrapper described in Andrews *et al.* (2018), to sample X-ray binaries with X-ray luminosities above 10^{36} erg s^{-1}. The synthetic populations are generated assuming different star formation histories, which we interpret as priors on our model distributions.

The vertical distance of HMXBs from the mid-plane is derived from the vertical distribution of stars corresponding to the star-formation activity off the galaxy's plane (star-forming distance), added to the convolution between the travel time and the centre-of-mass transverse velocity:

Vertical distance = star-forming distance + [Travel time × centre-of-mass transverse velocity × $\sin(\theta)\cos(\phi)$]

We assume the kick distribution to be isotropic, therefore the term $\sin(\theta)\cos(\phi)$ accounts for the random direction the kick will move the system, where θ is a polar

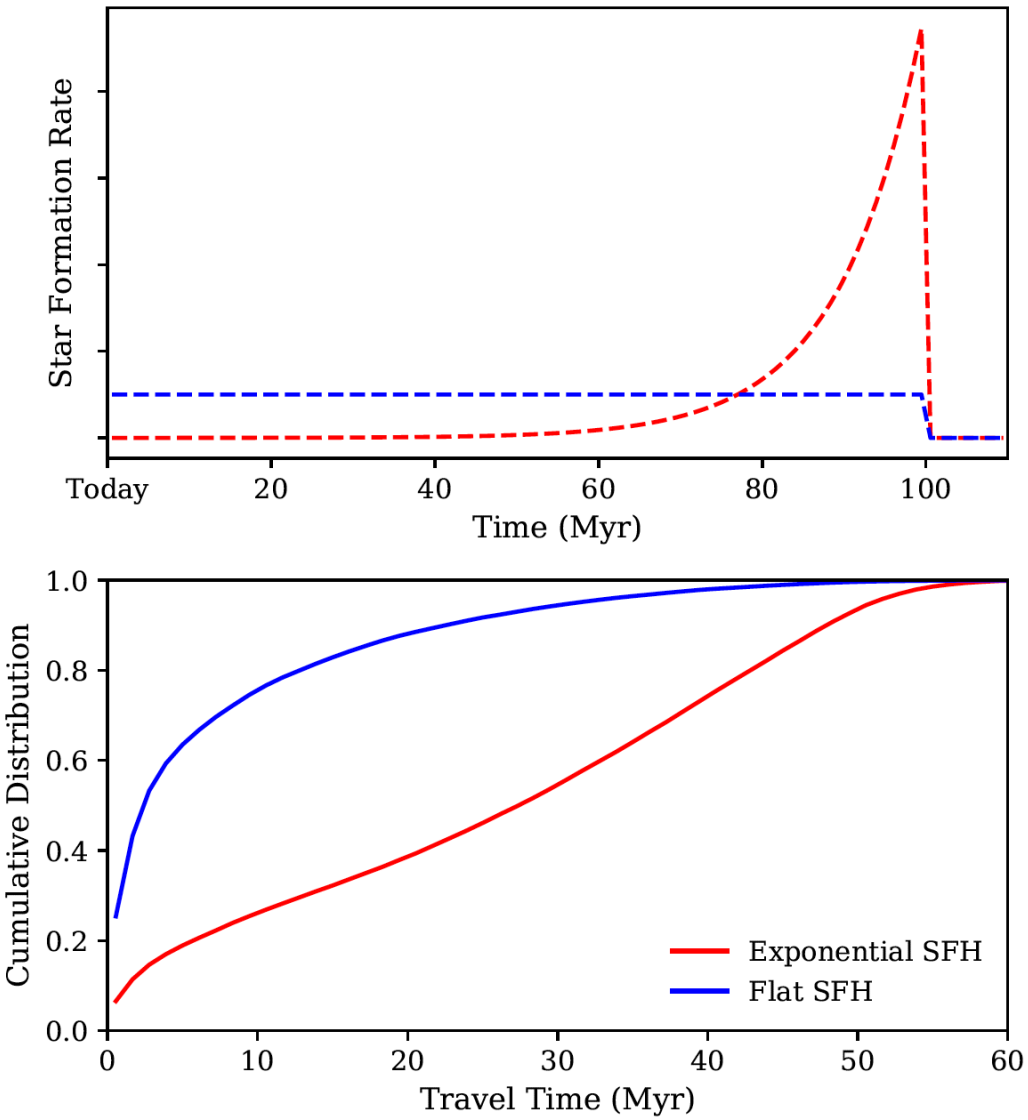

Figure 2.14: Top panel: Star formation history (SFH) models across the recent past of NGC 55. A flat model (blue dashed) where stars are formed at a constant rate and an exponentially declining model (red dashed) with a burst 100 Myr ago. Botton panel: Cumulative distribution of HMXB travel times adopted from binary population synthesis codes for the flat (blue) and exponential (red) SFH models. Depending on the star formation history, the travel time and therefore the travel distance of HMXBs can substantially change.

angle that defines the angle between the kick velocity and the direction of orbital motion and is randomly drawn from -1 $<$ cos(θ) $<$ 1, while ϕ is an azimuthal angle randomly varying between 0 and 2π.

To determine the center-of-mass transverse velocity distribution, we reverse the previous equation: we combine the observed sample's vertical distribution with randomly drawn vertical distances off the plane of NGC 55 (according to the exponentially declining distribution of star formation), travel time distributions (from binary population synthesis) and random polar and azimuthal angles to solve for the velocity distribution.

We determine the center-of-mass transverse velocity for three HMXB samples as in Section 2.2.3. In the first, the HMXB sample consists of all "verified HMXBs" as well as randomly selected combinations of 22 out of 37 "candidate HMXBs". In the second, the HMXB sample consists of "verified HMXBs" only. In the third, we have the "minimum " scale height sample, that consists of all "verified HMXBs" and "candidate HMXBs" excluding the 15 "candidate HMXBs" with the largest distances from the mid-plane. The results for the center-of-mass transverse velocity of HMXBs are presented in Table 2.4.

Figure 2.15 shows the center-of-mass transverse velocity distribution (normalised to the maximum value) for the first sample and for two different star-formation histories. The centre-of-mass transverse velocity for the exponential SFH model (red line) is 22 $\pm$ 6 km s^{-1} and for the flat SFH model (blue line) is 48 $\pm$ 9 km s^{-1}. For the second (the "verified HMXBs only") sample the centre-of-mass transverse velocity is 22 $\pm$ 6 km s^{-1} for the exponential and 41 $\pm$ 8 km s^{-1} for the flat SFH model. For the third (the "minimum scale height") sample, the centre-of-mass transverse velocity is 20 $\pm$ 5 km s^{-1} for the exponential and 34$\pm$7 km s^{-1} for the flat SFH model.

Table 2.4: HMXB center-of-mass transverse velocity

	velocity (km s^{-1})		displacement
HMXB sample	flat SFH	exp. SFH	(kpc)
verified, candidate[(1)]	48 ± 9	22 ± 6	0.57 ± 0.07
verified	41 ± 8	21 ± 6	0.39
verified, candidate[(2)]	34 ± 7	20 ± 5	0.33

(1) excluding 15 sources randomly selected
(2) excluding 15 sources with largest distances

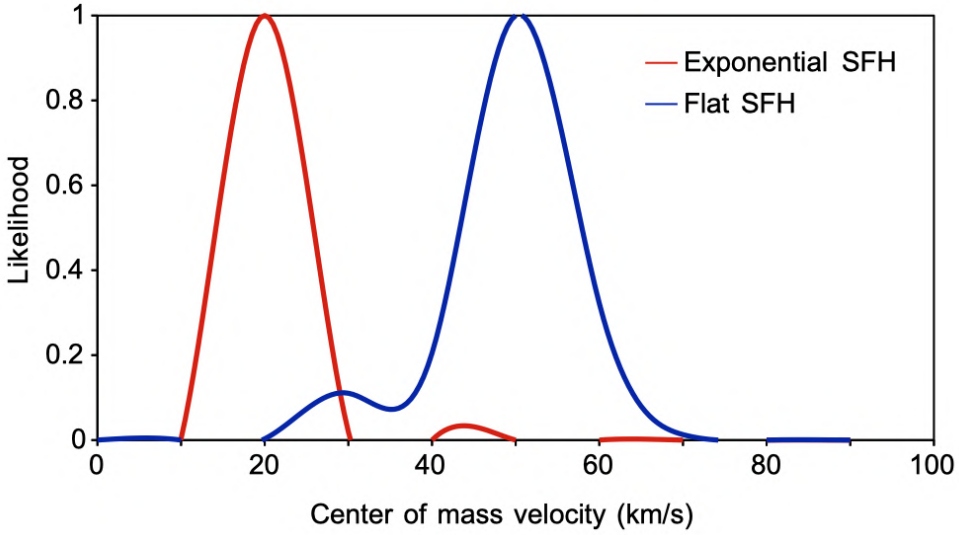

Figure 2.15: Normalised (to the maximum value) distribution of the centre-of-mass transverse velocity for the HMXB sample that consists of all "verified HMXBs" as well as randomly selected combinations of 22 out of 37 "candidate HMXBs", for two different star-formation histories. For the exponential SFH model (red line) the centre-of-mass transverse velocity is 22±6 km s^{-1} and for the flat SFH model (blue line) is 48±9 km s^{-1}.

2.3 Vertical distribution of MW HMXBs

The HMXB population in our Galaxy provides an excellent benchmark for: a) evaluating our statistical approach and b) comparing the vertical distribution of HMXBs between the two galaxies. Parallaxes from the second data release of Gaia (Gaia Collaboration 2018) allow us to measure their positions in the MW with unprecedented accuracy. We cross-correlate the HMXB catalog of Liu *et al.* (2006) with the Gaia DR2 catalog and we find matches for 36 out of the 114 known Galactic HMXBs. One of these matches (1H 1936+541) is excluded because most likely it is associated with the bright galaxy cluster G086.45+15.29 at a redshift of 0.260 (Andrade-Santos *et al.* 2017). Sources without Gaia DR2 counterparts either lack a previously associated optical counterpart or are too extincted to be observed by Gaia. For the 35 HMXBs, we measure their vertical distances from the mid-plane of the Galaxy by adopting a distance of the Sun from the Galactic plane at $h = 17 \pm 5$ pc (Karim & Mamajek 2017).

We repeat the same statistical analysis as in Section 2.2.2 where we treat the contribution of kicks as a Gaussian smearing function of standard deviation σ that spreads the vertical distribution of HMXBs around the Galaxy plane when applied on top of the star-formation activity distribution, which we consider is well represented by the vertical distribution of OB-stars in the Galaxy. We model the OB-stars distribution as an exponential function with a scale height of 103 ± 3 pc Kong & Zhu (2008) and derive that the difference between the scale heights of the vertical distribution of HMXBs and the vertical distribution of star-forming activity is 36 ± 3 pc (Figure 2.16).

To check the consistency of this result, we fit the distribution of vertical distances of HMXBs with an exponential function and find that the scale height of the vertical distribution of HMXBs in the Galaxy is 145 ± 23 pc (black dotted line in Figure 2.14) in general agreement with previous estimates at: 150 pc (Grimm *et al.* 2002), 240^{+90}_{-40} pc (Dean *et al.* 2005), 134^{+39}_{-25} pc (Bodaghee *et al.* 2007), 85^{+23}_{-15} pc (Lutovinov *et al.* 2013). When compared with the scale height of the distribution of OB-stars as in the previous

paragraph, the difference is at 42 ± 23 pc, consistent with the result from our statistical approach.

We note that from the distribution of HMXBs on the Galactic plane, Bodaghee *et al.* (2012) found much larger offsets between HMXBs and OB associations at 400±200 pc, with nine HMXBs located more than 1 kpc from their nearest OB association. The difference between the vertical and horizontal offsets of the HMXBs distribution is consistent with the kinematics of stellar systems due to Galaxy rotation and the kinematics of X-ray binary systems: Prior to the SN explosion, the orbit of binary systems in disk galaxies lay on the plane of the disk. The SN explosion induces a kick in addition to the initial motion of the progenitor on the Galactic plane.

On the other hand, the vertical displacement of HMXBs in NGC 55 is greater than in the Milky Way by an order of magnitude, despite the similar kick velocities the HMXBs receive in both galaxies. We attribute this difference to the greater gravitational potential of the MW that confines HMXBs more closely to the Galactic plane. More specifically, the stellar mass of NGC 55 is at $1.94 \times 10^9 M_\odot$ (Kudritzki *et al.* 2016) while for the Galaxy is 25 times greater, at $5.76 \times 10^{10} M_\odot$ (Licquia & Newman 2014). The local Galactic escape speed is estimated at 533 km s^{-1} (Piffl *et al.* 2014), while the escape velocity for NGC 55, using similar gravitational potential profiles as for the MW, is estimated at ∼100 km s^{-1}, which is consistent with the distribution of transverse velocities of HMXBs in NGC 55 (Figure 2.15). The typical kick velocities are well below the escape velocity of NGC 55, suggesting that most systems ought to remain bound to their host potential.

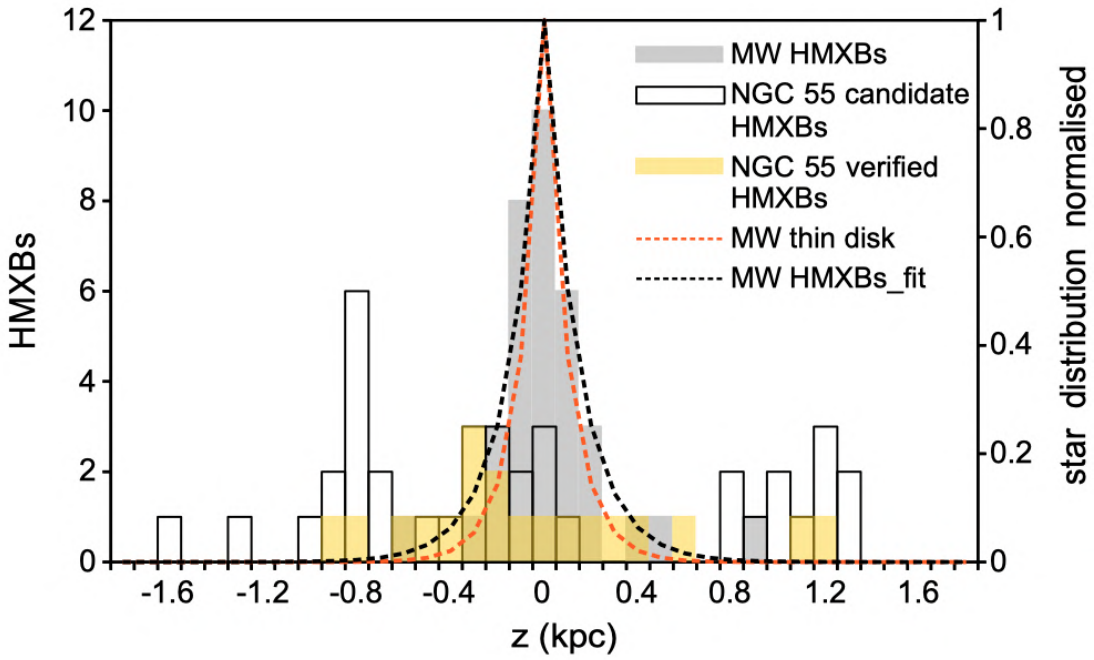

Figure 2.16: Vertical distribution of HMXBs in the MW (grey histogram) along with the best fit exponential function (black, dotted line) with a scale height of 145 ± 23 pc. The red, dotted line presents the vertical distribution of OB-stars in the MW with a scale height of 103 ± 3 pc (Kong & Zhu 2008). Applying our statistical approach, we find that the difference between the scale heights of the two distributions is 36 ± 3 pc. The white and yellow histograms show the observed vertical distribution of candidate and verified HMXBs in NGC 55. Despite the similar kick velocities the HMXBs receive in both galaxies, the distribution of vertical displacements in NGC 55 is much wider. We attribute the difference to the greater gravitational potential and therefore greater escape velocity of the Galactic disk that confines HMXBs more closely to the Galactic plane.

2.4 HMXB formation efficiency and metallicity

The formation rate of HMXBs follows closely the local SFR and metallicity (Fragos *et al.* 2013a, Antoniou *et al.* 2019). Since there is no local SFR data for NGC 55, we compare the HMXB formation efficiency in NGC 55 with the relevant efficiency in the SMC, LMC and the Milky Way, based on the average SFR of each galaxy (Table 2.5). We find that down to a luminosity of L_x=0.3 $\times$ 10^{36} erg s^{-1} the HMXBs/SFR in NGC 55 is 299^{+50}_{-46} (sources/$M_\odot$ yr^{-1}) assuming 41 HMXBs, which we consider as the most probable number of HMXBs in NGC 55 and SFR measurements from Weisz *et al.* 2011. In the case of LMC and SMC, down to a luminosity of L_x=3 $\times$ 10^{33} erg s^{-1} (Antoniou & Zezas 2016) we have 160^{+96}_{-64} (sources/$M_\odot$ yr^{-1}) and 480^{+400}_{-240} (sources/$M_\odot$ yr^{-1}) respectively (Antoniou & Zezas 2016, Harris & Zaritsky 2009). For the Milky Way we have 69 $\pm$ 17(sources/$M_\odot$ yr^{-1}) (Bodaghee *et al.* 2012, Licquia & Newman 2014). The errors are based on error propagation from the number of X-ray sources and the uncertainty on the SFR. The formation rate for the LMC and SMC is consistent with those calculated by Antoniou & Zezas (2016) given the local SFR of the episodes responsible for the formation of HMXBs. Taking into consideration the metallicity of each galaxy (Table 2.5), we see that the number of HMXBs per SFR is higher in galaxies with sub-solar metallicity. This is consistent with binary population synthesis models predicting more efficient HMXB production in metal poor environments. (Fragos *et al.* 2013a, Linden *et al.* 2010, Renzo *et al.* 2019).

2.5 Comparison with other galaxies

Measurements in the MW and the Magellanic Clouds show that the centre-of-mass transverse velocity of HMXBs is 12.4 ± 7.0 km s^{-1} for the LMC (Antoniou & Zezas 2016) and 16 km s^{-1} for the SMC (Coe 2005). The corresponding space velocities are 17.5 ± 9.8 km s^{-1} for the LMC (Antoniou & Zezas 2016) and 30 km s^{-1} for the SMC (Coe 2005). For the Milky Way, where van den Heuvel *et al.* (2000) derived proper motions from *Hipparcos* measurements, the transverse velocity of four SG-XRBs is 42±14 km s^{-1} and of 13 Be-XRBs is 15 ± 6 km s^{-1}. On the other hand, Bodaghee *et al.* (2012) used a sample of 79 Galactic HMXBs and estimated an average space velocity of 100 ± 50 km s^{-1}.

In this study, using travel time distributions derived from binary population synthesis codes based on two different SFH models we find that for a flat SFH model, which is typical of spiral galaxies like NGC 55, HMXBs are moving with typical transverse velocities between 34 and 48 km s^{-1}, consistent with space velocities of Milky Way HMXBs. For an exponential SFH model, with a starburst 100 Myr ago, HMXBs in NGC 55 have somewhat lower transverse velocities of approximately 21 km s^{-1}, consistent with the corresponding transverse velocity of HMXBs in the SMC and LMC.

Assuming that NGC 55 is reasonably accurately modelled with a flat star formation history, our results show that despite the similar kicks the HMXBs receive, the induced center-of-mass velocities are higher in NGC 55 than in the MCs. The differences can be attributed to pre and post SN orbital characteristics from which we can enrich our insight into the evolutionary process of XRB systems and revise the parameter space of theoretical models to reproduce the higher velocities by considering:

- Higher pre-supernova orbital velocities (Brandt & Podsiadlowski 1995).
- Larger masses of the secondary star (Brandt & Podsiadlowski 1995).

- Larger amounts of mass ejected during the SN explosion (Brandt & Podsiadlowski 1995).
- Increased natal kick velocities, that also affect the fraction of systems that remain bound (Kalogera 1996).

The comparatively high spatial velocities of HMXBs in NGC 55 suggest a larger fraction of SG-XRBs in NGC 55 than in the Milky Way and also hint for a small fraction of electron-capture SNe that impart very small kicks (Linden *et al.* 2009). The estimated centre-of-mass transverse velocities for each galaxy (LMC, SMC, MW, NGC 55) as well as the rest of the results of our analysis, are presented in Table 2.5.

Table 2.5: Comparison of HMXB displacement in different galaxies

	LMC	SMC	MW	NGC 55
Average displacement (kpc)	0.09 ± 0.05 [(1)]	0.07 [(2)]	0.40 ± 0.20 [(3)]	0.33 - 0.57 [(4)]
Transverse velocity (km s^{-1})	SG-XRBs 12.4±7.0 [(1)] Be-XRBs 10.8±7.3 [(1)]	16 [(2)] 13.1[(1)]	SG-XRBs 42±14 [(12)] Be-XRBs 15±6 [(12)]	21 [(13)] 34 - 48 [(14)]
Metallicity ($Z_\odot$)	0.4 [(1)]	0.2 [(1)]	1	0.4 [(5)]
SFR ($M_\odot$ yr^{-1})	$0.25^{+0.15}_{-0.10}$ [(6)]	$0.30^{+0.55}_{-0.15}$ [(6)]	1.66±0.20 [(8)]	$0.137^{+0.023}_{-0.021}$ [(11)]
Stellar mass ($M_\odot \times 10^9$)	2.70 [(7)]	0.31 [(7)]	57.6 [(8)]	1.94 [(9)]
HMXBs	40 [(1)]	144 [(1)]	114 [(3)]	41 [(10)]
HMXBs/SFR (sources/$M_\odot$ yr^{-1})	160^{+96}_{-64}	480^{+400}_{-240}	69±17	299^{+50}_{-46}

Notes: [(1)]Antoniou & Zezas (2016), [(2)]Coe (2005), [(3)]Bodaghee *et al.* (2012),[(4)]This study, [(5)]Kudritzki *et al.* (2016), [(6)]Harris & Zaritsky (2009),[(7)]van der Marel *et al.* (2009), [(8)]Licquia & Newman (2014), [(9)]Kudritzki *et al.* (2016),[(10)]this study based on Binder *et al.* (2015), [(11)]Weisz *et al.* (2011), [(12)]van den Heuvel *et al.* (2000),[(13)]This study, for an exponential SFH, [(14)]This study, for a flat SFH

3

XLF of nearby galaxies

The detection of discrete X-ray sources such as XRBs in our local universe enabled the statistical analysis of their populations in connection to the intrinsic properties (star formation rate, stellar mass, metallicity) of their host galaxies. The basic tool for the statistical analysis of XRB populations is the X-ray Luminosity Function (XLFs) that presents the number of XRBs as a function of their X-ray luminosity. The XLF of HMXBs in star-forming galaxies when normalised by the SFR of the host galaxies is described by a single power-law model with an index in the range between -1.5 and -1.8 (e.g. Grimm *et al.* 2003; Zezas *et al.* 2007; Mineo *et al.* 2012a; Wang *et al.* 2018; Lehmer *et al.* 2019) and a normalisation constant giving the number of HMXBs per SFR at a reference luminosity. The XLF of LMXBs in early-type galaxies when normalised by the $M_\star$ is described by a broken power-law with typical indices between -1.5 and -2.5 above a luminosity break-point L_b at $\sim 3.0 \times 10^{38}$ erg s^{-1} and between -2.0 and -3.0 at lower luminosities (e.g. Gilfanov *et al.* 2004; Kim & Fabbiano 2010; Zhang *et al.* 2012; Peacock & Zepf 2016; Lehmer *et al.* 2019).

In this chapter we study the demographics of a large population of XRBs in nearby galaxies. The sample is comprised of 10,099 X-ray sources in 319 nearby galaxies of all morphological types, covering a wide range of values in their intrinsic properties (SFR, $M_\star$, metallicity) and therefore representing all galactic environments. This is the most complete study of populations of XRBs in the literature, containing the largest sample of X-ray sources and galaxies and thus providing the best estimates for the aforementioned scaling relations of HMXBs and LMXBs.

3.1 Galaxy sample

Observations of nearby galaxies that contain X-ray point sources are retrieved from the *Chandra Source Catalogue 2.0 (CSC 2.0)* (Evans *et al.* 2020). Version 2.0 is the second major release of the catalog; the current minor release is version 2.0.1, updated on 2020 November 24. CSC 2.0 includes measured properties for 317,167 unique compact and extended X-ray sources in the sky, identified with the *Advanced CCD Imaging Spectrometer* (ACIS) in five energy bands: broad band (b)from 0.5 to 7.0 keV, ultrasoft (u)from 0.2 to 0.5 keV, soft (s)from 0.5 to 1.2 keV, medium (m) from 1.2 to 2.0 keV, hard (h) from 2.0 to 7.0 keV. In this study we use the ACIS detections in the broad band (b) from 0.5 to 7.0 keV. For further details on the structure of CSC 2.0 see Section 3.1.4 and on the photometric properties of CSC 2.0 see Section 3.2.1.

The following criteria are applied in order to create the galaxy sample:

1. Distance
2. Galactic footprint
3. Intrinsic properties
4. Availability of flux measurements

3.1.1 Distance

The goal of the analysis is to create the largest possible sample of discrete X-ray sources in nearby galaxies. At distances > 40 Mpc, source confusion severely limits our ability to resolve discrete sources in a galactic environment. Furthermore, for distances > 20 Mpc the minimum luminosity of the observed X-ray sources surpasses the value of 1×10^{38} erg s^{-1}. As a result, X-ray sources from galaxies at distances > 20 Mpc contribute only to the high luminosity end of the XLF, posing a significant bias in the creation of the XLF. We therefore include galaxies with distances up to 20 Mpc resulting in a sample of 386 nearby galaxies.

3.1.2 Galactic footprint

We use the D_{25} isophotal ellipse as the galactic footprint within which discrete X-ray sources are considered to be associated with the galaxy. The D_{25} is defined as the isophote ellipse with its centre at the centre of the galaxy and properties (coordinates, position angle, length of axes) according to the entries in the *HECATE*. Most of the observations included in CSC 2.0 target individual galaxies with the aimpoint usually positioned at the centre of the galaxy and the galaxy's D_{25} fully covered by the field-of-view of *Chandra*. However, there are observations with the aimpoint at specific (off-centre) regions as well as observations which partly cover the galaxy (particularly for the largest ones). The coverage of each galaxy is represented by the quantity f_{25} (available in the *HECATE*), defined as the fraction of the D_{25} included in the field-of-view of *Chandra*. The values of f_{25} are available in the *HECATE* and we consider as sufficiently covered, galaxies with $f_{25} > 0.7$ (Kovlakas *et al.* 2021), resulting in the exclusion of 19 galaxies.

3.1.3 Intrinsic properties

Three intrinsic properties of the host galaxies are considered in the analysis: SFR, $M_\star$, and metallicity (Z). These are retrieved from the *HECATE* in order to achieve

homogeneity (see Section 3.3.3 for the estimation of intrinsic properties). For 28 galaxies there is no available data in the *HECATE* and they are excluded.

3.1.4 Availability of flux measurements

For each galaxy of the sample, the flux of the population of X-ray sources must be available in CSC 2.0. Data that is available in CSC 2.0 is split into three main tables: the Master Sources Table, the Stacked Observation Detections Table, and the Per-Observation Detections Table. In the Master Sources Table, each row describes a source, whereas in the latter two tables, each row describes a detection. *Detections* are the photon counts that appear on the detector image, whereas *sources* are the detections interpreted as distinct X-ray sources (Evans *et al.* 2020). Therefore a X-ray source is represented by a single "Master source" entry, one or more "Per-Stack detection" entries (one for each stack in which the source has been detected) and by one or more "Per-Observation detection" entries, one for each observation in which the source has been detected. When a source is detected in several observations, its flux may vary from observation to observation. At the Master Sources level, CSC 2.0 constructs Bayesian blocks that group together those observations and within which the source may be considered to have a constant photon flux. The flux that is entered in the Master Sources Table is the one from the longest flux-ordered Bayesian block. We retrieve flux data from the Master Sources Table (see also Section 3.2.1) and we exclude 13 galaxies for which there is no available data in the Master Sources Table (there is available data only in the Per-Observation Detections Table). We also exclude seven more galaxies that contain only one X-ray source, and that source is associated with an AGN. The final galaxy sample consists of 319 galaxies. A subset of the galaxy sample with their corresponding intrinsic properties is presented in Table 3.1. The entire galaxy sample of the analysis is presented in the Appendix (Table 5.1).

Table 3.1: Galaxy sample and properties

Galaxy	Distance (Mpc)	Hubble Type (T)	Morph. Type	D_{25} (arcmin^2)	logSFR ($M_\odot$ yr^{-1})	log $M_\star$ ($M_\odot$)	Z	log L_{20} (erg sec^{-1})	N$_{scr}$	N$_c$	N$_{f/b}$
(1)	(2)	(3)	(4)	(5)	(6)	(7)	(8)	(9)	(10)	(11)	(12)
NGC6822	0.43	9.80	Irregular	180	-2.37	7.82	8.23	35.50	43	42.71	27.06
IC0010	0.75	9.90	Irregular	31	-1.38	8.57	8.04	35.87	40	37.46	5.57
NGC0598	0.85	5.90	spiral	1790	-0.64	9.45	8.42	36.05	714	410.38	189.22
NGC0205	0.87	-4.80	elliptical	122	-3.12	8.87	8.60	36.58	15	13.09	3.57
PGC029653	1.40	9.90	Irregular	18	-3.49	6.44	8.07	36.55	11	11.20	2.88
NGC0300	1.94	6.90	spiral	199	-1.32	9.26	8.55	36.67	83	80.84	36.74
NGC0055	2.00	8.80	spiral	143	-0.73	9.36	8.04	36.74	73	81.60	23.10
NGC4214	2.97	9.80	Irregular	28	-1.10	9.01	8.18	37.21	38	24.66	4.37

Column description: (1) Common galaxy name as in *NED*; (2) Distance in Mpc; (3) Classification according to HyperLEDA T; (4) Morphological type; (5) Area of D_{25} isophote in arcmin^2; (6) Star Formation Rate in $M_\odot$ yr^{-1}; (7) Stellar mass in $M_\odot$; (8) Metallicity in [12+log(O/H)]; (9) Sensitivity threshold, corresponding to the luminosity with 20% detection probability, estimated from average values; (10) Number of observed X-ray sources within the D_{25}; (11) Number of X-ray sources corrected for incompleteness; (12) Number of foreground/background X-ray sources (Kim *et al.* 2007)

3.2 X-ray source sample

3.2.1 Photometric properties of X-ray sources

Aperture photometry quantities in CSC 2.0 are derived from counts in source regions with elliptical apertures, with background estimated from counts in surrounding background regions. In the case of energy fluxes, the conversion from photons s^{-1} cm^{-2} to ergs s^{-1} cm^{-2} is performed by summing the photon energies for each incident source photon and scaling by the local value of the Auxiliary Response Function (ARF) at the location of the incident photon (Evans *et al.* 2020). The photometric properties of each distinct X-ray source are represented by one or more "per observation" entries in the Per-Observation Detections Table, and a single entry in the Master Sources Table. We extract the following properties for the ACIS broad (0.5-7.0 keV) band:

- **flux aper**: Net energy flux inferred from the source region aperture, derived from the longest block of a flux-ordered Bayesian Block analysis;
- **area aper**: area of the elliptical source region aperture in $arcsec^2$;
- **area aperbkg**: area of the annular background region aperture in $arcsec^2$;
- **cnts aper**: total counts measured in the source region;
- **cnts aperbkg**: total counts measured in the background region;
- **theta**: aperture off-axis angle in arcmin;
- **obsid**: observation identifier;
- **livetime**: effective observation exposure time.

The flux of each source is represented by the *flux aper* property which is extracted from the Master Sources Table. All other properties are extracted from the Per-Observation Detections Table. In case of multiple observations for a source, we select the entries of the observation (*obsid*) with the longest exposure time (*livetime*). The X-ray source sample consists of 10,099 X-ray sources, and a subset is presented in Table 3.2.

Table 3.2: List of X-ray sources and their photometric properties from CSC 2.0

Galaxy Name	Source Name	Flux aper (ergs/s/cm^2)	area aper (arcsec^2)	area aperbkg (arcsec^2)	cnts aper	cnts aperbkg	theta (arcmin)	obsid	livetime (sec)	Separation (arcsec)
NGC6822	J194456.5-144827	3.88	6.4	152	25	140	0.2	2925	28114	36.7
NGC6822	J194454.5-144713	4.46	4.2	1189	12	38	1.2	2925	28114	44.6
NGC6822	J194451.8-144658	15.71	6.3	1778	27	39	1.7	2925	28114	81.8
NGC6822	J194449.5-144704	5.21	5.6	1597	10	37	2.0	2925	28114	107.9
NGC6822	J194451.8-144919	3.28	5.0	1420	15	27	1.4	2925	28111	108.0
NGC6822	J194501.6-144908	4.71	5.0	1409	11	39	1.6	2925	28108	110.4
NGC6822	J194446.5-144852	3.73	8.8	2506	5	58	2.3	2925	28114	153.0
NGC6822	J194504.2-144552	1.93	12.6	1583	6	33	3.2	2925	28114	166.3
NGC6822	J194444.6-144807	21.80	11.3	623	43	25	2.8	2925	28114	168.5
NGC6822	J194459.9-144508	30.22	17.4	2183	80	46	3.3	2925	28114	171.9
NGC6822	J194447.5-144547	17.05	14.5	346	22	17	3.3	2925	28114	176.6

Column description: See text for the description of the photometric properties.

3.2.2 X-ray sources associated with Active Galactic Nuclei (AGN)

The presence of an active nucleus in the central region of galaxies can seriously contaminate the high luminosity end of the XLF, since AGN are detected as X-ray point sources that may exhibit luminosities well above 10^{39} erg s^{-1} (Ho & Ulvestad 2001; Ghosh *et al.* 2008). Information for the galaxies that contain AGN is derived from the *HECATE*, which in turn uses two sources:

(i) Stampoulis *et al.* (2019), who classified galaxies as AGN based on their location in optical emission-line ratio diagnostic diagrams, using spectroscopic data from the *MPA-JHU* catalogue.

(ii) She *et al.* (2017), who assembled a sample of 719 galaxies within 50 Mpc in *The Catalog of the Chandra Survey of Nearby Galaxies*.

In NGC4486 and NGC1068, there are more than one source (three and four sources respectively) at the central region (with distances from the aimpoint up to 2.57″ and 3.25″ respectively) with similar number of aperture and background counts. After visual inspection and since their detection cells overlap, all sources are excluded. In total, we exclude 130 X-ray sources, all of which are located within 3 ″ from the centre of the host galaxies.

3.2.3 Incompleteness and sources with low detection probability

Our sample of X-ray sources is incomplete due to the obvious fact that bright sources are easier to detect. Faint sources close to the detection limit are missed and this introduces a systematic bias, since the XLF becomes artificially flattened at the low luminosity (faint) end due to the missing sources. In order to correct for this flattening, we need to estimate the fraction of missing X-ray sources. We assume that the number of X-ray sources corrected for incompleteness is inversely proportional to the detection probability P for each X-ray source (Zezas *et al.* 2007). We use the parameterization of Wright *et al.*

(2015) for P as a function of the key source properties that allow the detectability of a source (source intensity, background surface brightness and off-axis angle) using the equation (Wright *et al.* 2015):

$$P = 1 - \mathbf{exp}\left(\frac{-C^{\lambda_1}}{10^{\lambda_2}}\right) \tag{3.1}$$

where C is the source intensity (in counts), and λ_1 and λ_2 are parameters that depend on the background surface brightness (in counts pixel^{-1}) and the off-axis angle for each source. The values of λ_1 and λ_2 for each source in Eq. 3.1 are based on the interpolation of tha data from Table 1 in Wright *et al.* (2015).

If N is the number of detected X-ray sources per galaxy, then the number of X-ray sources per galaxy corrected for incompleteness N_c is given by:

$$N_c = \sum_{i=1}^{N} \frac{1}{P_i} \tag{3.2}$$

In order to avoid in our analysis highly unreliable sources, such as sources with few counts and high background surface density, we select a detection probability threshold of $P = 20\%$ and we exclude from the final sample the X-ray sources with $P < 20\%$. As a result, we exclude 458 X-ray sources, with the final X-ray source sample consisting of 9641 sources.

Table 3.3: Parameters for the estimation of $N_{f/b}$

K	$S_{ref}{}^*$	$S_b{}^*$	γ_1	γ_2
1407^{+25}_{-48}	1	$19.2^{+1.3}_{-1.4}$	$1.64^{+0.01}_{-0.01}$	$2.48^{+0.05}_{-0.05}$

* S_{ref} and S_b in units of 10^{-15} erg cm^{-2} sec^{-1}

3.2.4 Contamination with foreground/background sources

In order to estimate the intrinsic population of XRBs per galaxy N_i, it is necessary to account for foreground (e.g. stars) and background (e.g. AGN) X-ray sources that are not associated with the galaxies but are projected onto the D_{25}. Since it is not possible to classify individual X-ray sources, we use deep field surveys to quantify the number of contaminants. From the Chandra Multi-wavelength Project (Kim *et al.* 2007) the following equation provides the number of X-ray sources N per deg^2 associated with the cosmic X-ray background (CXB) *a*bove a flux S_{20} which is the flux derived from the detection sensitivity limit L_{20} (which is the luminosity at the 20% completeness limit as defined in Section 3.3.2):

$$N_{f/b}(>S_{20}) = \begin{cases} K\left(\frac{1}{1-\gamma_1}-\frac{1}{1-\gamma_2}\right)\left(\frac{S_b}{S_{ref}}\right)^{(1-\gamma_1)} + \\ +K\left(\frac{1}{\gamma_1-1}\right)\left(\frac{S_{20}}{S_{ref}}\right)^{(1-\gamma_1)}, & S_{20} < S_b \\ K\left(\frac{1}{\gamma_2-1}\right)\left(\frac{S_b}{S_{ref}}\right)^{(\gamma_2-\gamma_1)}\left(\frac{S_{20}}{S_{ref}}\right)^{(1-\gamma_2)}, & S_{20} \geq S_b \end{cases} \tag{3.3}$$

where K is a normalisation constant, S_{ref} is a normalisation flux, S_b is the break flux at which the slope changes, γ_1 and γ_2 are faint and bright power indices. The values of the parameters for the broad energy band (0.5 - 8.0 keV) are presented in Table 3.3, adopted from Table 3 in Kim *et al.* (2007).

The number of foreground or background X-ray sources $N_{f/b}$ for each galaxy is estimated from Eq. 3.3 considering the extent of each galaxy (defined by the area of its

Table 3.4: Effect of contamination

Morphological type	$N_{f/b}/N_c$	average D_{25} ($arcmin^2$)	average L_{20} (10^{38} erg sec^{-1})
Spiral c,d,m	31.15 %	41.42	0.43
Irregular	23.60 %	19.96	0.27
Spiral a,b	16.93 %	21.91	0.44
Lenticular	14.62 %	12.88	0.49
Elliptical	6.79 %	13.61	0.65
All	19.44 %		

D_{25}) and its FOV coverage (defined by the the quantity f_{25}, see Section 3.1.2):

$$N_{f/b} = \frac{N(> S_{20})}{3600} \times D_{25} \times f_{25} \tag{3.4}$$

The value of $N_{f/b}$ for each galaxy is presented in Table 3.1 and in Table 5.1. The population of X-ray sources associated with each galaxy N_i is estimated after removing the background or foreground X-ray sources $N_{f/b}$ from the incompleteness corrected X-ray sources N_c.

The effect of the contamination for each morphological type of galaxies is presented in Table 3.4. The contamination is presented as the ratio $N_{f/b}/N_c$ of the background or foreground X-ray sources $N_{f/b}$ to the incompleteness corrected X-ray sources N_c. We also present the average values of D_{25} and L_{20} that according to Eq. 3.4 affect the estimation of $N_{f/b}$. The overall contamination is 19.44 % and mostly affects the spiral c,d,m (31.15%) and irregular (23.60%) galaxies. On the contrary, elliptical galaxies are very little affected (6.79 %). The high contamination in spiral c,d,m galaxies is due to their significantly larger extent, while for irregular galaxies is due to their low detection sensitivity limit L_{20} (the corresponding S_{20} is also low and according to Eq. 3.3 results in higher values of $N > S_{20}$). The low contamination in elliptical galaxies is due to their smaller extent and their higher detection sensitivity limit L_{20}.

Table 3.5: Morphological classification of galaxies

Category	de Vaucouleurs type	HyperLEDA type T
elliptical	E, E-S0	-5 to -3
lenticular	E-S0, S0, S0-a	-2.9 to 0
spiral a,b	Sa,Sb,Sab,SBa,SBb,SABa,SABb	0.1 to 4
spiral c,d,m	Sbc, Sc, Scd,Sm,SABc,SBc, SBcd,SBm,SABm	4.1 to 9.5
Irregular	I, IB	9.6 to 10

3.3 Properties of galaxies

The galaxies of the sample are first categorised according to their morphology. We then estimate the quantity L_{20}, which is the luminosity at the 20% completeness limit (see Section 3.3.2) that provides a measure of the detection sensitivity. Finally, we retrieve the values of the intrinsic properties SFR, M_* and metallicity from the *HECATE* and also estimate the value of the specific SFR (the SFR normalised to the M_*). The respective values are presented in Table 3.1.

3.3.1 Morphological classification of galaxies

The galaxies of the sample are categorised in five morphological categories according to the morphological classification of de Vaucouleurs and HyperLEDA (Table 3.5). Figure 3.1 shows the fraction of galaxies in our sample (number of galaxies in each category to the total number of galaxies) compared to the relevant sample (galaxies at distances < 20 Mpc) of the *HECATE*. The difference in the fraction of irregular galaxies is due to the fact that the *HECATE* includes a large population of irregular galaxies (mostly satellites of the Local Group galaxies), and only a small number of them has been observed with *Chandra*.

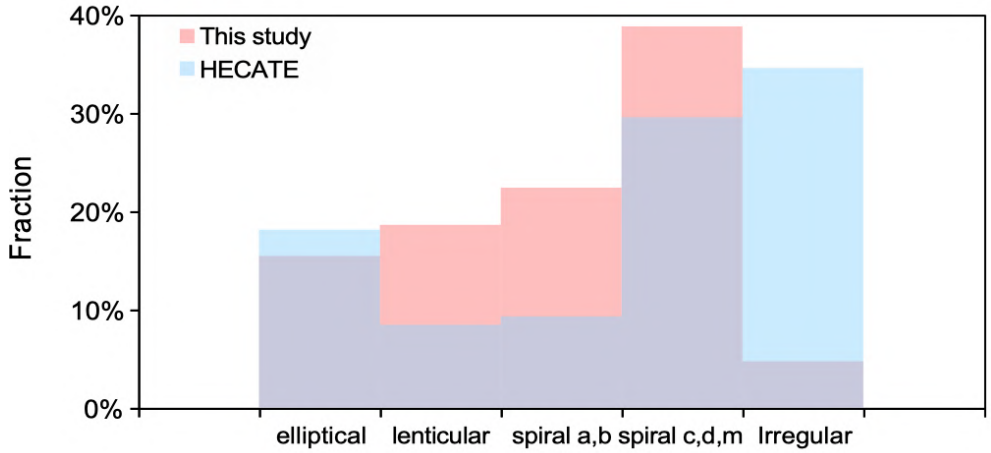

Figure 3.1: Fraction of galaxies in our sample (according to their morphological type) of our sample compared to the parent sample (galaxies at distances < 20 Mpc) of the *HECATE*. The difference in the fraction of irregular galaxies is due to the fact that the *HECATE* includes a large population of irregular galaxies (mostly satellites of the Local Group), and only a small number of them has been observed with *Chandra*.

3.3.2 Luminosity completeness limit

As a measure of the detection sensitivity for the available observations of each galaxy, we use the quantity L_{20} which is defined as the luminosity at the 20% completeness limit. This is based on the 20% flux limit S_{20} and the distance d of each galaxy (Table 3.1):

$$L_{20} = S_{20} * 4\pi d^2 \tag{3.5}$$

We use *CXC PIMMS* v4.11a to estimate S_{20} for a given *count-rate*. Taking for each galaxy the average (over all sources) values of λ_1, λ_2 and *livetime* (which is the observation exposure time as presented in Table 3.2), then from Eq. 3.1 solving for C, dividing by the average livetime and substituting $P = 20\%$ gives:

$$count - rate = \frac{[-10^{\lambda_2} ln(1-0.2)^{-1}]^{\lambda_1^{-1}}}{livetime} \tag{3.6}$$

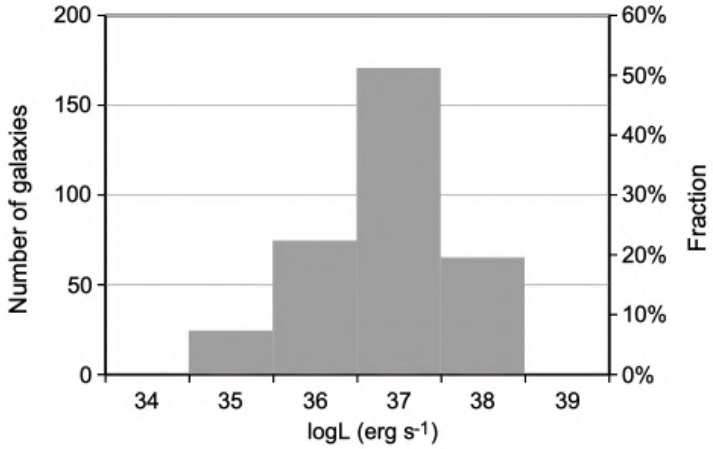

Figure 3.2: The sensitivity of the observations for our sample of galaxies as represented by the distribution of the 20% luminosity completeness limit L_{20} in luminosity bins of one dex. The sensitivity for the majority of the galaxies is within the 10^{37} erg sec^{-1} luminosity bin.

The estimated *count-rate* is used as input in *CXC PIMMS* v4.11a, which calculates the corresponding flux S_{20} by applying the following parameters:

- A Power Law model with a Photon Index of 1.7
- The Chandra Cycle (Mission) according to the *Obsid* of Table 3.2.
- The HI column density for the sky position corresponding to the coordinates of each galaxy using NASA's HEASARC NH Tool (heasarc.gsfc.nasa.gov).

Finally, substituting S_{20} in Eq. 3.5, L_{20} is estimated with the respective values shown in Table 3.1, while Figure 3.2 shows the distribution of L_{20} in luminosity bins of one dex. The sensitivity for the majority of galaxies falls within the 10^{37} erg sec^{-1} luminosity bin.

3.3.3 Intrinsic properties of galaxies

We retrieve from the *HECATE* values for the following galactic properties:

- *SFR*, which is associated with young stellar populations such as HMXBs;
- $M_\star$, which is associated with old stellar populations such as LMXBs;
- *Metallicity* which is significant for the formation efficiency of HMXBs.

The SFR estimates are based on photometric measurements from *IRAS* and *WISE* computing four different SFR indicators:

- Total-infrared (TIR) from *IRAS* at 24 μm, 60 μm and 100 μm (Dale & Helou 2002; Kennicutt & Evans 2012).
- Far-infrared (FIR) from *IRAS* at 60 μm and 100 μm (Helou & Walker 1988; Kennicutt 1998).
- 60 μm from *IRAS* (Rowan-Robinson 2001).
- 12 μm and 22 μm from *WISE* (Lang *et al.* 2016; Cluver *et al.* 2017).

The SFR value for each galaxy is obtained by homogenising the measurements based on the individual SFR indicators, using the TIR-based one as reference (Kovlakas *et al.* 2021).

$M_\star$ measurements are provided from the 2MASS K-band and the SDSS g-r colour photometries according to the mass-to-light ratio calibrations of Bell *et al.* (2003). We additionally estimate $M_\star$ values using the 2MASS K-band and SDSS g-r colour photometries according to the mass-to-light ratio calibrations of Zibetti *et al.* (2009), in order to directly compare our results with those of Lehmer *et al.* (2019) that also use the calibrations of Zibetti *et al.* (2009).

Metallicity values (defined using the oxygen abundance $[12+\log_{10}(\mathrm{O/H})]$) that include gas-phase metallicities, are based on *SDSS* spectroscopic data from the MPA-JHU catalogue (Kauffmann *et al.* 2003; Brinchmann *et al.* 2004; Tremonti *et al.* 2004), using the OIII-NII calibration (Pettini & Pagel 2004).

Based on the values of SFR and $M_\star$, we also estimate the sSFR (= SFR/$M_\star$) which is considered as a good indicator for the dominant population of XRBs.

The distribution of the SFR, $M_\star$, sSFR, and Z are presented in Figure 3.3 (blue columns) in comparison with the parent sample (galaxies at distances $<$ 20 Mpc) of the *HECATE* (red columns). It is evident that the intrinsic properties of our galaxy sample cover a wide range of sSFR, SFR, $M_\star$ and Z values.

The differences between the range of values of our sample and the *HECATE* are attributed to a large population of irregular dwarf galaxies (mostly satellites of Local Group galaxies), that have not been observed with *Chandra*. These galaxies have small values of SFR and M_* and they are located (red columns) in the region with log SFR $<$ -3 $M_\odot$ yr^{-1} (upper right panel of Figure 3.3) and log $M_* < 7$ $M_\odot$) (bottom left panel of Figure 3.3).

Figure 3.4 shows the locus of the sample of galaxies in the SFR - $M_\star$ plane. The grey dashed lines represent locations of constant log(sSFR) from -8 to -13 (yr^{-1}). The locus covers 5 dex in SFR and $M_\star$, significantly extended from the sample of previous studies such as in Lehmer *et al.* (2019), which is shown in Figure 3.4 with the black x-symbol. The red dashed line at log(sSFR) = -10.5 yr^{-1} represents the star formation main sequence (SFMS) (Pozzetti *et al.* 2010). Galaxies above the red line (higher sSFR) are considered as star-forming, while galaxies below (smaller sSFR) are considered as early-type. Figure 3.5 shows the locus of the sample of galaxies in the SFR - Z (upper) and SFR - sSFR (lower) planes.The red dashed line at log sSFR = -10.5 yr^{-1} in the SFR - sSFR (lower) plane, represents the value of log sSFR marking the transition from LMXB to HMXB dominated populations (Lehmer *et al.* 2019). The area with log(sSFR) $>$ -10.5 yr^{-1} is comprised of only spiral and irregular galaxies where HMXBs dominate the XRB population.

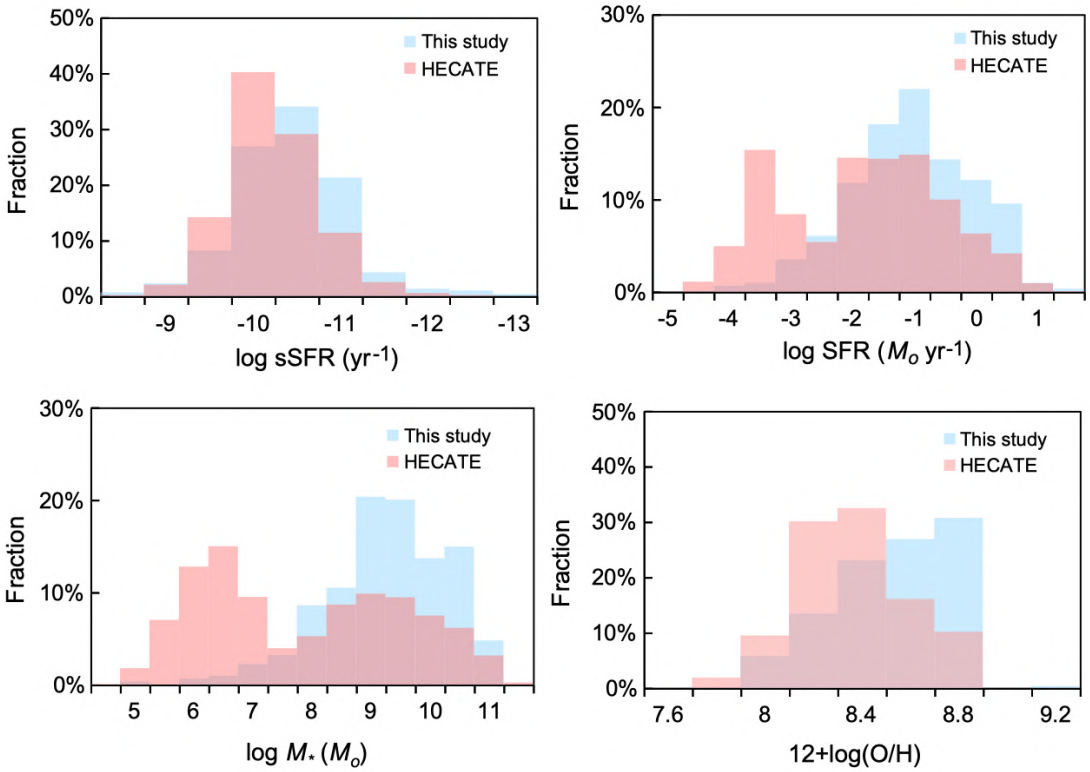

Figure 3.3: Distribution of the values of the intrinsic properties (sSFR, SFR, $M_\star$, metallicity) for the galaxy sample (blue histograms) compared to the parent sample of the *HECATE* for galaxies at distances < 20 Mpc, shown with red histograms.

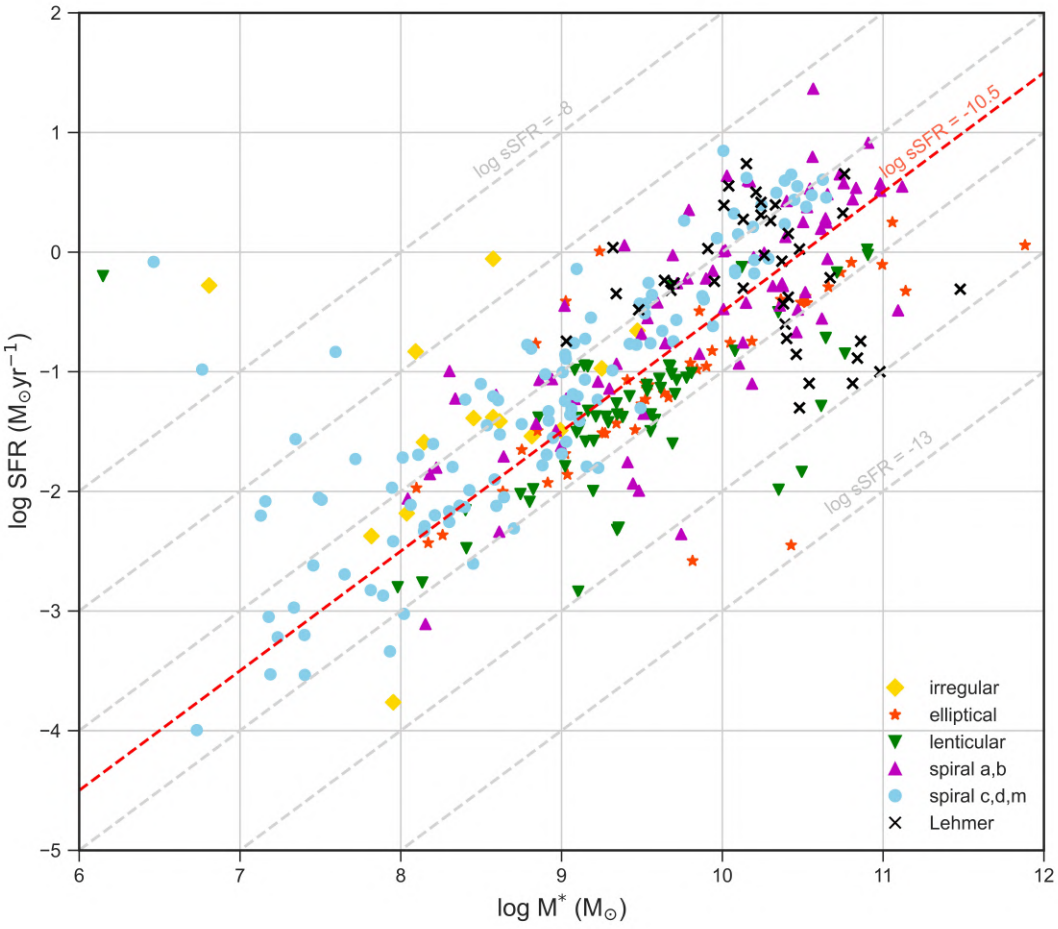

Figure 3.4: Distribution of the galaxy sample on the SFR-M_* plane per galaxy type. The grey dashed lines represent locations of constant log(sSFR) from -8 to -13 (yr^{-1}). The red dashed line at log sSFR = -10.5 yr^{-1} represents the star formation main sequence (SFMS) (Pozzetti *et al.* 2010). Galaxies above the red line (higher values of sSFR) are considered as star-forming, while galaxies below (smaller values of sSFR) are considered as early type. The galaxies shown with the black x-symbol represent the galaxy sample of Lehmer *et al.* (2019).

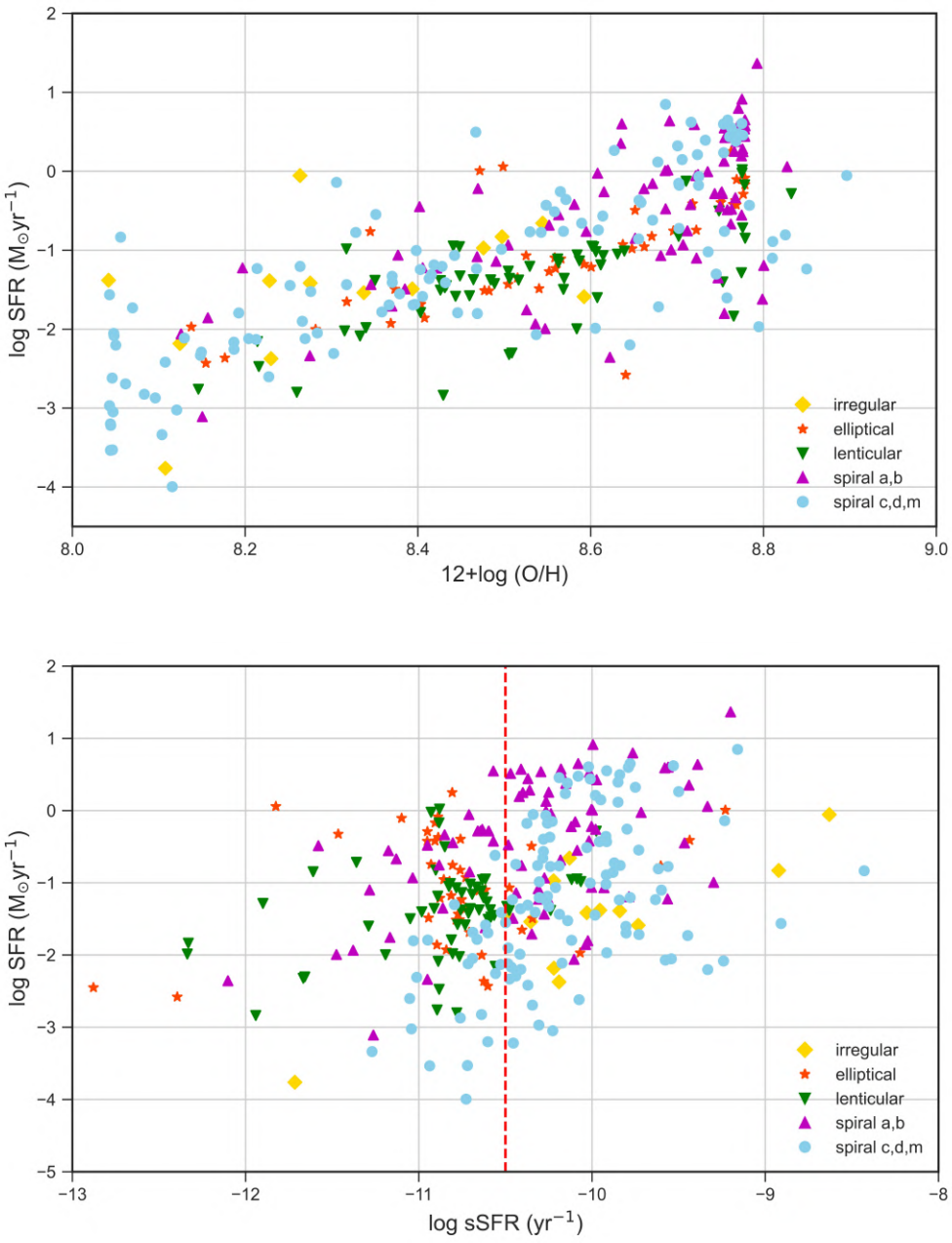

Figure 3.5: Distribution of the galaxy sample on the SFR - Z (upper) and SFR - sSFR (lower) panels. The red dashed line at log(sSFR) = -10.5 yr^{-1} in the SFR - sSFR (lower) plane, represents the value of log sSFR marking the transition from LMXB to HMXB dominated populations. The area with log(sSFR) > -10.5 yr^{-1} is comprised of spiral and irregular galaxies where HMXBs dominate the XRB population.

3.4 Cumulative Unbinned XLF

In order to present the distribution of the X-ray sources as a function of their luminosity without bias from binning effects, we create the cumulative unbinned XLF (Figure 3.6) of the X-ray point sources corrected for incompleteness N_c. We consider each morphological type independently. The contribution of the CXB sources $N_{f/b}$ which is included in N_c, can be estimated separately using Eq. 3.3 in Section 3.2.4 and is shown with the dotted lines in Figure 3.6.

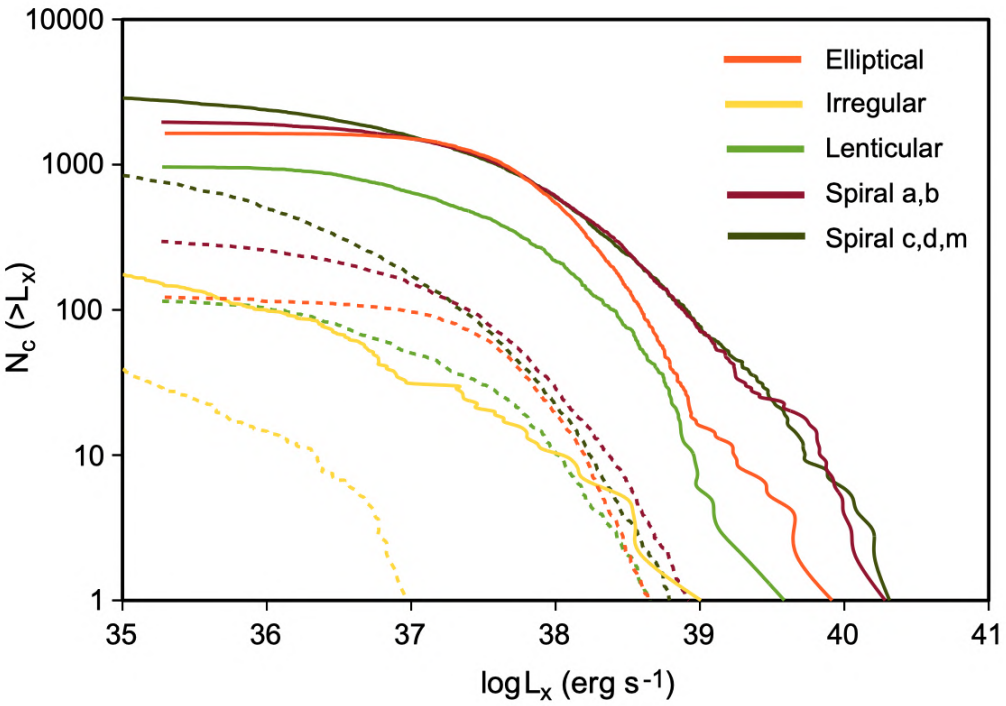

Figure 3.6: Cumulative unbinned XLF of the X-ray sources for each galaxy type. The XLFs are corrected for incompleteness. The contribution of CXB sources is shown with the dotted lines.

3.5 Differential XLFs

3.5.1 XLFs per morphological type

We construct the differential XLF of the X-ray sources associated with each galaxy by creating luminosity bins dL of constant width $logL = 0.05$ dex from $L_{min} = 1 \times 10^{35}$ erg s^{-1} to $L_{max} = 2 \times 10^{40}$ erg s^{-1} where L_{min} and L_{max} are the minimum and maximum luminosities in the sample of X-ray sources. The differential XLF constructed from all the galaxies of our sample contains approximately 80 X-ray sources per bin.

For each luminosity bin and for each galaxy we estimate the incompleteness corrected X-ray sources dN_c (Section 3.2.3). For the same bin we estimate the X-ray sources associated with the cosmic X-ray background $dN_{f/b}$ by differentiating Eq. 3.3 and following the procedure in Section 3.2.4.

The differential XLF of the X-ray sources associated with each galaxy dN_i per luminosity bin dL, is constructed by removing from the incompleteness corrected X-ray sources dN_c the background or foreground X-ray sources $dN_{f/b}$. In case the bin contains zero X-ray sources ($dN_c = 0$), then $dN_i = 0$ and the background or foreground X-ray sources $dN_{f/b}$ estimated for the bin are discarded. The differential XLF of the total galaxy sample and of each morphological type, is constructed by summing the corresponding dN_i and dividing by the luminosity bin dL. Figure 3.7 shows the differential XLF of each morphological type of galaxies (red dotted points) as well as of the total sample of galaxies (blue dotted points).

In this and the following sections we only consider incompleteness and contamination (from interlopers) corrected XLFs.

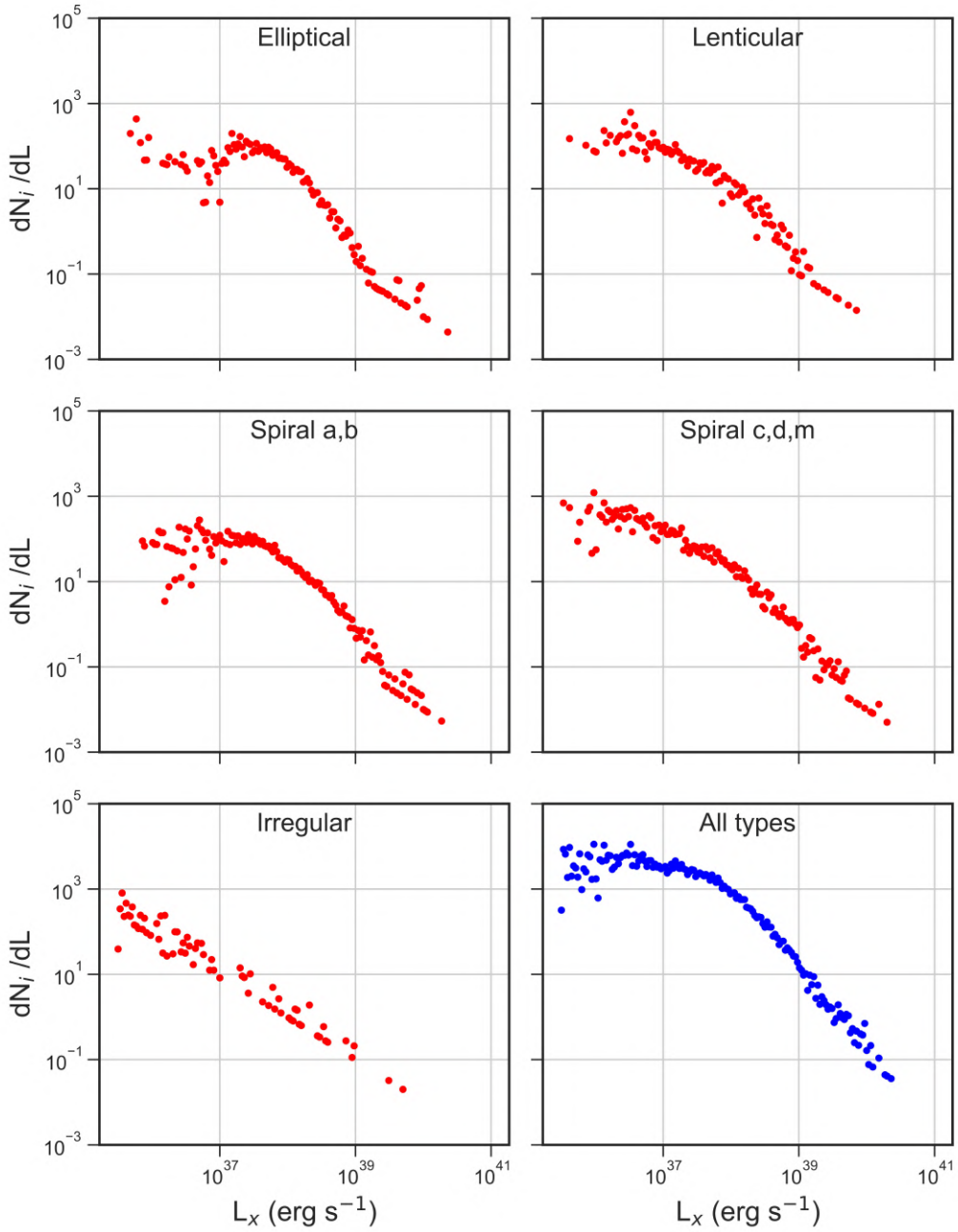

Figure 3.7: Differential XLFs of the number of X-ray point sources dN_i per luminosity bin dL of constant $logL = 0.05$ dex for each morphological type of galaxies corrected for incompleteness and from the contribution of foreground and background sources.

3.5.2 XLFs normalised to the SFR

As mentioned in Section 1.4, scaling relations emerge when the XLF of HMXBs is normalised to the SFR of the host galaxies. Since in star-forming galaxies the population of XRBs is dominated by HMXBs, we create a subgroup from the sample of galaxies that contains those with significant star-formation. As such, it can be determined based either on the morphological type, considering only spiral c,d,m and irregular type galaxies, or based on the sSFR considering only galaxies with log sSFR $>$ -10.5 yr^{-1} (see Section 3.3.3).

We examine both cases, starting from the star-forming subgroup based on the morphological type. Spiral a,b type galaxies are not included in the star-forming group since their population of XRBs has a non-negligible contribution of LMXBs.

We construct the differential XLF of the X-ray sources dN_i per luminosity bin dL as in Section 3.5.1 and normalise it to the SFR of the host galaxies contributing to the luminosity bin dL. We exclude the sources associated with the galaxies of the Local Group (with distances $<$ 1 Mpc), since the *Chandra* observations for the Local Group, in contrast with the observations of more distant galaxies, reach low luminosities resulting in high numbers of X-ray sources with luminosities $< 10^{36}$ erg s^{-1}, thus greatly affecting the low luminosity end of the XLF.

The results are shown in Figure 3.9 (blue dotted points) with the luminosity on the x-axis normalised to 10^{38} erg s^{-1} and designated as L_{38}.

We fit the data in Figure 3.9 by applying a power-law model of the form:

$$\frac{dN_i}{dL_{38}} = SFR * K_{HMXB} \times L_{38}^{-\alpha} \tag{3.7}$$

where:

- K_{HMXB} is the power-law normalisation in $sources(M_\odot\ \mathrm{yr}^{-1})^{-1}$
- α is the power-law slope

For fitting the data, we use of a Markov Chain Monte Carlo (MCMC) procedure that implements the Metropolis–Hastings sampling algorithm (Hastings 1970). The initial values of the input parameters K_{HMXB} and α are estimated using a least squares optimiser. The initial values are used as the starting position in the parameter space, in which the sampler performs the following loop: The position is perturbed randomly with a Gaussian distribution of mean 0 and standard deviation 1 to get a new trial position. We calculate the ratio between the likelihood at the previous position and the likelihood at this new trial position. We draw a random number between 0 and 1, and compare if the likelihood ratio is greater than this number. If the comparison is favorable, the sampler moves to the new position, and if not, it stays put and draws another trial position. Every new trial position is stored in a chain of length 100,000 (i.e. we perform 100,000 iterations). The first 1,000 entries during the "burn-in" phase are discarded, and we use the rest of the MCMC chain to compute the best-fit values and standard deviations.

The best-fit values of the model parameters K_{HMXB} and α (displayed with the green line in Figure 3.9) as well as their corresponding standard errors at the 1σ confidence level are:

- K_{HMXB} (at 10^{38} erg s^{-1}) = 2.82 ± 0.32 $sources(M_{\odot}\ \mathrm{yr}^{-1})^{-1}$
- α = 1.58 ± 0.26

The aforementioned values are estimated from the XLF that is constructed selecting a luminosity bin of dL = 0.05 dex. We next investigate the sensitivity of the scaling parameters K_{HMXB} and α for varying luminosity bins dL from 0.01 to 0.1 dex. We plot the results in Figure 3.8 where we show the variations of K_{HMXB}, α and the background or foreground X-ray sources $N_{f/b}$. We compare all three parameters with their values at the luminosity bin dL = 0.05 dex which we use as reference. The normalization K_{HMXB} (blue columns) varies inversely proportional to the number of CXB sources

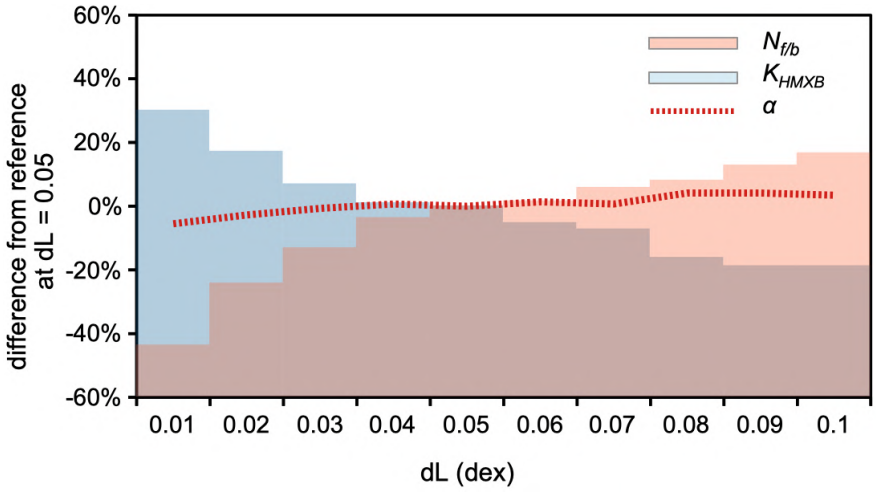

Figure 3.8: Sensitivity of parameters for varying luminosity bins dL. The normalization K_{HMXB} (blue columns) varies inversely proportional to the number of CXB sources $N_{f/b}$ (red columns). The variation is minimum for bin-widths between 0.04 and 0.06 dex. The slope α (red dotted line) does not vary. All variations are compared to the reference luminosity bin of $dL = 0.05$ dex

$N_{f/b}$ (red columns). For smaller (than the reference) luminosity bins, there are more bins that contain zero X-ray sources and therefore more background or foreground X-ray sources $dN_{f/b}$ are discarded (as described in Section 3.5.1). As a result, the remaining (small) bins contain a larger number of sources dN_i, thus increasing the normalization K_{HMXB}. On the other hand, for larger (than the reference) luminosity bins, there are less bins that contain zero X-ray sources and therefore less background or foreground X-ray sources $dN_{f/b}$ are discarded. As a result, the remaining (large) bins contain a smaller number of sources dN_i, thus decreasing the normalization K_{HMXB}. The slope α (red dotted line) does not vary.

For the star-forming subgroup of XRBs selected on the basis of log(sSFR) $>$ -10.5 yr^{-1}, following the same procedure for constructing the normalised to the SFR differential XLF and for fitting the data with an MCMC, the best-fit model parameters K_{HMXB} and α (displayed with the green line in Figure 3.10) as well as their corresponding standard errors at the 1σ confidence level are:

- K_{HMXB} (at 10^{38} erg s^{-1}) $= 2.24 \pm 0.27$ $sources(M_{\odot}\ \mathrm{yr}^{-1})^{-1}$

- $\alpha = 1.56 \pm 0.17$

Comparing the behaviour between the two subgroups, the estimated slopes α are very similar, indicating a strong correlation between the X-ray luminosity of HMXBs and the SFR of the hosting galaxies. On the contrary, the normalisation K_{HMXB} of the subgroup based on the sSFR is significantly lower. This is attributed to the lenticular, elliptical but mainly to the spiral a,b galaxies included in the subgroup (see Figure 3.5), that contain older stellar populations associated with LMXBs that scale with the $M_\star$ rather than the SFR of the host galaxy (for the contribution of LMXBs in spiral a,b galaxies see Section 3.5.4).

The best-fit XLF parameters for both star-forming subgroups are presented in Table 3.6.

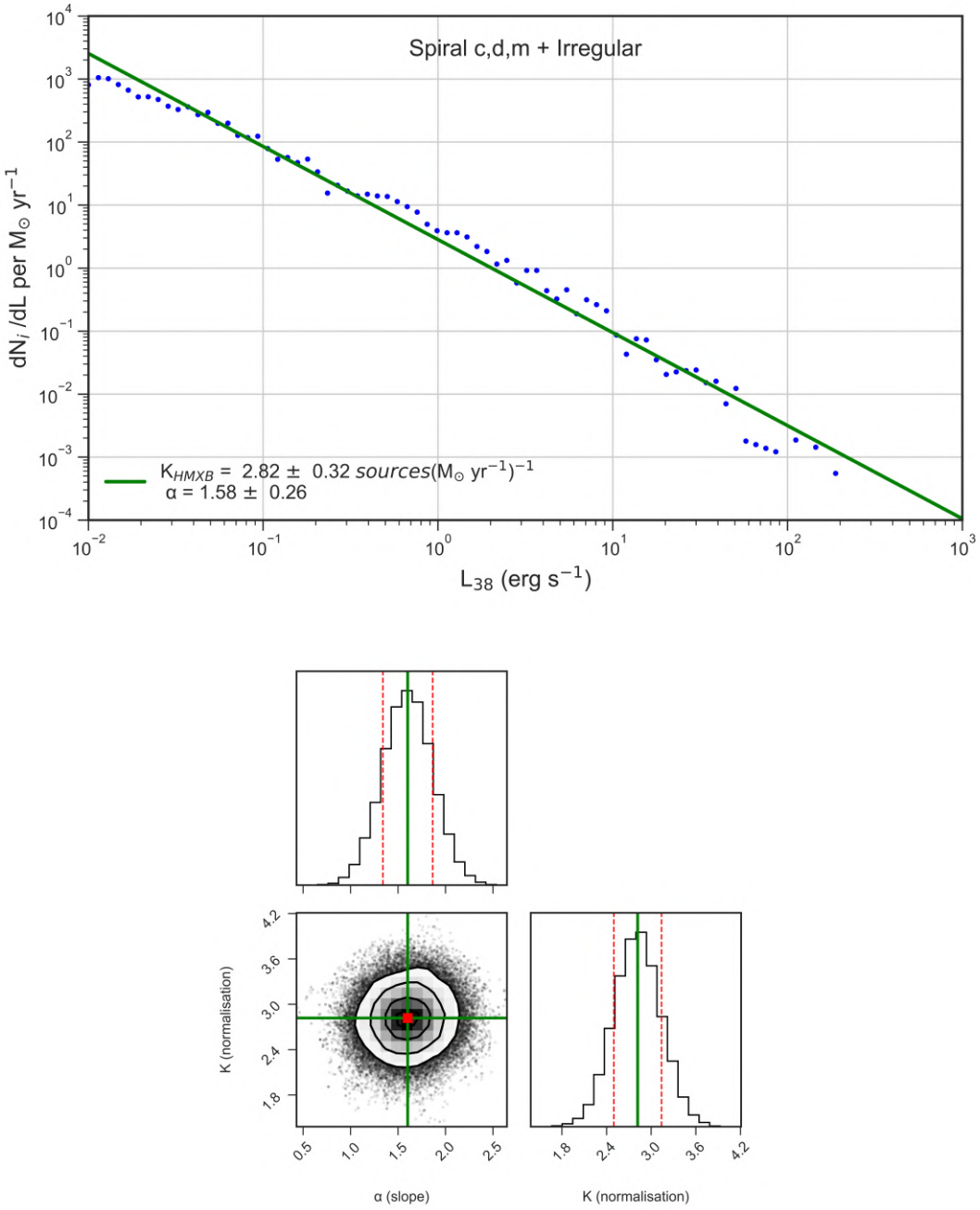

Figure 3.9: Differential XLF of XRBs in the star-forming subgroup of galaxies (**based on the morphological type**) normalised to the SFR of the hosting galaxies. The green line shows the best-fit power-law based on an MCMC fit of the data. The lower panel shows the variation of the model parameters as well as the best-fit values (green lines) and the corresponding standard errors (red dashed lines) at the 1σ confidence level. The legend shows the best-fit model parameters.

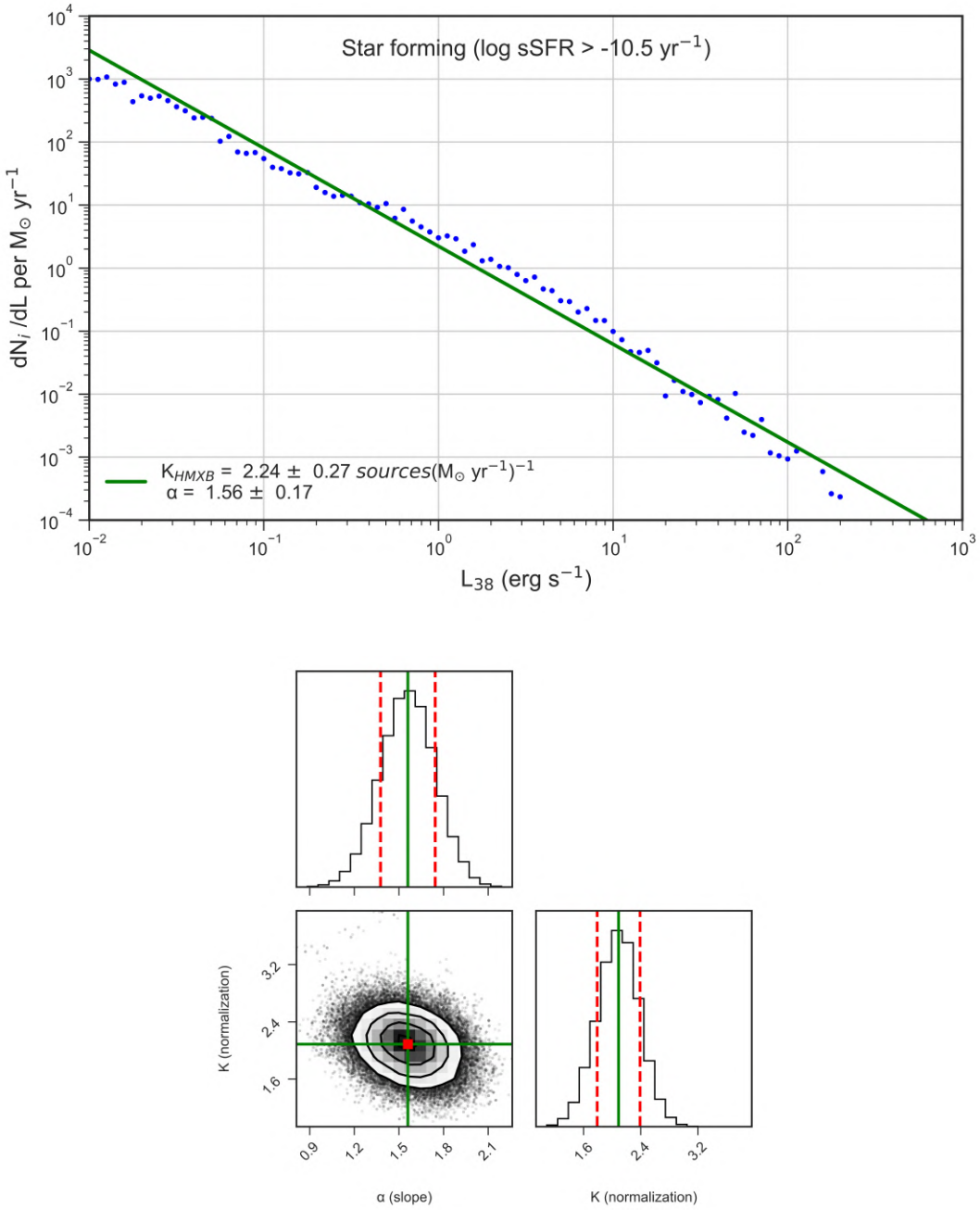

Figure 3.10: Differential XLF of XRBs in the star-forming subgroup of galaxies (**based on the sSFR**) normalised to the SFR of the hosting galaxies. The green line shows the best-fit power-law based on an MCMC fit of the data. The lower panel shows the variation of the model parameters as well as the best-fit values (green lines) and the corresponding standard errors (red dashed lines) at the 1σ confidence level. The legend shows the best-fit model parameters.

3.5.3 XLFs normalised to the stellar mass

Scaling relations can also be calculated for LMXBs. However, since LMXBs are associated with older stellar populations, they scale with the $M_\star$ of the host galaxies. Since the population of LMXBs is dominant in early-type galaxies and following the same approach as in Section 3.5.2, we create a subgroup from the sample of galaxies that contains the early-type ones. As such, it can be determined based either on the morphological type, considering only elliptical and lenticular type galaxies, or based on the sSFR, considering only galaxies with log(sSFR) $<$ -10.5 yr^{-1}.

Starting from the early-type subgroup based on the morphological type, we construct the differential XLF of the X-ray sources dN_i per luminosity bin dL as in Section 3.5.1 and normalise it to the $M_\star$ of the host galaxies contributing to the luminosity bin dL. The results are shown in Figure 3.11 (blue dotted points) with the luminosity on the x-axis normalised to 10^{38} erg s^{-1} and designated as L_{38}. We fit the data with a broken power-law model of the form:

$$\frac{dN_i}{dL_{38}} = M_\star * K_{LMXB} \times \begin{cases} L_{38}^{-\alpha_1}, & L_{38} < L_b \\ L_b^{\alpha_2-\alpha_1} L_{38}^{-\alpha_2}, & L_{38} \geq L_b \end{cases} \tag{3.8}$$

where:

- K_{LMXB} is the broken power-law normalisation in $sources(10^{11} M_\odot)^{-1}$ at 10^{38} erg s^{-1};
- α_1 is the broken power-law slope below the break luminosity L_b;
- α_2 is the broken power-law slope above the break luminosity L_b;
- L_b is the broken power-law break luminosity in units 10^{38} erg s^{-1}.

We fit the data using the same Markov Chain Monte Carlo (MCMC) procedure as in Section 3.5.2. The best-fit values of the model parameters as well as their corresponding standard errors at the 1σ confidence level are:

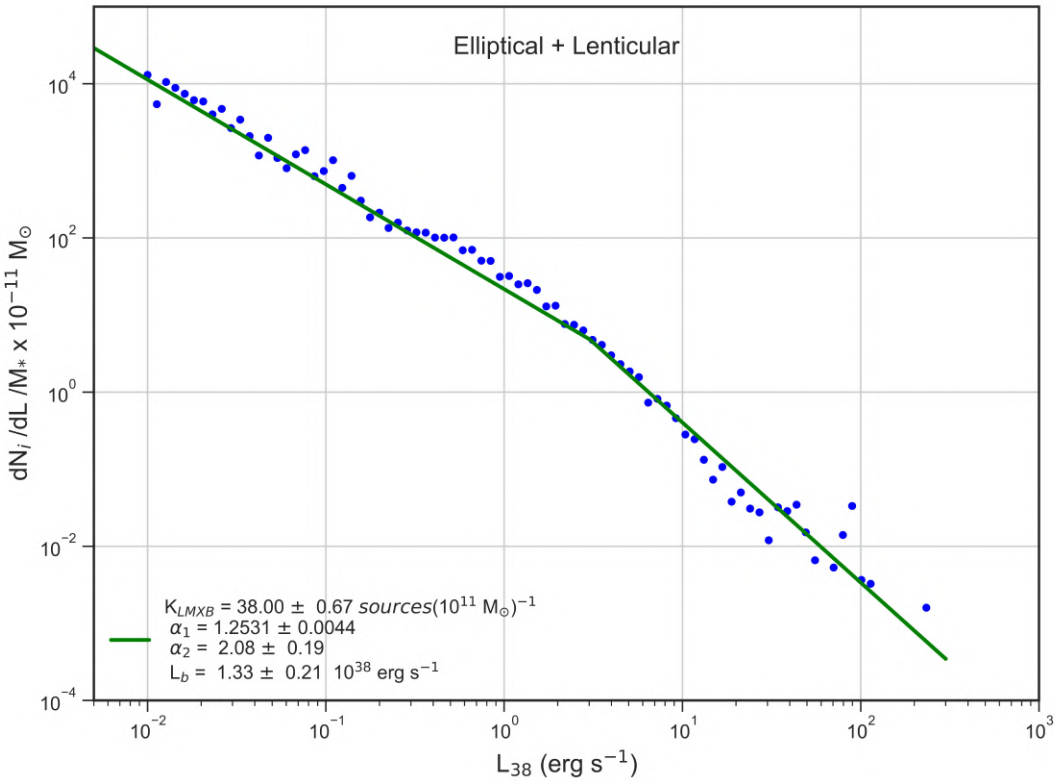

Figure 3.11: Differential XLF of XRBs in early-type galaxies (**based on the morphological type**) normalised to the $M_\star$ of the hosting galaxies. The green line shows the best-fit broken power-law based on an MCMC fit of the data. The legend shows the best-fit model parameters.

- K_{LMXB} (at 10^{38} erg s^{-1}) = 38.00 ± 0.67 *sources*$(10^{11}M_\odot)^{-1}$;
- α_1 = 1.253 ± 0.004;
- α_2 = 2.08 ± 0.19;
- L_b = 1.33 ± 0.21 (10^{38} erg s^{-1}).

The best-fit results are displayed with the green line in Figure 3.11, while Figure 3.12 shows the distribution and correlation of the broken power-law model parameters where the blue lines indicate the best-fit values and the red dashed lines the standard errors at the 1σ confidence level.

Following the same procedure for the early-type subgroup of XRBs in galaxies with log(sSFR) < -10.5 yr^{-1}, the MCMC best-fit values of the model parameters are:

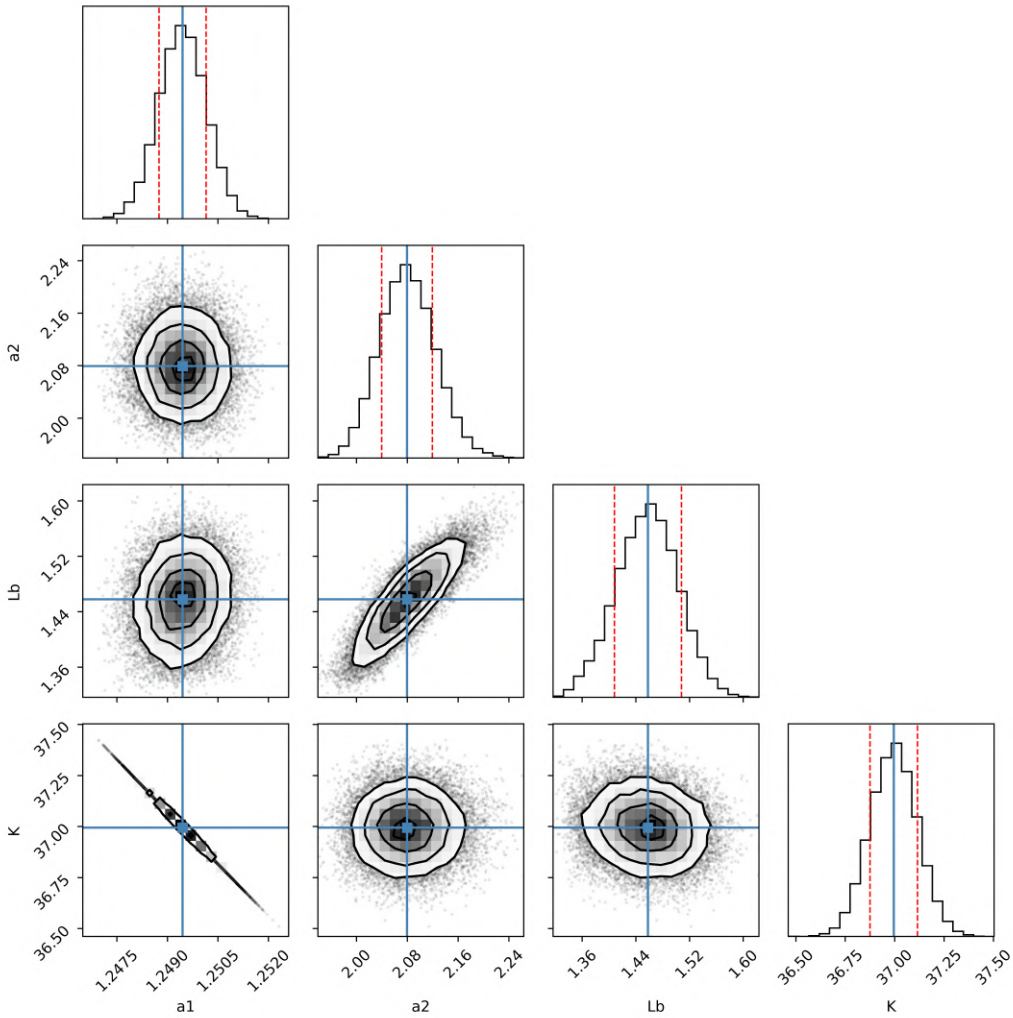

Figure 3.12: Corner plot of the broken power-law model parameters for XRBs in early-type galaxies (**based on the morphological type**) normalised to the $M_\star$ of the hosting galaxies. The blue lines indicate the best-fit values and the red dashed lines the standard errors at the 1σ confidence level.

- K_{LMXB} (at 10^{38} erg s^{-1}) = 26.92 ± 0.04 *sources*$(10^{11}M_{\odot})^{-1}$;
- α_1 = 1.231 ± 0.003;
- α_2 = 2.17 ± 0.01;
- L_b = 2.27 ± 0.01 (10^{38} erg s^{-1}).

The best-fit results are displayed with the green line in Figure 3.13, while Figure 3.14 shows the distribution and correlation of the broken power-law model parameters, where the blue lines indicate the best-fit values and the red dashed lines the standard errors at the 1σ confidence level.

Comparing the behaviour between the two subgroups, the estimated low and high luminosity slopes α_1 and α_2 have similar values, while the normalisation K_{LMXB} of the subgroup based on the sSFR is significantly lower. This is attributed to spiral galaxies included in the subgroup (see Figure 3.5), that contain stellar populations associated with HMXBs that scale with the SFR rather than the $M_{\star}$ of the host galaxy.

The best-fit XLF parameters for both early-type subgroups are presented in Table 3.6.

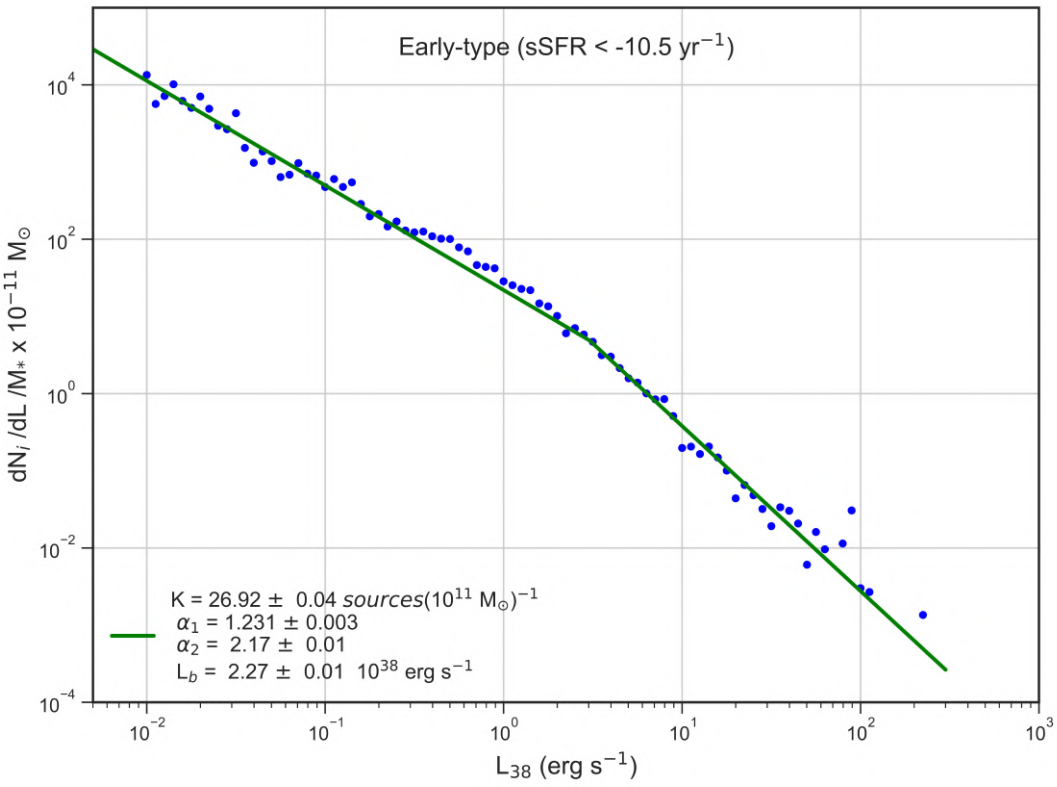

Figure 3.13: Differential XLF of XRBs in early-type galaxies (**based on the sSFR**) normalised to the $M_\star$ of the hosting galaxies. The green line shows the best-fit broken power-law based on an MCMC fit of the data. The legend shows the best-fit model parameters.

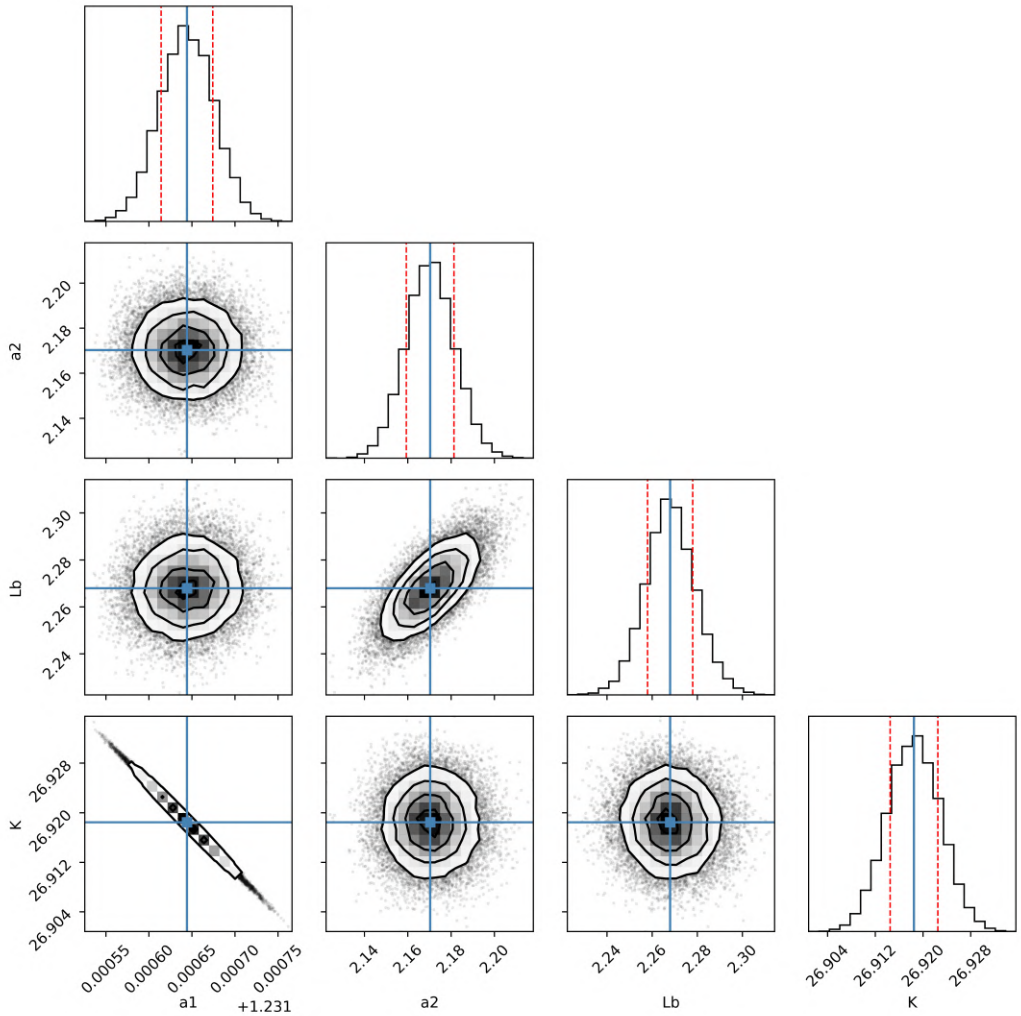

Figure 3.14: Corner plot of the broken power-law model parameters for XRBs in early-type galaxies (**based on the sSFR**) normalised to the $M_\star$ of the hosting galaxies. The blue lines indicate the best-fit values and the red dashed lines the standard errors at the 1σ confidence level.

3.5.4 Scaling relations for spiral a,b type galaxies

We have so far estimated the XLF scaling relations for galaxy types with XRB populations dominated by a specific type of XRBs. These scaling relations do not apply for galaxies with significant contribution from both types of XRBs, such as spiral a,b type galaxies in which apart from the population of HMXBs there is also a contribution from LMXBs. Instead of fitting the XLF, we investigate the respective contribution of HMXBs and LMXBs in spiral a,b galaxies by exploring the scaling relations of the number of XRBs in our galaxy sample when applying the best-fit values of the power-law and broken power-law slopes derived in Sections 3.5.2 and 3.5.3 respectively.

For a given luminosity bin dL, the number of XRBs dN is equal to the number of HMXBs (dN_{HMXB}) and LMXBs (dN_{LMXB}):

$$\frac{dN}{dL} = \frac{dN_{HMXB}}{dL} + \frac{dN_{LMXB}}{dL} \tag{3.9}$$

Substituting in Eq. 3.9 the values of $d\mathrm{N}_{HMXB}/d\mathrm{L}$ and $d\mathrm{N}_{LMXB}/d\mathrm{L}$ from Eq. 3.7 and Eq. 3.8 respectively:

$$\frac{dN}{dL} = SFR * K_H \times L^{-\alpha} + M_* * K_L \times \begin{cases} L^{-\alpha_1}, & L < L_b \\ L_b^{\alpha_2-\alpha_1} L^{-\alpha_2}, & L \geq L_b. \end{cases} \tag{3.10}$$

where α, α_1 and α_2 are the power-law and broken power-law slopes estimated in Sections 3.5.2 and 3.5.3, and K_H and K_L are the normalisations that determine the respective contribution of HMXBs and LMXBs.

The number of XRBs brighter than a luminosity $L_{35} = 10^{35}$ erg s^{-1} (which is the

minimum sensitivity for our sample of galaxies as shown in Figure 3.2) is given by:

$$N(> L_{35}) = \int \frac{dN}{dL} dL^{'} \tag{3.11}$$

Substituting Eq.3.10 in Eq.3.11, solving the integral and dividing by the SFR gives:

$$\frac{N}{SFR} = A(\alpha) * K_H + B(\alpha_1, \alpha_2, L_b) * K_L * sSFR^{-1} \tag{3.12}$$

where

$$A(\alpha) = \frac{1}{\alpha - 1} * L_{35}^{1-\alpha} \equiv A \tag{3.13}$$

$$B(\alpha_1, \alpha_2, L_b) = \left(\frac{1}{1-\alpha_1} - \frac{1}{1-\alpha_2} \right) * L_b^{1-\alpha_1} + \frac{1}{\alpha_1 - 1} * L_{35}^{1-\alpha_1} \equiv B \tag{3.14}$$

where L_b is the breaking luminosity set at 1.5×10^{38} erg s^{-1}.

Taking the logarithm of both sides in Eq.3.12 gives:

$$log\left(\frac{N}{SFR}\right) = log[(B * K_L) * 10^{-log(sSFR)} + (A * K_H)] \tag{3.15}$$

Since we have already estimated the number of X-ray sources associated with each galaxy N_i, then from 3.15 we can determine the normalizations K_H and K_L by fitting the data of the galaxy sample in a log(N_i/SFR) vs log(sSFR) plot (and substituting the power-law and broken power-law slopes α, α_1 and α_2, derived in Sections 3.5.2 and 3.5.3 respectively, to estimate A and B).

The MCMC best-fit to the data is shown with the red curve in Figure 3.15. Irregular and spiral c,d,m galaxies (our star-forming subgroup of Section 3.5.2) are shown with cyan crosses, while elliptical and lenticular galaxies (our early-type subgroup of Section 3.5.3) are shown with green crosses. Spiral a,b galaxies where the population of XRBs consists of both HMXBs and LMXBs are shown with magenta dots. The blue error bars represent median values of the distribution of galaxies included in bins of 0.25 log(sSFR).

The best-fit values of the normalisations K_H and K_L with the standard errors at the 1σ confidence level are:

- $K_H = 0.83 \pm 0.35$ $sources(M_\odot\ \mathrm{yr}^{-1})^{-1}$
- $K_L = 22.42 \pm 3.51$ $sources(10^{11} M_\odot)^{-1}$

Comparing the normalisation K_H with the normalisation K_{HMXB} for the star-forming galaxies (Section 3.5.2) the greater value of K_{HMXB} indicates a more efficient production of HMXBs in star-forming galaxies attributed to a population of XRBs with high luminosities (ULXs) in galaxies with low metallicity (see Sections 3.5.5 and 3.8).

Comparing the normalisation K_L with the normalisation K_{LMXB} for the early type galaxies (Section 3.5.3) the greater value of K_{LMXB} indicates a more efficient production of LMXBs in early type galaxies attributed to a population of XRBs associated with globular clusters, the density of which is greater in elliptical galaxies.

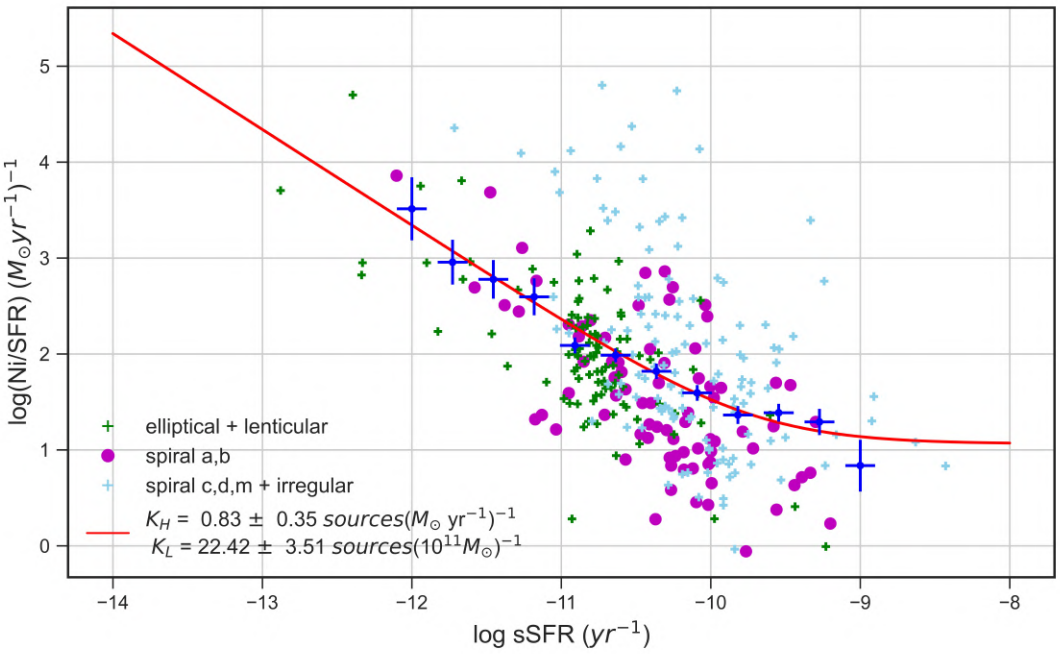

Figure 3.15: Estimation of the normalisations K_H and K_L that determine the number of HMXBs per SFR and LMXBs per M_* respectively, in galaxies with significant contribution from both types of XRBs such as the spiral a,b galaxies, shown with magenta dots. The red curve shows the MCMC best-fit to the data. Irregular and spiral c,d,m galaxies (our star-forming subgroup of Section 3.5.2) are shown with cyan crosses, while elliptical and lenticular galaxies (our early-type subgroup of Section 3.5.3) are shown with green crosses. The blue error bars represent average values of the distribution of galaxies included in bins of 0.25 log(sSFR). The legend shows the values of the best-fit model parameters with the standard errors at the 1σ confidence level.

3.5.5 Integrated X-ray luminosity scaling relation parameters

The integrated X-ray luminosity L_x of N number of X-ray binaries in a galaxy is given by:

$$L_x = \int_{L_{min}}^{L_{max}} L\frac{dN}{dL}dL' \tag{3.16}$$

where dN/dL the number of sources per luminosity bin as defined in Section 3.5.2 and in Section 3.5.3.

Considering that L_x is the sum of the luminosities emitted from LMXBs and HMXBs, which in turn are proportional to the respective $M^\star$ and SFR of the galaxy, then:

$$L_x = L_x(LMXB) + L_x(HMXB) = \alpha_{LMXB} * M^\star + \beta_{HMXB} * SFR \tag{3.17}$$

where α_{LMXB} is the integrated LMXB X-ray luminosity per unit stellar mass and β_{HMXB} is the integrated HMXB X-ray luminosity per unit SFR (e.g. Lehmer *et al.* (2019)) defined using Eq.3.16 and Eq.3.17 as:

$$\alpha_{LMXB} = \frac{1}{M^\star}\int_{L_{min}}^{L_{max}} L\frac{dN_{LMXB}}{dL}dL = \frac{L_x(LMXB)}{M^\star} \tag{3.18}$$

and

$$\beta_{HMXB} = \frac{1}{SFR}\int_{L_{min}}^{L_{max}} L\frac{dN_{HMXB}}{dL}dL = \frac{L_x(HMXB)}{SFR} \tag{3.19}$$

Dividing 3.17 by SFR and taking the logarithm of both sides we have:

$$log\frac{L_x}{SFR} = log(\alpha_{LMXB} * 10^{-logsSFR} + \beta_{HMXB}) \tag{3.20}$$

We can determine the parameters α_{LMXB} and β_{HMXB} by estimating the L_x for each galaxy and fitting the data in a $\log(L_x/\mathrm{SFR})$ vs $\log(\mathrm{sSFR})$ plot.

For each galaxy, the integrated luminosity L_x (in units of 10^{38} erg s^{-1}) of its X-ray binaries is given by the integral of 3.16, where the number of sources per luminosity bin dN/dL_{38} is described according to the morphological type of the galaxy by:

- A power-law with normalization K_p (that determines the number of sources at $L = L_{38}$) and slope α, for spiral and irregular galaxies (as in equation 3.7 but without normalising to the SFR of the hosting galaxy). Substituting in Eq. 3.16:

$$L_x = \int_{L_{min}}^{L_{max}} L_{38}(K_p L_{38}^{-\alpha}) dL_{38} = \frac{K_p}{2-\alpha}[L_{38}]_{L_{min}}^{L_{max}} \tag{3.21}$$

$$\begin{aligned} L_x &= \int_{L_{min}}^{L_b} L_{38}(K_{bp} L_{38}^{-\alpha_1}) dL_{38} + \int_{L_b}^{L_{max}} L_{38}(K_{bp} L_b^{(\alpha_2-\alpha_1)} L_{38}^{-\alpha_2}) dL_{38} \\ &= \frac{K_{bp}}{2-\alpha_1}[L_{38}]_{L_{min}}^{L_b} + \frac{K_{bp}}{2-\alpha_2} L_b^{(\alpha_2-\alpha_1)}[L_{38}]_{L_b}^{L_{max}} \end{aligned} \tag{3.22}$$

- A broken power-law of low-luminosity slope $\alpha_1 = 1.253$, high-luminosity slope $\alpha_2 = 2.08$, break luminosity $L_b = 1.33 \times 10^{38}$ erg s^{-1} (as estimated in Section 3.5.3) and normalization K_{bp} (that determines the number of sources at $L = L_{38}$) for elliptical and lenticular galaxies. Substituting in Eq. 3.16:

For solving Eq. 3.21 and Eq. 3.22, we select $L_{min} = 10^{35}$ erg s^{-1} (as in Section 3.5.4) and $L_{max} = 2 \times 10^{40}$ erg s^{-1} which is the maximum luminosity from the X-ray source sample.

The normalizations K_p or K_{bp} are determined for each galaxy individually, by creating the differential XLF for each galaxy and fitting the data with either a power-law (for

spiral and irregular galaxies) or a broken power-law (for elliptical and lenticular galaxies). The aforementioned procedure is applied for galaxies with more than six X-ray sources, the minimum number of sources with which a reasonable fit can be achieved. For more than half of the galaxies (55%) of the sample, the normalizations K_p and K_{bp} are estimated and fortunately all types of galaxies are represented.

Substituting the values of L_x from Eq. 3.21 and Eq. 3.22 in Eq. 3.20 we are able to construct the distribution of the integrated X-ray luminosity per unit SFR ($\log L_x/\mathrm{SFR}$) vs. log(sSFR) for galaxies with more than six X-ray sources as shown with the blue dotted points in Figure 3.16. The MCMC best-fit to the data is shown with the red line and the best-fit values of α_{LMXB} and β_{HMXB} as well as their corresponding standard errors at the 1σ confidence level are:

- $\log \alpha_{LMXB} = 29.85 \pm 0.71$ erg s^{-1} ${M_\odot}^{-1}$
- $\log \beta_{HMXB} = 39.37 \pm 0.17$ erg s^{-1} $(M_\odot\ \mathrm{yr}^{-1})^{-1}$

In Figure 3.16 we present with grey crosses the integrated luminosities of the galaxies with less than six sources, which are estimated by summing the luminosities of their X-ray sources. Since the galaxies with less than six sources show similar scatter to the galaxies with more than six sources, the estimation of the parameters α_{LMXB} and β_{HMXB} is not affected from the missing galaxies. The black triangles and the black dashed line in Figure 3.16 present the galaxies and the corresponding fit to the data from the sample of Lehmer *et al.* (2019). Comparing the two samples, it is evident that the scatter of our sample is significantly larger than the scatter from the sample of Lehmer *et al.* (2019), with our fit (red line) extending towards higher luminosities. We consider our sample more indicative, as it is (approximately five times) larger and represents all galactic environments. Galaxies containing X-ray binaries with super-Eddington luminosities (ULXs) greater than 5×10^{39} erg s^{-1} (well above the 10^{39} erg s^{-1} limit for super-Eddington luminosity) are highlighted with orange squares. These sources contribute to the excessive integrated luminosity of our sample.

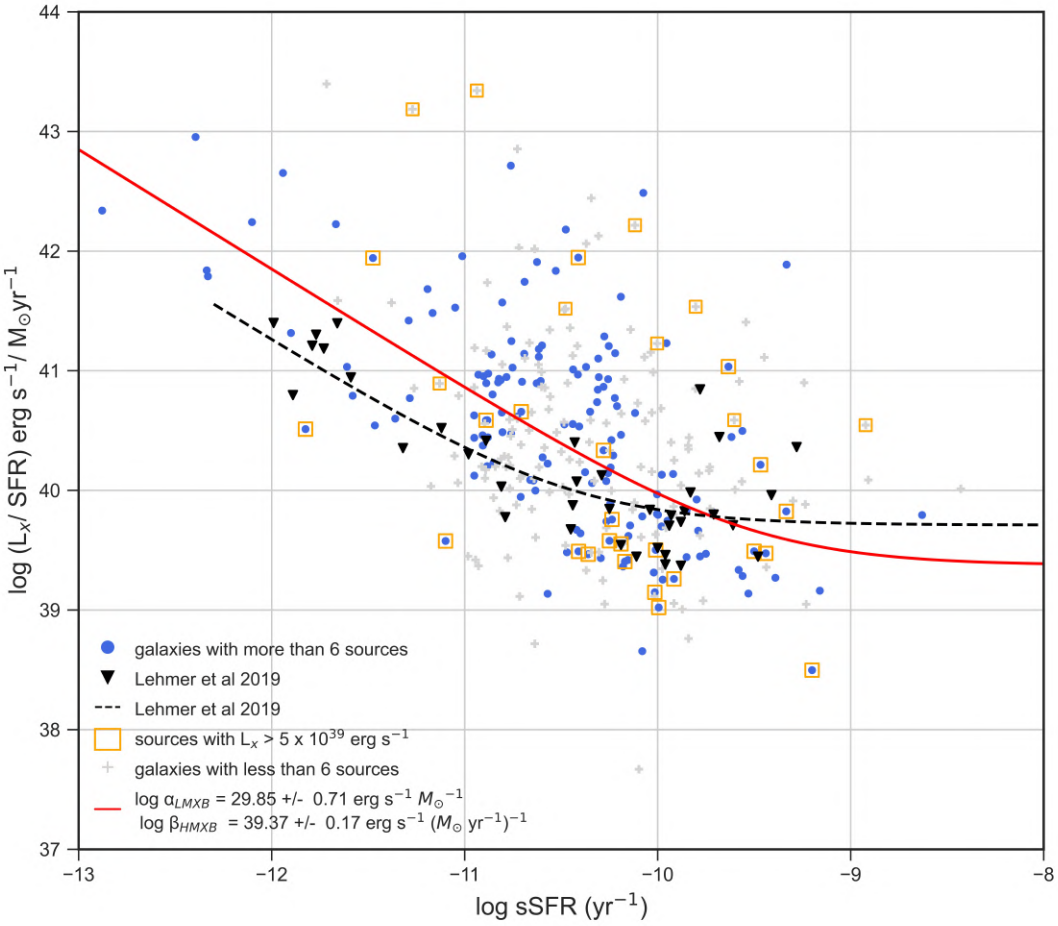

Figure 3.16: Distribution of the integrated X-ray luminosity per unit SFR (L_x/SFR) vs. sSFR for galaxies with more than six X-ray sources (blue dotted points) estimated from the procedure described in Section 3.5.5. The red line shows the best-fit to the data. Grey crosses show galaxies with less than six sources the integrated luminosity of which is estimated by summing the luminosities of their X-ray sources. The black triangles and the black dashed line present the galaxies and the corresponding fit to the data from the work of Lehmer *et al.* (2019). Galaxies that contain X-ray binaries (ULXs) with super-Eddington luminosities greater than 5×10^{39} erg s^{-1} are highlighted with orange squares.The legend shows the best-fit values with the standard errors at the 1σ confidence level.

3.6 Comparison with other studies

Table 3.6 summarises the values of the scaling parameters estimated in the previous sections, along with the relevant values from similar studies of Mineo *et al.* 2012b (M12), Zhang *et al.* 2012 (Z12) and Lehmer *et al.* 2019 (L19). The values in brackets present the results for the subgroups based on the sSFR.

Each study uses a different strategy in analysing the data, and specifically there are differences in the selection of:

- The galaxy sample
- The X-ray source sample
- The method used in the estimation of the intrinsic properties of galaxies
- The limiting detection sensitivity
- The area of the galaxy (galactic footprint) associated with the X-ray sources

In **M12**, they select star-forming galaxies with *Hubble type* T $>$ 0, high sSFR ($>$ 1 $\times$ 10^{-10} yr^{-1}) and distances up to 27 Mpc. They use observations with exposure-time (t_{exp}) $>$ 15 ks. The SFR is estimated using a complex SFR proxy that takes into account both the UV light escaping the galaxy and the IR emission of the dust heated by young stars (Bell 2003). The galactic footprint is a re-scaled D_{25} ellipse, defined as the region within which the contribution of CXB sources equals 30% of the total number of detected sources. They adopt a limiting detection sensitivity (% completeness level) of 20%. The galaxy sample includes 29 galaxies and the X-ray source sample includes 702 sources.

In **L19**, they select galaxies of all morphological types within a distance up to 30 Mpc, with B-band absolute magnitudes M_B $<$ -19 mag and inclination $<$ 70^o. The SFR is estimated using a combination of the *GALEX* FUV and *Spitzer* 24μm luminosities and the relation in Hao *et al.* (2011). The $M^\star$ is estimated following the relations in Zibetti

et al. (2009) based on optical and near IR imaging. The galactic footprint is the ellipse that traces the $K_S \sim 20$ mag arcsec^{-2} galactic surface brightness, with some central regions excised owing to the presence of AGNs or substantial source crowding. They adopt a limiting detection sensitivity (% completeness level) of 50%. The galaxy sample includes 38 galaxies and the X-ray source sample includes 2,478 sources.

In **Z12**, they select early-type elliptical and lenticular galaxies within a distance up to 25 Mpc, for which reliable age determination is available, with K_S luminosity $L_K > 8 \times 10^{10}\ L_{K,\odot}$ without ongoing or very recent star formation. The $M^\star$ is estimated from NIR data, using the K_S (2.16 μm) from *2MASS* and then converted to stellar mass following the relation in Bell & Kennicutt (2001). The galactic footprint is the D_{25} ellipse with the central 5″ region excluded. They adopt a limiting detection sensitivity (% completeness level) of 60%. The galaxy sample includes 20 galaxies and the X-ray source sample includes 2,074 sources.

In our analysis, we select galaxies of all morphological types within a distance up to 20 Mpc, with with no other constrains. Host galaxy properties are based on the *HECATE* (see Section 3.3.3). The galactic footprint is the D_{25} ellipse and the detection sensitivity (% completeness level) is set at 20%. The galaxy sample includes 319 galaxies and the X-ray source sample includes 9,641 sources.

The galaxy and X-ray source sample selection criteria from all studies are summarised in Table 3.7.

Table 3.6: Best-fit scaling parameters

Parameter	Thesis	L19	M12	Z12
K_{HMXB} *sources*$(M_\odot\ \mathrm{yr}^{-1})^{-1}$	2.82 ± 0.32 [2.24 ± 0.27]	1.96 ± 0.14	2.68 ± 0.13	
α	1.58 ± 0.26 [1.56 ± 0.17]	$1.65\ ^{+0.03}_{-0.02}$	1.58 ± 0.02	
K_{LMXB} *sources*$(10^{11} M_\odot)^{-1}$	38.00 ± 0.67 [26.92 ± 0.04]	$33.8\ ^{+7.3}_{-3.6}$		41.5 ± 11.5
α_1	1.253 ± 0.004 [1.231 ± 0.003]	$1.28^{+0.06}_{-0.09}$		$1.02\ ^{+0.07}_{-0.08}$
α_2	2.08 ± 0.19 [2.17 ± 0.01]	$2.33\ ^{+0.27}_{-0.21}$		$2.06\ ^{+0.06}_{-0.05}$
L_b $(10^{38}$ erg s$^{-1})$	1.33 ± 0.21	$1.48^{+0.70}_{-0.66}$		$0.546^{+0.043}_{-0.037}$
log α_{LMXB} erg s^{-1} $M_\odot{}^{-1}$	29.85 ± 0.71	$29.25\ ^{+0.07}_{-0.06}$		29.2 ± 0.1
log β_{HMXB} erg s^{-1} $(M_\odot\ \mathrm{yr}^{-1})^{-1}$	39.37 ± 0.17	$39.71\ ^{+0.14}_{-0.09}$	39.67 ± 0.06	
K_H *sources*$(M_\odot\ \mathrm{yr}^{-1})^{-1}$	0.83 ± 0.35			
K_L *sources*$(10^{11} M_\odot)^{-1}$	22.42 ± 3.51			

Table 3.7: Galaxy and X-ray source samples of similar studies

	Thesis	L19	M12	Z12
Galaxy type	All types	All types	Spiral c,d,m Irregular	Elliptical Lenticular
Selection criteria	None	$M_B <$ -19 mag	sSFR $> 1 \times 10^{-10}$ yr^{-1}	Small SFR $L_K > 8 \times 10^{10}\ L_{K,\odot}$
Distance (Mpc)	20	30	27	25
Number of galaxies	319	38	29	20
Number of X-ray sources	9,641	2,478	702	2,074
SFR estimation	*HECATE*	L_{FUV} and $L_{24\mu m}$.	L_{NUV} and L_{IR}.	
M^* estimation	*HECATE*	L_K and *g-i* color		K_S at 2.16 μm
Detection sensitivity L_{lim} (% completeness level)	20	50	20	60
Galactic footprints	D_{25}	$K_S \sim 20$ mag arcsec^{-2}	re-scaled D_{25}: $N_{CXB}/N_{tot} = 30\%$	D_{25} excluding the central 5$''$

Comparing the results from our analysis with those from the aforementioned studies of **M12**, **Z12** and **L19** we find that:

- For the shape and scaling with the SFR of the differential XLF of XRBs in star-forming galaxies, the power-law slope α is in very good agreement with the studies of **M12** and **L19**. The normalisation K_{HMXB} is in good agreement with the study of **M12** but is higher than the corresponding value of **L19**. We attribute the difference to our: i) galaxy and X-ray source samples that contain more low metallicity star-forming galaxies with efficient HMXB production, ii) lower detection sensitivity limit L_{lim} (20% compared to 50% of **L19**) that results in more sources per bin and iii) lower luminosity bin dL (0.05 dex compared to 0.057 dex of **L19**) that according to Figure 3.8 leads to a higher K_{HMXB}.

- The shape and scaling with the $M_{\star}$ of the differential XLF of XRBs in early-type galaxies as described by the parameters K_{LMXB}, α_1, α_2 and L_b, are in good agreement with the studies of **Z12** and **L19**.

3.7 XLFs as a function of specific SFR

We construct XRB XLFs in bins of sSFR aiming to utilize the sSFR as an indicator for the dominant population of XRBs. When analyzing XRB XLFs in bins of sSFR, we should be able to see the transition in XLF shape and normalization from the almost "pure" HMXB XLF from young stellar populations in star-forming galaxies with high sSFR to the almost "pure" LMXB XLF from old stellar populations in early-type galaxies with low sSFR.

Figure 3.17 shows the differential XLF normalised to the SFR (upper panel) for galaxies with log(sSFR) $>$ -10.5 yr^{-1} and to the $M_\star$ for galaxies with log(sSFR) $<$ -10.5 yr^{-1} (lower panel) in three log(sSFR) bins. The colored lines show the power-law (upper panel) and broken power-law (lower panel) fits for each bin.

In the XLF of star-forming galaxies (upper panel), the power-law slope α of the XLF decreases (becomes flatter) for increasing sSFR (from blue to red), indicating an increased production of luminous X-ray sources in galaxies with high sSFR. The power-law normalization (per SFR) K also decreases with increasing sSFR, due to the decreasing population of LMXBs and the dominance of HMXBs in galaxies with high sSFR.

In the XLF of early-type galaxies (lower panel), the high luminosity broken power-law slope α_h increases (becomes stepper) for decreasing sSFR (from blue to red), indicating a decreasing population of luminous X-ray sources in galaxies with low sSFR. The broken power-law normalization (per $M_\star$) K decreases with decreasing sSFR, indicating a smaller population of XRBs due to the decreasing population of HMXBs and the dominance of LMXBs in galaxies with low sSFR.

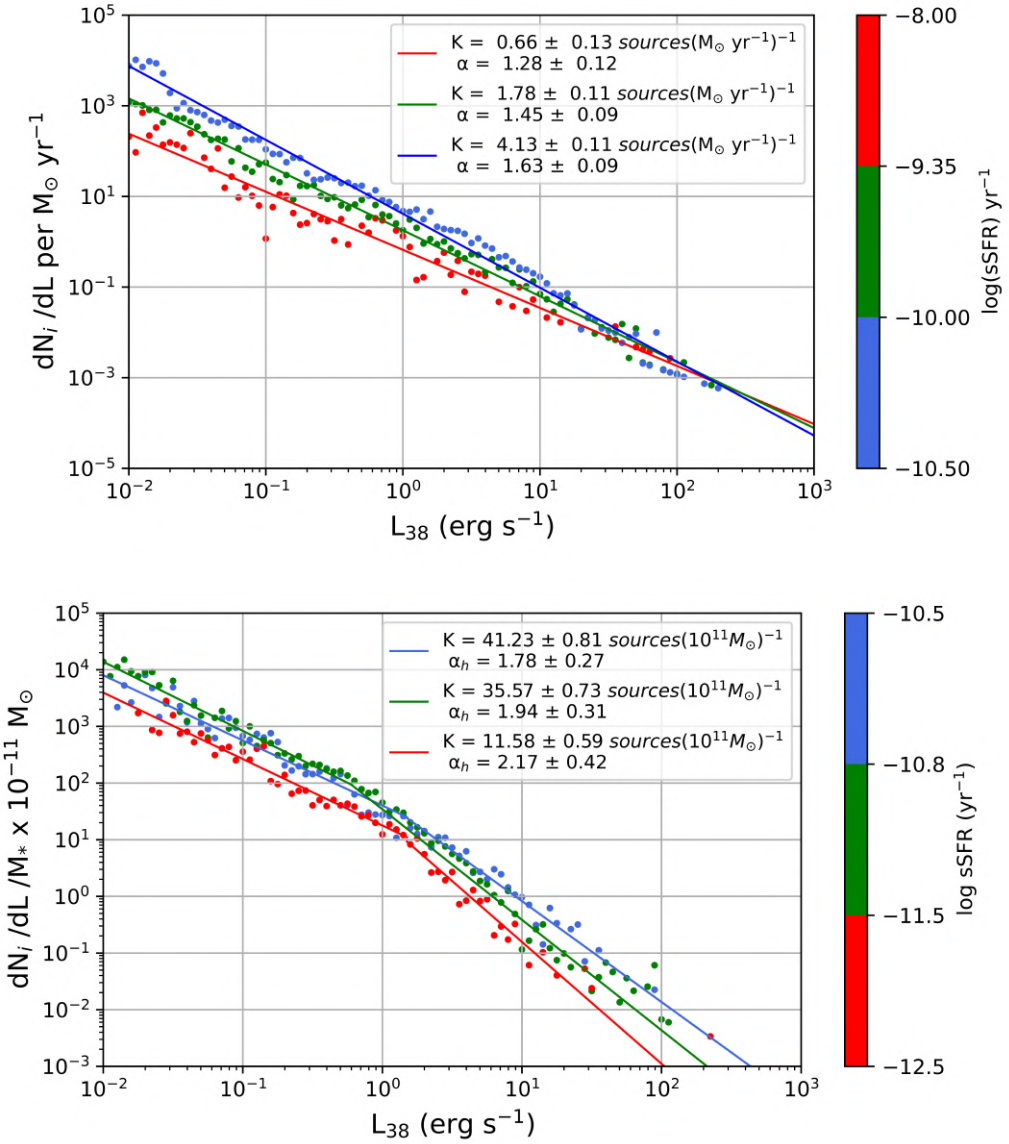

Figure 3.17: Differential XLF in three log(sSFR) bins for star-forming (upper panel) and early-type (lower panel) galaxies. The colored lines show the model fits for each bin. In the upper panel, the power-law slope and normalization (per SFR) decrease with increasing sSFR, due to the decreasing population of LMXBs and the dominance of HMXBs in galaxies with high sSFR. In the lower panel, for decreasing sSFR the high luminosity broken power-law slope α_h increases (becomes stepper) and the normalization (per M_*) decreases due to the decreasing population of HMXBs and the dominance of LMXBs in galaxies with low sSFR.

3.8 XLFs as a function of metallicity

Recent theoretical and observational studies of integrated scaling relations (e.g., Fragos *et al.* (2013b); Linden *et al.* (2010); Politakis *et al.* (2020); Renzo *et al.* (2019); Fornasini *et al.* (2020); Kouroumpatzakis *et al.* (2020), imply that apart from SFR and M^*, another physical property that has an important impact on the scaling relations of star-forming galaxies dominated by HMXBs is the metallicity (Z) of the stellar populations. The metallicity dependence of HMXBs arises from the fact that higher-metallicity stars have more powerful radiatively-driven winds. As a result, higher-metallicity stars in binaries lose more mass and angular momentum prior to exploding as supernovae compared to their lower-metallicity counterparts. Thus, the aforementioned studies predict that lower-metallicity HMXB populations should host more massive compact objects in tighter orbits resulting in more Roche-lobe overflow systems and subsequently in higher accretion rates and higher X-ray luminosities on average.

Figure 3.18 shows the differential (SFR normalised) XLF of X-ray sources in star-forming galaxies (of type spiral c,d,m and irregular) in three metallicity bins selected according to the solar metallicity, measured in [12+log(O/H)]:

- Less than 8.4 (Low metallicity, shown with red dots)
- Between 8.4 and 8.65 (Sub-solar metallicity, shown with green dots)
- Greater than 8.65 (Solar metallicity, shown with blue dots).

The value of solar metallicity is $Z_{\odot} = 0.0134$, corresponding to [12+log(O/H)] = 8.69 ± 0.05 (Asplund *et al.* 2009).

The colored lines in Figure 3.18 show the single power-law fits for each metallicity bin. Low-metallicity galaxies tend to have flatter XLFs (smaller power-law slopes) and higher normalisations (per SFR), indications of increased formation rate of XRBs and

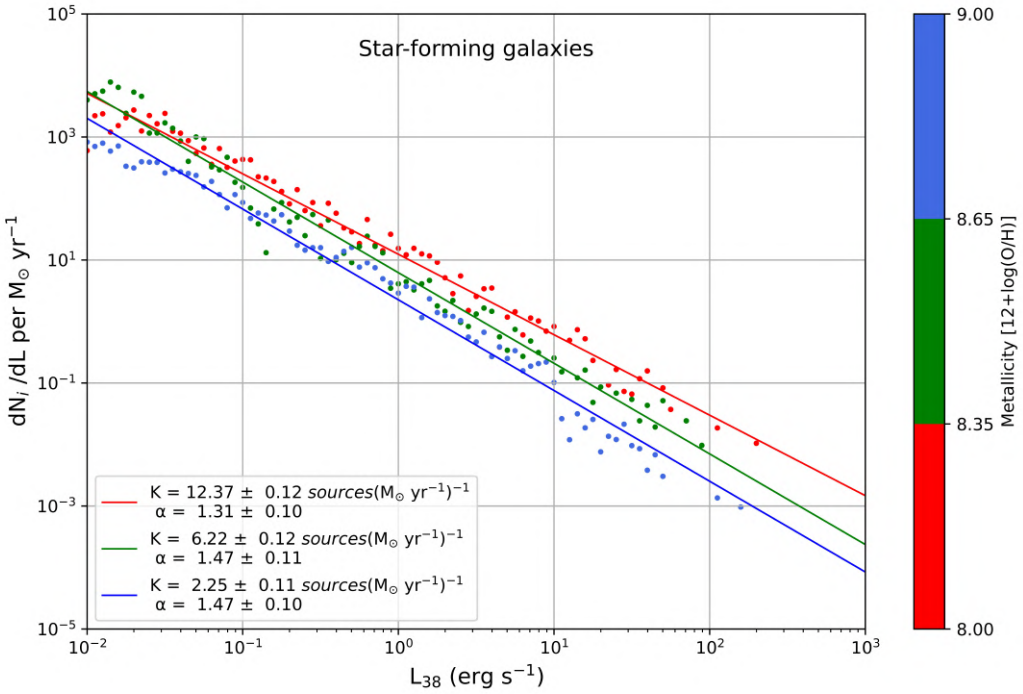

Figure 3.18: Differential XLF of XRBs in three metallicity bins for star-forming galaxies (of spiral c,d,m and irregular morphological types). Metallicity bins are selected according to the solar metallicity (see text for details). The colored lines show the power-law fits for each metallicity bin. The power-law slope α is lower for low metallicity galaxies, while the power-law normalisation (per SFR) K increases with decreasing metallicity, indicating more efficient HMXB production in metal poor environments.

increasing number of XRBs with high luminosities. The HMXB formation efficiency (defined as the number of X-ray sources N_i/SFR) for each bin and for $L > 10^{35}$ erg s^{-1}is:

- Low metallicity, ~ 535 (sources/$M_\odot$ yr^{-1})
- Sub-solar metallicity, ~ 114 (sources/$M_\odot$ yr^{-1})
- Solar metallicity, ~ 63 (sources/$M_\odot$ yr^{-1}).

This is consistent with the aforementioned studies and population synthesis models predicting more efficient HMXB production in metal poor environments as well as the formation efficiency of MW, LMC, SMS, NGC 55 presented in Table 2.5.

This page intentionally left blank

4

Conclusions and future perspectives

4.1 Conclusions

In this thesis we first studied the vertical distribution of HMXBs in the closest to the Milky Way edge-on galaxy NGC 55, in correlation with the distribution of star formation within the galaxy and we presented that:

- The vertical distribution of HMXBs compared to the star-forming activity distribution has a larger scale height. The maximum likelihood vertical scale height corresponding to the difference between HMXBs and star-forming regions is between 0.33 and 0.57 kpc.

- We interpret the vertical offsets in the context of a momentum kick the HMXB progenitor received, after the supernova explosion of the primary star.

- Using HMXB travel times from binary population synthesis models for different star-formation history scenarios, we find that the centre-of-mass transverse velocity

strongly depends on the recent star-formation history of NGC 55.

- For a flat SFH model, the centre-of-mass transverse velocity is between 34 and 48 km s^{-1} consistent with velocities of Milky Way HMXBs.

- For an exponential SFH model, the centre-of-mass transverse velocity is approximately 21 km s^{-1} consistent with the corresponding velocity of HMXBs in the SMC and LMC.

- The formation efficiency of XRBs in NGC 55 is consistent with the formation efficiency of XRBs in SMC and LMC, but significantly larger than that of the Milky Way, a difference that can be attributed to the sub-solar metallicity of both the MCs and NGC 55.

We also studied the demographics of the largest so far population of XRBs in nearby galaxies, comprised of 10,099 X-ray sources in 319 nearby galaxies, to revisit scaling relations of the HMXB and LMXB X-ray Luminosity Functions with SFR and $M_\star$ respectively, and we presented that:

- The differential XLF of XRBs in star-forming galaxies (of spiral c,d,m and irregular type) dominated by HMXBs, when normalised to the SFR of the hosting galaxies is represented by a power-law model with parameters: Normalisation K_{HMXB} = 2.82 ± 0.32 $sources(M_\odot\ \mathrm{yr}^{-1})^{-1}$ and slope α = -1.58 ± 0.26.

- The value of the power-law slope α is consistent with the values in similar studies of Mineo *et al.* (2012a) and Lehmer *et al.* (2019).

- The value of the normalisation K_{HMXB} is in good agreement with the study of Mineo *et al.* (2012a) but is higher than the corresponding values of Lehmer *et al.* (2019). We attributed the difference to our galaxy and X-ray source samples that contain more low metallicity star-forming galaxies with efficient HMXB production.

- The differential XLF of XRBs in early-type galaxies (of elliptical and lenticular type),

when normalised to the $M_\star$ of the hosting galaxies is represented by a broken power-law model with parameters: Normalisation $K_{LMXB} = 38.00 \pm 0.67$ $sources(10^{11} M_\odot)^{-1}$, low-luminosity slope $\alpha_1 = 1.253 \pm 0.004$, high-luminosity slope $\alpha_2 = 2.08 \pm 0.19$ and luminosity break $L_b = 1.33 \pm 0.21$ ($\times 10^{38}$ erg s^{-1}).

- The shape and scaling with the $M_\star$ of the differential XLF of XRBs in early-type galaxies are in agreement with the studies of Zhang *et al.* 2012 and Lehmer *et al.* (2019).

- In spiral a,b galaxies where the population of XRBs consists of both HMXBs and LMXBs the contribution from each type of XRBs is estimated from the corresponding normalisations K_H and K_L with values: $K_H = 0.83 \pm 0.35$ $sources(M_\odot\ \mathrm{yr}^{-1})^{-1}$ and $K_L = 22.42 \pm 3.51$ $sources(10^{11} M_\odot)^{-1}$.

- The estimated values of the integrated LMXB X-ray luminosity per unit stellar mass α_{LMXB} and of the integrated HMXB X-ray luminosity per unit SFR β_{HMXB} are: $\log \alpha_{LMXB} = 29.85 \pm 0.71$ erg s^{-1} $M_\odot{}^{-1}$ and $\log \beta_{HMXB} = 39.37 \pm 0.17$ erg s^{-1} $(M_\odot\ \mathrm{yr}^{-1})^{-1}$. The scatter of the distribution of the integrated X-ray luminosity per unit SFR (L_x/SFR) vs. sSFR of our sample compared with the sample of Lehmer *et al.* (2019) is significantly larger, extending towards higher luminosities. The excessive integrated luminosity is attributed to metal poor galaxies containing X-ray binaries with super-Eddington luminosities (ULXs) greater than 5×10^{39} erg s^{-1}.

- In the XLF of star-forming galaxies, the power-law slope of the XLF decreases (becomes flatter) for increasing sSFR , indicating an increased production of luminous X-ray sources in galaxies with high sSFR. The power-law normalization (per SFR) also decreases with increasing sSFR, due to the decreasing population of LMXBs and the dominance of HMXBs in galaxies with high sSFR.

- In the XLF of early-type galaxies, the high-luminosity broken power-law slope increases (becomes stepper) for decreasing sSFR, indicating a decreasing population of

luminous X-ray sources in galaxies with low sSFR. The broken power-law normalization (per $M_\star$) decreases with decreasing sSFR, indicating a smaller population of XRBs due to the decreasing population of HMXBs and the dominance of LMXBs in galaxies with low sSFR.

- Low-metallicity galaxies tend to have flatter XLFs (smaller power-law slopes) and higher normalisations (per SFR), an indication of increased formation rate of XRBs and increasing number of XRBs with high luminosities. This is consistent with the aforementioned studies and population synthesis models predicting more efficient HMXB production in metal poor environments..

4.2 Future Plans

The methodology for the estimation of the center-of-mass transverse velocity can be used for other nearby edge-on galaxies (e.g. NGC 253, NGC 4594, NGC 3115). It can be complemented with information regarding the identification of optical counterparts (companions) to X-ray sources, enabling the classification of XRBs (HMXBs or LMXBs).

The demographics of XRB populations and their scaling relations with the intrinsic properties of their host galaxies, can be enriched with data from the forthcoming version of *CSC* that contains X-ray observations of galaxies not included in the present sample, as well as additional observations for the galaxies already included in the sample.

Both methodologies will be greatly affected by the advent of 30-m class ground based optical/infrared telescopes as well as the next generation of X-ray space telescopes.Ground based telescopes will provide more accurate measurements of the intrinsic properties of galaxies, as well as spectroscopic measurements for the identification of optical counterparts. The next generation of X-ray telescopes will detect the XRB populations not only in numerous nearby galaxies, but also in galaxies with high z. The *Athena X-ray observatory* will be capable of individually detecting XRB-dominated galaxies out to $z \sim 1$ (Nandra *et al.* 2013) and the *Lynx X-ray Observatory* would push this limit to $z \sim 10$ (Gaskin *et al.* 2019).

This page intentionally left blank

Bibliography

Andrade-Santos, F., Jones, C., Forman, W.R., Lovisari, L., Vikhlinin, A., van Weeren, R.J., Murray, S.S., Arnaud, M., Pratt, G.W., Démoclès, J., Kraft, R., Mazzotta, P., Böhringer, H., Chon, G., Giacintucci, S., Clarke, T.E., Borgani, S., David, L., Douspis, M., Pointecouteau, E., Dahle, H., Brown, S., Aghanim, N. & Rasia, E. (2017). The Fraction of Cool-core Clusters in X-Ray versus SZ Samples Using Chandra Observations. ApJ, **843**, 76. (in p. 60)

Andrews, J.J., Zezas, A. & Fragos, T. (2018). dart_board: Binary Population Synthesis with Markov Chain Monte Carlo. *The Astrophysical Journal Supplement Series*, **237**, 1. (in pp. 28 and 56)

Antoniou, V. & Zezas, A. (2016). Star formation history and X-ray binary populations: the case of the Large Magellanic Cloud. MNRAS, **459**, 528–553. (in pp. 44, 63, 64, and 66)

Antoniou, V., Zezas, A., Drake, J.J., Badenes, C., Haberl, F., Wright, N.J., Hong, J., Di Stefano, R., Gaetz, T.J., Long, K.S., Plucinsky, P.P., Sasaki, M., Williams, B.F. & Winkler, P.F. (2019). Deep Chandra survey of the Small Magellanic Cloud. III. Formation efficiency of High-Mass X-ray binaries. *arXiv e-prints*, arXiv:1901.01237. (in p. 63)

Asplund, M., Grevesse, N., Sauval, A.J. & Scott, P. (2009). The chemical composition of the sun. *Annual Review of Astronomy and Astrophysics*, **47**, 481–522. (in p. 116)

Bakis, V., Bulut, , Bilir, S., Bakis, H., Demircan, O. & Hensberge, H. (2010). Absolute Dimensions and Apsidal Motion of the Young Detached System LT Canis Majoris. *Publications of the Astronomical Society of Japan*, **62**, 1291–1299. (in p. 18)

Baron, F., Monnier, J.D., Pedretti, E., Zhao, M., Schaefer, G., Parks, R., Che, X., Thureau, N., ten Brummelaar, T.A., McAlister, H.A., Ridgway, S.T., Farrington, C., Sturmann, J., Sturmann, L. & Turner, N. (2012). Imaging the Algol Triple System in the H Band with the CHARA Interferometer. ApJ, **752**, 20. (in p. 18)

Belczynski, K., Kalogera, V., Zezas, A. & Fabbiano, G. (2004). X-Ray Binary Populations: The Luminosity Function of NGC 1569. ApJ, **601**, L147–L150. (in p. 27)

Belczynski, K., Kalogera, V., Rasio, F.A., Taam, R.E., Zezas, A., Bulik, T., Maccarone, T.J. & Ivanova, N. (2008). Compact Object Modeling with the StarTrack Population Synthesis Code. ApJS, **174**, 223–260. (in p. 27)

Belczynski, K., Kalogera, V., Rasio, F.A., Taam, R.E., Zezas, A., Bulik, T., Maccarone, T.J. & Ivanova, N. (2008). Compact object modeling with the startrack population synthesis code. *The Astrophysical Journal Supplement Series*, **174**, 223. (in p. 27)

Bell, E.F. (2003). Estimating Star Formation Rates from Infrared and Radio Luminosities: The Origin of the Radio-Infrared Correlation. ApJ, **586**, 794–813. (in p. 109)

Bell, E.F. & Kennicutt, J., Robert C. (2001). A Comparison of Ultraviolet Imaging Telescope Far-Ultraviolet and Hα Star Formation Rates. ApJ, **548**, 681–693. (in p. 110)

Bibliography

Bell, E.F., McIntosh, D.H., Katz, N. & Weinberg, M.D. (2003). The Optical and Near-Infrared Properties of Galaxies. I. Luminosity and Stellar Mass Functions. ApJS, **149**, 289–312. (in p. 81)

Bildsten, L., Chakrabarty, D., Chiu, J., Finger, M.H., Koh, D.T., Nelson, R.W., Prince, T.A., Rubin, B.C., Scott, D.M., Stollberg, M., Vaughan, B.A., Wilson, C.A. & Wilson, R.B. (1997). Observations of Accreting Pulsars. ApJS, **113**, 367–408. (in p. 10)

Binder, B., Williams, B.F., Eracleous, M., Plucinsky, P.P., Gaetz, T.J., Anderson, S.F., Skillman, E.D., Dalcanton, J.J., Kong, A.K.H. & Weisz, D.R. (2015). The Chandra Local Volume Survey. I. The X-Ray Point Source Populations of NGC 55, NGC 2403, and NGC 4214. AJ, **150**, 94. (in pp. 32, 33, 34, 35, 37, 38, 39, 40, 41, 42, 43, and 66)

Blaauw, A. (1961). On the origin of the O- and B-type stars with high velocities (the "run-away" stars), and some related problems. Bull. Astron. Inst. Netherlands, **15**, 265. (in p. 20)

Bodaghee, A., Courvoisier, T.J.L., Rodriguez, J., Beckmann, V., Produit, N., Hannikainen, D., Kuulkers, E., Willis, D.R. & Wendt, G. (2007). A description of sources detected by INTEGRAL during the first 4 years of observations. A&A, **467**, 585–596. (in p. 60)

Bodaghee, A., Tomsick, J.A., Rodriguez, J. & James, J.B. (2012). Clustering between High-mass X-Ray Binaries and OB Associations in the Milky Way. ApJ, **744**, 108. (in pp. 44, 61, 63, 64, and 66)

Bondi, H. & Hoyle, F. (1944). On the Mechanism of Accretion by Stars. *Monthly Notices of the Royal Astronomical Society*, **104**, 273–282. (in p. 4)

Boroson, B., Kim, D.W. & Fabbiano, G. (2011). Revisiting with Chandra the Scaling Relations of the X-ray Emission Components (Binaries, Nuclei, and Hot Gas) of Early-type Galaxies. ApJ, **729**, 12. (in p. 25)

Brandt, N. & Podsiadlowski, P. (1995). The effects of high-velocity supernova kicks on the orbital properties and sky distributions of neutron-star binaries. MNRAS, **274**, 461–484. (in pp. 20, 64, and 65)

Brinchmann, J., Charlot, S., White, S.D.M., Tremonti, C., Kauffmann, G., Heckman, T. & Brinkmann, J. (2004). The physical properties of star-forming galaxies in the low-redshift Universe. MNRAS, **351**, 1151–1179. (in p. 81)

Brorby, M., Kaaret, P. & Prestwich, A. (2014). X-ray binary formation in low-metallicity blue compact dwarf galaxies. *Monthly Notices of the Royal Astronomical Society*, **441**, 2346–2353. (in p. 29)

Budding, E., Butland, R. & Blackford, M. (2015). Absolute parameters of young stars: GG Lup and μ1 Sco. *Monthly Notices of the Royal Astronomical Society*, **448**, 3784–3796. (in p. 18)

Calzetti, D. (2008). Star Formation Rates in the Infrared. In R.R. Chary, H.I. Teplitz & K. Sheth, eds., *Infrared Diagnostics of Galaxy Evolution*, vol. 381 of *Astronomical Society of the Pacific Conference Series*, 323. (in p. 44)

Casares, J., Negueruela, I., Ribó, M., Ribas, I., Paredes, J.M., Herrero, A. & Simón-Díaz, S. (2014). A Be-type star with a black-hole companion. Nature, **505**, 378–381. (in p. 6)

Castro, N., Herrero, A., Garcia, M., Trundle, C., Bresolin, F., Gieren, W., Pietrzyński, G., Kudritzki, R.P. & Demarco, R. (2008). The Araucaria Project: VLT-spectroscopy of blue massive stars in NGC 55. A&A, **485**, 41–50. (in pp. 38, 39, and 41)

Cluver, M.E., Jarrett, T.H., Dale, D.A., Smith, J.D.T., August, T. & Brown, M.J.I. (2017). Calibrating Star Formation in WISE Using Total Infrared Luminosity. ApJ, **850**, 68. (in p. 81)

Coe, M.J. (2005). An estimate of the supernova kick velocities for high-mass X-ray binaries in the Small Magellanic Cloud. MNRAS, **358**, 1379–1382. (in pp. 44, 64, and 66)

Dalcanton, J.J., Williams, B.F., Seth, A.C., Dolphin, A., Holtzman, J., Rosema, K., Skillman, E.D., Cole, A., Girardi, L., Gogarten, S.M., Karachentsev, I.D., Olsen, K., Weisz, D., Christensen, C., Freeman, K., Gilbert, K., Gallart, C., Harris, J., Hodge, P., de Jong, R.S., Karachentseva, V., Mateo, M., Stetson, P.B., Tavarez, M., Zaritsky, D., Governato, F. & Quinn, T. (2009). The ACS Nearby Galaxy Survey Treasury. ApJS, **183**, 67–108. (in p. 32)

Dale, D.A. & Helou, G. (2002). The Infrared Spectral Energy Distribution of Normal Star-forming Galaxies: Calibration at Far-Infrared and Submillimeter Wavelengths. ApJ, **576**, 159–168. (in p. 81)

Dale, D.A., Cohen, S.A., Johnson, L.C., Schuster, M.D., Calzetti, D., Engelbracht, C.W., Gil de Paz, A., Kennicutt, R.C., Lee, J.C., Begum, A., Block, M., Dalcanton, J.J., Funes, J.G., Gordon, K.D., Johnson, B.D., Marble, A.R., Sakai, S., Skillman, E.D., van Zee, L., Walter, F., Weisz, D.R., Williams, B., Wu, S.Y. & Wu, Y. (2009). The Spitzer Local Volume Legacy: Survey Description and Infrared Photometry. ApJ, **703**, 517–556. (in pp. 33, 44, 47, and 48)

Davidge, T.J. (2005). The Disk and Extraplanar Regions of NGC 55. ApJ, **622**, 279–293. (in pp. 33, 53, and 55)

de Vaucouleurs, G., de Vaucouleurs, A., Corwin, H.G., Jr., Buta, R.J., Paturel, G. & Fouqué, P. (1991). *Third Reference Catalogue of Bright Galaxies. Volume I: Explanations and references. Volume II: Data for galaxies between 0^h and 12^h. Volume III: Data for galaxies between 12^h and 24^h.*. (in pp. 32, 33, and 46)

Dean, A.J., Bazzano, A., Hill, A.B., Stephen, J.B., Bassani, L., Barlow, E.J., Bird, A.J., Lebrun, F., Sguera, V., Shaw, S.E., Ubertini, P., Walter, R. & Willis, D.R. (2005). Global characteristics of the first IBIS/ISGRI catalogue sources: unveiling a murky episode of binary star evolution. A&A, **443**, 485–494. (in p. 60)

Douna, V.M., Pellizza, L.J., Mirabel, I.F. & Pedrosa, S.E. (2015). Metallicity dependence of high-mass X-ray binary populations. A&A, **579**, A44. (in p. 29)

Eggleton, P.P. (1983). Aproximations to the radii of Roche lobes. ApJ, **268**, 368–369. (in p. 3)

Ekström, S., Georgy, C., Eggenberger, P., Meynet, G., Mowlavi, N., Wyttenbach, A., Granada, A., Decressin, T., Hirschi, R., Frischknecht, U., Charbonnel, C. & Maeder, A. (2012). Grids of stellar models with rotation. I. Models from 0.8 to 120 $M_{amp;sun;}$ at solar metallicity (Z = 0.014). A&A, **537**, A146. (in pp. 40 and 43)

Engelbracht, C.W., Gordon, K.D., Bendo, G.J., Pérez-González, P.G., Misselt, K.A., Rieke, G.H., Young, E.T., Hines, D.C., Kelly, D.M., Stansberry, J.A., Papovich, C., Morrison, J.E., Egami, E., Su, K.Y.L., Muzerolle, J., Dole, H., Alonso-Herrero, A., Hinz, J.L., Smith, P.S., Latter, W.B., Noriega-Crespo, A., Padgett, D.L., Rho, J., Frayer, D.T. & Wachter, S. (2004). Far-Infrared Imaging of NGC 55. ApJS, **154**, 248–252. (in p. 33)

Erdem, A., Sürgit, D., Banks, T.S., Özkardeş, B. & Budding, E. (2021). Absolute parameters of young stars: PU Pup. *Research in Astronomy and Astrophysics*, **21**, 256. (in p. 18)

Erdem, A. & Öztürk, O. (2014). Non-conservative mass transfers in Algols. *Monthly Notices of the Royal Astronomical Society*, **441**, 1166–1176. (in p. 18)

Evans, I.N., Primini, F.A., Miller, J.B., Evans, J.D., Allen, C.E., Anderson, C.S., Becker, G., Budynkiewicz, J.A., Burke, D., Chen, J.C., Civano, F., D'Abrusco, R., Doe, S.M., Fabbiano, G., Martinez Galarza, J., Gibbs, I., D. G., Glotfelty, K.J., Graessle, D.E., Grier, J., J. D., Hain, R.M., Hall, D.M., Harbo, P.N., Houck, J.C., Lauer, J.L., Laurino, O., Lee, N.P., McCollough, M.L., McDowell, J.C., McLaughlin, W., Morgan, D.L., Mossman, A.E., Nguyen, D.T., Nichols, J.S., Nowak, M.A., Paxson, C., Perdikeas, M., Plummer, D.A., Rots, A.H., Siemiginowska, A.L., Sundheim, B.A., Thong, S., Tibbetts, M.S., Van Stone, D.W., Winkelman, S.L. & Zografou, P. (2020). The Chandra Source Catalog — A Billion X-ray Photons. In *American Astronomical Society Meeting Abstracts #235*, vol. 235 of *American Astronomical Society Meeting Abstracts*, 154.05. (in pp. 30, 68, 70, and 72)

Fabbiano, G. (1989). X rays from normal galaxies. *Annual Review of Astronomy and Astrophysics*, **27**, 87–138. (in p. 25)

Fabbiano, G. (2006). Populations of X-Ray Sources in Galaxies. ARA&A, **44**, 323–366. (in pp. 5 and 31)

Fornasini, F.M., Civano, F. & Suh, H. (2020). Connecting the metallicity dependence and redshift evolution of high-mass X-ray binaries. MNRAS, **495**, 771–783. (in p. 116)

Fragos, T., Kalogera, V., Willems, B., Belczynski, K., Fabbiano, G., Brassington, N.J., Kim, D.W., Angelini, L., Davies, R.L., Gallagher, J.S., King, A.R., Pellegrini, S., Trinchieri, G., Zepf, S.E. & Zezas, A. (2009). Transient Low-mass X-ray Binary Populations in Elliptical Galaxies NGC 3379 and NGC 4278. ApJ, **702**, L143–L147. (in p. 27)

Fragos, T., Lehmer, B., Tremmel, M., Tzanavaris, P., Basu-Zych, A., Belczynski, K., Hornschemeier, A., Jenkins, L., Kalogera, V., Ptak, A. & Zezas, A. (2013a). X-Ray Binary Evolution Across Cosmic Time. ApJ, **764**, 41. (in pp. 28, 29, and 63)

Fragos, T., Lehmer, B.D., Naoz, S., Zezas, A. & Basu-Zych, A. (2013b). Energy Feedback from X-Ray Binaries in the Early Universe. ApJ, **776**, L31. (in pp. 25 and 116)

Frank, J., King, A. & Raine, D.J. (2002). *Accretion Power in Astrophysics: Third Edition*. (in pp. 4 and 22)

Fryer, C. & Kalogera, V. (1997). Double Neutron Star Systems and Natal Neutron Star Kicks. ApJ, **489**, 244–253. (in pp. 31 and 49)

Gaia Collaboration (2018). VizieR Online Data Catalog: Gaia DR2 (Gaia Collaboration, 2018). *VizieR Online Data Catalog*, **1345**. (in p. 60)

Gaskin, J., Özel, F., Vikhlinin, A. & Swartz, D. (2019). Special Section Guest Editorial: Lynx X-Ray Observatory. *Journal of Astronomical Telescopes, Instruments, and Systems*, **5**, 021000. (in p. 123)

Ghosh, H., Mathur, S., Fiore, F. & Ferrarese, L. (2008). Low-Level Nuclear Activity in Nearby Spiral Galaxies. ApJ, **687**, 216–229. (in p. 74)

Gieren, W., Pietrzyński, G., Soszyński, I., Bresolin, F., Kudritzki, R.P., Storm, J. & Minniti, D. (2008). The Araucaria Project: Near-Infrared Photometry of Cepheid Variables in the Sculptor Galaxy NGC 55. ApJ, **672**, 266–273. (in pp. 31 and 33)

Gil de Paz, A., Boissier, S., Madore, B.F., Seibert, M., Joe, Y.H., Boselli, A., Wyder, T.K., Thilker, D., Bianchi, L., Rey, S.C., Rich, R.M., Barlow, T.A., Conrow, T., Forster, K., Friedman, P.G., Martin, D.C., Morrissey, P.,

Neff, S.G., Schiminovich, D., Small, T., Donas, J., Heckman, T.M., Lee, Y.W., Milliard, B., Szalay, A.S. & Yi, S. (2007). The GALEX Ultraviolet Atlas of Nearby Galaxies. ApJS, **173**, 185–255. (in pp. 32, 34, 47, and 48)

Gilfanov, M., Grimm, H.J. & Sunyaev, R. (2004). Statistical properties of the combined emission of a population of discrete sources: astrophysical implications. MNRAS, **351**, 1365–1378. (in pp. 25, 26, and 67)

Grimm, H.J., Gilfanov, M. & Sunyaev, R. (2002). The Milky Way in X-rays for an outside observer. Log(N)-Log(S) and luminosity function of X-ray binaries from RXTE/ASM data. A&A, **391**, 923–944. (in pp. 5 and 60)

Grimm, H.J., Gilfanov, M. & Sunyaev, R. (2003). High-mass X-ray binaries as a star formation rate indicator in distant galaxies. MNRAS, **339**, 793–809. (in pp. 5, 25, 26, 31, 40, and 67)

Hao, C.N., Kennicutt, R.C., Johnson, B.D., Calzetti, D., Dale, D.A. & Moustakas, J. (2011). Dust-corrected Star Formation Rates of Galaxies. II. Combinations of Ultraviolet and Infrared Tracers. ApJ, **741**, 124. (in p. 109)

Harris, J. & Zaritsky, D. (2009). The Star Formation History of the Large Magellanic Cloud. AJ, **138**, 1243–1260. (in pp. 63 and 66)

Hastings, W.K. (1970). Monte Carlo Sampling Methods using Markov Chains and their Applications. *Biometrika*, **57**, 97–109. (in p. 90)

Helou, G. & Walker, D.W. (1988). Infrared Astronomical Satellite (IRAS), Catalogs and Atlases. Vol. 7. The Small Scale Structure Catalog. *NASA RP-1190*, **7**, 0. (in p. 81)

Ho, L.C. & Ulvestad, J.S. (2001). Radio Continuum Survey of an Optically Selected Sample of Nearby Seyfert Galaxies. ApJS, **133**, 77–118. (in p. 74)

Hurley, J.R., Tout, C.A. & Pols, O.R. (2002). Evolution of binary stars and the effect of tides on binary populations. *Monthly Notices of the Royal Astronomical Society*, **329**, 897–928. (in p. 56)

Jarrett, T.H. (2000). Near-Infrared Galaxy Morphology Atlas. PASP, **112**, 1008–1080. (in p. 33)

Kaaret, P., Alonso-Herrero, A., Gallagher, J.S., Fabbiano, G., Zezas, A. & Rieke, M.J. (2004). Displacement of X-ray sources from star clusters in starburst galaxies. MNRAS, **348**, L28–L32. (in p. 31)

Kaaret, P., Feng, H. & Roberts, T.P. (2017). Ultraluminous X-Ray Sources. ARA&A, **55**, 303–341. (in pp. 23 and 29)

Kalogera, V. (1996). Orbital Characteristics of Binary Systems after Asymmetric Supernova Explosions. ApJ, **471**, 352. (in pp. 20 and 65)

Karim, M.T. & Mamajek, E.E. (2017). Revised geometric estimates of the North Galactic Pole and the Sun's height above the Galactic mid-plane. MNRAS, **465**, 472–481. (in p. 60)

Karino, S. (2016). The nature of the X-ray pulsar in M 31: An intermediate-mass X-ray binary? PASJ, **68**, 93. (in p. 10)

Kauffmann, G., Heckman, T.M., Tremonti, C., Brinchmann, J., Charlot, S., White, S.D.M., Ridgway, S.E., Brinkmann, J., Fukugita, M., Hall, P.B., Ivezić, Ž., Richards, G.T. & Schneider, D.P. (2003). The host galaxies of active galactic nuclei. MNRAS, **346**, 1055–1077. (in p. 81)

Kennicutt, J., Robert C. (1998). Star Formation in Galaxies Along the Hubble Sequence. ARA&A, **36**, 189–232. (in p. 81)

Kennicutt, R.C. & Evans, N.J. (2012). Star Formation in the Milky Way and Nearby Galaxies. ARA&A, **50**, 531–608. (in p. 81)

Khan, R., Stanek, K.Z., Kochanek, C.S. & Sonneborn, G. (2015). Spitzer Point-source Catalogs of ˜ 300,000 Stars in Seven Nearby Galaxies. ApJS, **219**, 42. (in pp. 38 and 39)

Kim, D.W. & Fabbiano, G. (2010). X-ray properties of young early-type galaxies. i. x-ray luminosity function of low-mass x-ray binaries. *The Astrophysical Journal*, **721**, 1523. (in pp. 26 and 67)

Kim, M., Kim, D.W., Wilkes, B.J., Green, P.J., Kim, E., Anderson, C.S., Barkhouse, W.A., Evans, N.R., Ivezić, Ž., Karovska, M., Kashyap, V.L., Lee, M.G., Maksym, P., Mossman, A.E., Silverman, J.D. & Tananbaum, H.D. (2007). Chandra Multiwavelength Project X-Ray Point Source Catalog. ApJS, **169**, 401–429. (in pp. 33, 71, and 76)

King, A.R. (2002). The brightest black holes. *Monthly Notices of the Royal Astronomical Society*, **335**, L13–L16. (in p. 24)

King, A.R., Davies, M.B., Ward, M.J., Fabbiano, G. & Elvis, M. (2001). Ultraluminous X-Ray Sources in External Galaxies. ApJ, **552**, L109–L112. (in p. 24)

Kolbas, V., Pavlovski, K., Southworth, J., Lee, C.U., Lee, D.J., Lee, J.W., Kim, S.L., Kim, H.I., Smalley, B. & Tkachenko, A. (2015). Spectroscopically resolving the Algol triple system. *Monthly Notices of the Royal Astronomical Society*, **451**, 4150–4161. (in p. 18)

Kong, D.L. & Zhu, Z. (2008). A Study of the Scale Height of the Thin Galactic Disk in the Solar Neighborhood. Chinese Astron. Astrophys., **32**, 360–368. (in pp. 60 and 62)

Kouroumpatzakis, K., Zezas, A., Sell, P., Kovlakas, K., Bonfini, P., Willner, S.P., Ashby, M.L.N., Maragkoudakis, A. & Jarrett, T.H. (2020). Sub-galactic scaling relations between X-ray luminosity, star formation rate, and stellar mass. MNRAS, **494**, 5967–5984. (in p. 116)

Kovlakas, K., Zezas, A., Andrews, J.J., Basu-Zych, A., Fragos, T., Hornschemeier, A., Kouroumpatzakis, K., Lehmer, B. & Ptak, A. (2021). The Heraklion Extragalactic Catalogue (HECATE): a value-added galaxy catalogue for multimessenger astrophysics. *Monthly Notices of the Royal Astronomical Society*, **506**, 1896–1915. (in pp. 30, 69, and 81)

Kudritzki, R.P., Castro, N., Urbaneja, M.A., Ho, I.T., Bresolin, F., Gieren, W., Pietrzyński, G. & Przybilla, N. (2016). A Spectroscopic Study of Blue Supergiant Stars in the Sculptor Galaxy NGC 55: Chemical Evolution and Distance. ApJ, **829**, 70. (in pp. 33, 55, 61, and 66)

Lang, D., Hogg, D.W. & Schlegel, D.J. (2016). Wise photometry for 400 million sdss sources. *The Astronomical Journal*, **151**, 36. (in p. 81)

Lattimer, J.M. (2012). The Nuclear Equation of State and Neutron Star Masses. *Annual Review of Nuclear and Particle Science*, **62**, 485–515. (in p. 4)

Lehmer, B.D., Alexander, D.M., Bauer, F.E., Brandt, W.N., Goulding, A.D., Jenkins, L.P., Ptak, A. & Roberts, T.P. (2010). A Chandra Perspective on Galaxy-wide X-ray Binary Emission and its Correlation with Star Formation Rate and Stellar Mass: New Results from Luminous Infrared Galaxies. ApJ, **724**, 559–571. (in p. 25)

Lehmer, B.D., Basu-Zych, A.R., Mineo, S., Brandt, W.N., Eufrasio, R.T., Fragos, T., Hornschemeier, A.E., Luo, B., Xue, Y.Q., Bauer, F.E., Gilfanov, M., Ranalli, P., Schneider, D.P., Shemmer, O., Tozzi, P., Trump, J.R., Vignali, C., Wang, J.X., Yukita, M. & Zezas, A. (2016). The Evolution of Normal Galaxy X-Ray Emission through Cosmic History: Constraints from the 6 MS Chandra Deep Field-South. ApJ, **825**, 7. (in p. 25)

Lehmer, B.D., Eufrasio, R.T., Markwardt, L., Zezas, A., Basu-Zych, A., Fragos, T., Hornschemeier, A.E., Ptak, A., Tzanavaris, P. & Yukita, M. (2017). On the Spatially Resolved Star Formation History in M51. II. X-Ray Binary Population Evolution. ApJ, **851**, 11. (in p. 28)

Lehmer, B.D., Eufrasio, R.T., Tzanavaris, P., Basu-Zych, A., Fragos, T., Prestwich, A., Yukita, M., Zezas, A., Hornschemeier, A.E. & Ptak, A. (2019). X-Ray Binary Luminosity Function Scaling Relations for Local Galaxies Based on Subgalactic Modeling. ApJS, **243**, 3. (in pp. 26, 27, 29, 67, 81, 82, 84, 105, 107, 108, 109, 120, and 121)

Licquia, T. & Newman, J. (2014). Improved Constraints on the Milky Way - Star Formation Rate and Stellar Mass from Hierarchical Bayesian Analysis. In *American Astronomical Society Meeting Abstracts #223*, vol. 223 of *American Astronomical Society Meeting Abstracts*, 336.04. (in pp. 61, 63, and 66)

Linden, T., Sepinsky, J.F., Kalogera, V. & Belczynski, K. (2009). Probing Electron-Capture Supernovae: X-Ray Binaries in Starbursts. ApJ, **699**, 1573–1577. (in pp. 21 and 65)

Linden, T., Kalogera, V., Sepinsky, J.F., Prestwich, A., Zezas, A. & Gallagher, J.S. (2010). The Effect of Starburst Metallicity on Bright X-ray Binary Formation Pathways. ApJ, **725**, 1984–1994. (in pp. 63 and 116)

Liu, Q.Z., van Paradijs, J. & van den Heuvel, E.P.J. (2006). Catalogue of high-mass X-ray binaries in the Galaxy (4th edition). A&A, **455**, 1165–1168. (in pp. 5, 6, 9, and 60)

Lutovinov, A.A., Revnivtsev, M.G., Tsygankov, S.S. & Krivonos, R.A. (2013). Population of persistent high-mass X-ray binaries in the Milky Way. MNRAS, **431**, 327–341. (in p. 60)

Malkov, O.Y. (2020). Semidetached double-lined eclipsing binaries: Stellar parameters and rare classes. MNRAS, **491**, 5489–5497. (in p. 18)

Maraschi, L., Treves, A. & van den Heuvel, E.P.J. (1976). B-emission Stars and X-ray sources. Nature, **259**, 292. (in p. 6)

Mennickent, R.E., Unda-Sanzana, E. & Tappert, C. (2006). Doppler tomography of the dwarf novae VY Aquari and WX Ceti. A&A, **451**, 613–619. (in p. 18)

Miller, S.T. & Veilleux, S. (2003). Extraplanar Emission-Line Gas in Edge-on Spiral Galaxies. II. Optical Spectroscopy. ApJ, **592**, 79–110. (in p. 33)

Mineo, S., Gilfanov, M. & Sunyaev, R. (2012a). X-ray emission from star-forming galaxies - I. High-mass X-ray binaries. MNRAS, **419**, 2095–2115. (in pp. 25, 26, 27, 67, and 120)

Mineo, S., Gilfanov, M. & Sunyaev, R. (2012b). X-ray emission from star-forming galaxies - II. Hot interstellarmedium. MNRAS, **426**, 1870–1883. (in pp. 25 and 109)

Mineo, S., Gilfanov, M., Lehmer, B.D., Morrison, G.E. & Sunyaev, R. (2014). X-ray emission from star-forming galaxies - III. Calibration of the L_X-SFR relation up to redshift z $\approx$ 1.3. MNRAS, **437**, 1698–1707. (in pp. 25 and 26)

Nakano, S., Nishiyama, K., Kabashima, F., Sakurai, Y., Jacques, C., Pimentel, E., Chekhovich, D., Korotkiy, S., Kryachko, T. & Samus, N.N. (2008). V1309 Scorpii = Nova Scorpii 2008. IAU Circ., **8972**, 1. (in p. 19)

Nandra, K., Barret, D., Barcons, X., Fabian, A., den Herder, J.W., Piro, L., Watson, M., Adami, C., Aird, J., Afonso, J.M., Alexander, D., Argiroffi, C., Amati, L., Arnaud, M., Atteia, J.L., Audard, M., Badenes, C., Ballet, J., Ballo, L., Bamba, A., Bhardwaj, A., Stefano Battistelli, E., Becker, W., De Becker, M., Behar, E., Bianchi, S., Biffi, V., Bîrzan, L., Bocchino, F., Bogdanov, S., Boirin, L., Boller, T., Borgani, S., Borm, K., Bouché, N.,

Bourdin, H., Bower, R., Braito, V., Branchini, E., Branduardi-Raymont, G., Bregman, J., Brenneman, L., Brightman, M., Brüggen, M., Buchner, J., Bulbul, E., Brusa, M., Bursa, M., Caccianiga, A., Cackett, E., Campana, S., Cappelluti, N., Cappi, M., Carrera, F., Ceballos, M., Christensen, F., Chu, Y.H., Churazov, E., Clerc, N., Corbel, S., Corral, A., Comastri, A., Costantini, E., Croston, J., Dadina, M., D'Ai, A., Decourchelle, A., Della Ceca, R., Dennerl, K., Dolag, K., Done, C., Dovciak, M., Drake, J., Eckert, D., Edge, A., Ettori, S., Ezoe, Y., Feigelson, E., Fender, R., Feruglio, C., Finoguenov, A., Fiore, F., Galeazzi, M., Gallagher, S., Gandhi, P., Gaspari, M., Gastaldello, F., Georgakakis, A., Georgantopoulos, I., Gilfanov, M., Gitti, M., Gladstone, R., Goosmann, R., Gosset, E., Grosso, N., Guedel, M., Guerrero, M., Haberl, F., Hardcastle, M., Heinz, S., Alonso Herrero, A., Hervé, A., Holmstrom, M., Iwasawa, K., Jonker, P., Kaastra, J., Kara, E., Karas, V., Kastner, J., King, A., Kosenko, D., Koutroumpa, D., Kraft, R., Kreykenbohm, I., Lallement, R., Lanzuisi, G., Lee, J., Lemoine-Goumard, M., Lobban, A., Lodato, G., Lovisari, L., Lotti, S., McCharthy, I., McNamara, B., Maggio, A., Maiolino, R., De Marco, B., de Martino, D., Mateos, S., Matt, G., Maughan, B., Mazzotta, P., Mendez, M., Merloni, A., Micela, G., Miceli, M., Mignani, R., Miller, J., Miniutti, G., Molendi, S., Montez, R., Moretti, A., Motch, C., Nazé, Y., Nevalainen, J., Nicastro, F., Nulsen, P., Ohashi, T., O'Brien, P., Osborne, J., Oskinova, L., Pacaud, F., Paerels, F., Page, M., Papadakis, I., Pareschi, G., Petre, R., Petrucci, P.O., Piconcelli, E., Pillitteri, I., Pinto, C., de Plaa, J., Pointecouteau, E., Ponman, T., Ponti, G., Porquet, D., Pounds, K., Pratt, G., Predehl, P., Proga, D., Psaltis, D., Rafferty, D., Ramos-Ceja, M., Ranalli, P., Rasia, E., Rau, A., Rauw, G., Rea, N., Read, A., Reeves, J., Reiprich, T., Renaud, M., Reynolds, C., Risaliti, G., Rodriguez, J., Rodriguez Hidalgo, P., Roncarelli, M., Rosario, D., Rossetti, M., Rozanska, A., Rovilos, E., Salvaterra, R., Salvato, M., Di Salvo, T., Sanders, J., Sanz-Forcada, J., Schawinski, K., Schaye, J., Schwope, A., Sciortino, S., Severgnini, P., Shankar, F., Sijacki, D., Sim, S., Schmid, C., Smith, R., Steiner, A., Stelzer, B., Stewart, G., Strohmayer, T., Strüder, L., Sun, M., Takei, Y., Tatischeff, V., Tiengo, A., Tombesi, F., Trinchieri, G., Tsuru, T.G., Ud-Doula, A., Ursino, E., Valencic, L., Vanzella, E., Vaughan, S., Vignali, C., Vink, J., Vito, F., Volonteri, M., Wang, D., Webb, N., Willingale, R., Wilms, J., Wise, M., Worrall, D., Young, A., Zampieri, L., In't Zand, J., Zane, S., Zezas, A., Zhang, Y. & Zhuravleva, I. (2013). The Hot and Energetic Universe: A White Paper presenting the science theme motivating the Athena+ mission. *arXiv e-prints*, arXiv:1306.2307. (in p. 123)

Okazaki, A.T., Hayasaki, K. & Moritani, Y. (2013). Origin of Two Types of X-Ray Outbursts in Be/X-Ray Binaries. I. Accretion Scenarios. PASJ, **65**, 41. (in p. 6)

Olejak, A., Belczynski, K., Bulik, T. & Sobolewska, M. (2020). Synthetic catalog of black holes in the Milky Way. A&A, **638**, A94. (in p. 27)

Orosz, J.A., Kuulkers, E., van der Klis, M., McClintock, J.E., Garcia, M.R., Callanan, P.J., Bailyn, C.D., Jain, R.K. & Remillard, R.A. (2001). A black hole in the superluminal source sax j1819.3â2525 (v4641 sgr). *The Astrophysical Journal*, **555**, 489. (in p. 10)

Peacock, M.B. & Zepf, S.E. (2016). The x-ray luminosity function of low mass x-ray binaries in early-type galaxies, their metal-rich, and metal-poor globular clusters. *The Astrophysical Journal*, **818**, 33. (in pp. 26 and 67)

Penny, L.R., Ouzts, C. & Gies, D.R. (2008). Tomographic Separation of Composite Spectra. XI. The Physical Properties of the Massive Close Binary HD 100213 (TU Muscae). ApJ, **681**, 554–561. (in p. 18)

Persic, M. & Rephaeli, Y. (2007). Galactic star formation rates gauged by stellar end-products. A&A, **463**, 481–492. (in pp. 5 and 31)

Pettini, M. & Pagel, B.E.J. (2004). [OIII]/[NII] as an abundance indicator at high redshift. MNRAS, **348**, L59–L63. (in p. 81)

Pfahl, E., Rappaport, S., Podsiadlowski, P. & Spruit, H. (2002). A New Class of High-Mass X-Ray Binaries: Implications for Core Collapse and Neutron Star Recoil. ApJ, **574**, 364–376. (in p. 31)

Piffl, T., Scannapieco, C., Binney, J., Steinmetz, M., Scholz, R.D., Williams, M.E.K., de Jong, R.S., Kordopatis, G., Matijevič, G., Bienaymé, O., Bland-Hawthorn, J., Boeche, C., Freeman, K., Gibson, B., Gilmore, G., Grebel, E.K., Helmi, A., Munari, U., Navarro, J.F., Parker, Q., Reid, W.A., Seabroke, G., Watson, F., Wyse, R.F.G. & Zwitter, T. (2014). The RAVE survey: the Galactic escape speed and the mass of the Milky Way. A&A, **562**, A91. (in p. 61)

Podsiadlowski, P. & Rappaport, S. (2000). Cygnus X-2: The Descendant of an Intermediate-Mass X-Ray Binary. ApJ, **529**, 946–951. (in p. 9)

Podsiadlowski, P., Langer, N., Poelarends, A.J.T., Rappaport, S., Heger, A. & Pfahl, E. (2004). The Effects of Binary Evolution on the Dynamics of Core Collapse and Neutron Star Kicks. ApJ, **612**, 1044–1051. (in p. 31)

Politakis, B., Zezas, A., Andrews, J.J. & Williams, S.J. (2020). Vertical distribution of HMXBs in NGC 55: Constraining their centre of mass velocity. MNRAS. (in p. 116)

Ponnada, S., Brorby, M. & Kaaret, P. (2019). Effects of metallicity on high-mass X-ray binary formation. *Monthly Notices of the Royal Astronomical Society*, **491**, 3606–3612. (in p. 29)

Porter, J.M. & Rivinius, T. (2003). Classical Be Stars. PASP, **115**, 1153–1170. (in p. 6)

Pozzetti, L., Bolzonella, M., Zucca, E., Zamorani, G., Lilly, S., Renzini, A., Moresco, M., Mignoli, M., Cassata, P., Tasca, L., Lamareille, F., Maier, C., Meneux, B., Halliday, C., Oesch, P., Vergani, D., Caputi, K., Kovač, K., Cimatti, A., Cucciati, O., Iovino, A., Peng, Y., Carollo, M., Contini, T., Kneib, J.P., Le Févre, O., Mainieri, V., Scodeggio, M., Bardelli, S., Bongiorno, A., Coppa, G., de la Torre, S., de Ravel, L., Franzetti, P., Garilli, B., Kampczyk, P., Knobel, C., Le Borgne, J.F., Le Brun, V., Pellò, R., Perez Montero, E., Ricciardelli, E., Silverman, J.D., Tanaka, M., Tresse, L., Abbas, U., Bottini, D., Cappi, A., Guzzo, L., Koekemoer, A.M., Leauthaud, A., Maccagni, D., Marinoni, C., McCracken, H.J., Memeo, P., Porciani, C., Scaramella, R., Scarlata, C. & Scoville, N. (2010). zCOSMOS - 10k-bright spectroscopic sample. The bimodality in the galaxy stellar mass function: exploring its evolution with redshift. A&A, **523**, A13. (in pp. 82 and 84)

Reig, P. (2011). Be/X-ray binaries. Ap&SS, **332**, 1–29. (in pp. 6 and 7)

Renzo, M., Zapartas, E., de Mink, S.E., Götberg, Y., Justham, S., Farmer, R.J., Izzard, R.G., Toonen, S. & Sana, H. (2019). Massive runaway and walkaway stars. A study of the kinematical imprints of the physical processes governing the evolution and explosion of their binary progenitors. A&A, **624**, A66. (in pp. 63 and 116)

Revnivtsev, M. & Mereghetti, S. (2015). Magnetic Fields of Neutron Stars in X-Ray Binaries. Space Sci. Rev., **191**, 293–314. (in p. 4)

Ritter, H. & Kolb, U. (2003). Catalogue of cataclysmic binaries, low-mass X-ray binaries and related objects (Seventh edition). A&A, **404**, 301–303. (in pp. 9 and 10)

Rowan-Robinson, M. (2001). The star formation history of the universe: An infrared perspective. *The Astrophysical Journal*, **549**, 745. (in p. 81)

Sana, H., de Mink, S.E., de Koter, A., Langer, N., Evans, C.J., Gieles, M., Gosset, E., Izzard, R.G., Le Bouquin, J.B. & Schneider, F.R.N. (2012). Binary Interaction Dominates the Evolution of Massive Stars. *Science*, **337**, 444. (in p. 15)

Schreier, E., Levinson, R., Gursky, H., Kellogg, E., Tananbaum, H. & Giacconi, R. (1972). Evidence for the Binary Nature of Centaurus X-3 from UHURU X-Ray Observations. ApJ, **172**, L79. (in p. 5)

Seth, A.C., Dalcanton, J.J. & de Jong, R.S. (2005). A Study of Edge-On Galaxies with the Hubble Space Telescope Advanced Camera for Surveys. II. Vertical Distribution of the Resolved Stellar Population. AJ, **130**, 1574–1592. (in p. 33)

She, R., Ho, L.C. & Feng, H. (2017). Chandra Survey of Nearby Galaxies: The Catalog. ApJ, **835**, 223. (in p. 74)

Sipahi, E., Ibanoglu, C., Cakirli, O., Dal, H.A. & Evren, S. (2013). V1135 Herculis: a double-lined eclipsing binary with an Anomalous Cepheid. *Rev. Mex. Astron. Astrofis.*, **49**, 239. (in p. 18)

Soria, R. & Wu, K. (2003). Properties of discrete X-ray sources in the starburst spiral galaxy M 83. A&A, **410**, 53–74. (in p. 28)

Soydugan, F., Soydugan, E. & Frasca, A. (2007). A Spectroscopic Survey of Algol-type Binary S Equ. In O. Demircan, S.O. Selam & B. Albayrak, eds., *Solar and Stellar Physics Through Eclipses*, vol. 370 of *Astronomical Society of the Pacific Conference Series*, 201. (in pp. 17 and 18)

Stampoulis, V., van Dyk, D.A., Kashyap, V.L. & Zezas, A. (2019). Multidimensional data-driven classification of emission-line galaxies. MNRAS, **485**, 1085–1102. (in p. 74)

Stern, D., Eisenhardt, P., Gorjian, V., Kochanek, C., Caldwell, N., Eisenstein, D., Brodwin, M., Brown, M., Cool, R., Dey, A., Green, P., Jannuzi, B., Murray, S., Pahre, M. & Willner, S. (2005). Mid-Infrared Selection of Active Galaxies. ApJ, **631**, 163–168. (in pp. 38 and 39)

Stevens, I.R. & Strickland, D.K. (1998). A ROSAT survey of Wolf-Rayet galaxies. MNRAS, **294**, 523–547. (in p. 25)

Stobbart, A.M., Roberts, T.P. & Warwick, R.S. (2006). The X-ray properties of the dwarf Magellanic-type galaxy NGC 55. MNRAS, **370**, 25–42. (in p. 53)

Surkova, L.P. & Svechnikov, M.A. (2004). VizieR Online Data Catalog: Semi-detached eclipsing binaries (Surkova+, 2004). *VizieR Online Data Catalog*. (in p. 18)

Tauris, T., Heuvel, E. & Savonije, G. (2000). Formation of millisecond pulsars with heavy white dwarf companions:extreme mass transfer on subthermal timescales. *The Astrophysical journal*, **530**, L93–L96. (in p. 9)

Tauris, T.M. & van den Heuvel, E.P.J. (2006). Formation and evolution of compact stellar X-ray sources. *Cambridge University Press*, 623–665. (in pp. 11, 13, 14, and 17)

Tremonti, C.A., Heckman, T.M., Kauffmann, G., Brinchmann, J., Charlot, S., White, S.D.M., Seibert, M., Peng, E.W., Schlegel, D.J., Uomoto, A., Fukugita, M. & Brinkmann, J. (2004). The Origin of the Mass-Metallicity Relation: Insights from 53,000 Star-forming Galaxies in the Sloan Digital Sky Survey. ApJ, **613**, 898–913. (in p. 81)

Tzanavaris, P., Fragos, T., Tremmel, M., Jenkins, L., Zezas, A., Lehmer, B.D., Hornschemeier, A., Kalogera, V., Ptak, A. & Basu-Zych, A.R. (2013). Modeling X-Ray Binary Evolution in Normal Galaxies: Insights from SINGS. ApJ, **774**, 136. (in p. 27)

van den Heuvel, E.P.J., Portegies Zwart, S.F., Bhattacharya, D. & Kaper, L. (2000). On the origin of the difference between the runaway velocities of the OB-supergiant X-ray binaries and the Be/X-ray binaries. A&A, **364**, 563–572. (in pp. 64 and 66)

van der Marel, R.P., Kallivayalil, N. & Besla, G. (2009). Kinematical structure of the Magellanic System. In J.T. Van Loon & J.M. Oliveira, eds., *The Magellanic System: Stars, Gas, and Galaxies*, vol. 256 of *IAU Symposium*, 81–92. (in p. 66)

van Rensbergen, W., Vanbeveren, D. & De Loore, C. (1996). OB-runaways as a result of massive star evolution. A&A, **305**, 825. (in p. 31)

Voss, R. & Tauris, T.M. (2003). Galactic distribution of merging neutron stars and black holes - prospects for short gamma-ray burst progenitors and LIGO/VIRGO. MNRAS, **342**, 1169–1184. (in pp. 20 and 21)

Wang, S., Qiu, Y., Liu, J. & Bregman, J.N. (2018). VizieR Online Data Catalog: Chandra ACIS survey in nearby galaxies. II (Wang+, 2016). *VizieR Online Data Catalog*, J/ApJ/829/20. (in pp. 26 and 67)

Webster, B.L. & Murdin, P. (1972). Cygnus X-1-a Spectroscopic Binary with a Heavy Companion ? Nature, **235**, 37–38. (in p. 5)

Weisz, D.R., Dalcanton, J.J., Williams, B.F., Gilbert, K.M., Skillman, E.D., Seth, A.C., Dolphin, A.E., McQuinn, K.B.W., Gogarten, S.M., Holtzman, J., Rosema, K., Cole, A., Karachentsev, I.D. & Zaritsky, D. (2011). The ACS Nearby Galaxy Survey Treasury. VIII. The Global Star Formation Histories of 60 Dwarf Galaxies in the Local Volume. ApJ, **739**, 5. (in pp. 33, 63, and 66)

Westmeier, T., Koribalski, B.S. & Braun, R. (2013). Gas and dark matter in the Sculptor group: NGC 55. MNRAS, **434**, 3511–3525. (in pp. 32 and 33)

Williams, S.J. & Bonanos, A.Z. (2016). Spitzer mid-infrared point sources in the fields of nearby galaxies. A&A, **587**, A121. (in p. 35)

Williams, S.J., Bonanos, A.Z., Whitmore, B.C., Prieto, J.L. & Blair, W.P. (2015). The infrared massive stellar content of M 83. A&A, **578**, A100. (in pp. 38 and 39)

Wong, R.K.W., Kashyap, V.L., Lee, T.C.M. & van Dyk, D.A. (2015). Detecting Abrupt Changes in the Spectra of High-Energy Astrophysical Sources. *ArXiv e-prints*. (in p. 53)

Wright, N.J., Drake, J.J., Guarcello, M.G., Kashyap, V.L. & Zezas, A. (2015). Simulating the sensitivity to stellar point sources of Chandra X-ray observations. *arXiv e-prints*, arXiv:1511.03943. (in pp. 74 and 75)

Wu, H., Cao, C., Hao, C.N., Liu, F.S., Wang, J.L., Xia, X.Y., Deng, Z.G. & Young, C.K.S. (2005). PAH and Mid-Infrared Luminosities as Measures of Star Formation Rate in Spitzer First Look Survey Galaxies. ApJ, **632**, L79–L82. (in p. 46)

Yerli, S.K., Sarna, M.J., Zoła, S., Connon Smith, R. & Tovmassian, G. (2003). A photometric–spectroscopic analysis and the evolutionary status of the Algol-type binary U Coronae Borealis. *Monthly Notices of the Royal Astronomical Society*, **342**, 1349–1360. (in p. 18)

Zezas, A., Fabbiano, G., Rots, A.H. & Murray, S.S. (2002). Chandra Observations of "The Antennae" Galaxies (NGC 4038/4039). III. X-Ray Properties and Multiwavelength Associations of the X-Ray Source Population. ApJ, **577**, 710–725. (in p. 31)

Zezas, A., Fabbiano, G., Baldi, A., Schweizer, F., King, A.R., Rots, A.H. & Ponman, T.J. (2007). Chandra monitoring observations of the antennae galaxies. ii. x-ray luminosity functions. *The Astrophysical Journal*, **661**, 135. (in pp. 26, 67, and 74)

Zhang, Z., Gilfanov, M. & Bogdán, Á. (2012). Dependence of the low-mass X-ray binary population on stellar age. A&A, **546**, A36. (in pp. 25, 26, 27, 28, 67, 109, and 121)

Zibetti, S., Charlot, S. & Rix, H.W. (2009). Resolved stellar mass maps of galaxies - I. Method and implications for global mass estimates. MNRAS, **400**, 1181–1198. (in pp. 81 and 109)

Zuo, Z.Y., Li, X.D. & Gu, Q.S. (2013). Population synthesis on high-mass X-ray binaries: prospects and constraints from the universal X-ray luminosity function. *Monthly Notices of the Royal Astronomical Society*, **437**, 1187–1198. (in p. 27)

5 Appendix

Table 5.1 presents the full sample of galaxies and their corresponding properties that are used in the analysis.

Figure 5.1 shows the differential XLFs of star-forming (of type irregular and spiral c,d,m) galaxies as well as the MCMC fitting results from a power-law model (red line). The black dashed line shows the slope as estimated in Section 3.5.2.

Figure 5.2 shows the differential XLFs of spiral a,b galaxies, while Figure 5.3 shows the differential XLFs of early-type galaxies (of type elliptical and irregular).

Table 5.1: Sample of galaxies

Galaxy: Common galaxy name as in *NED*;

Distance: Distance of the galaxy in *Mpc*;

T: Hubble Type classification according to *HyperLEDA* T;

Morph. Type: Morphological type;

$\boldsymbol{D_{25}}$: area of the D_{25} isophote ellipse in $arcmin^2$;

log SFR: Star Formation Rate in $M_\odot$ yr^{-1};

$\boldsymbol{logM_\star}$: Stellar mass in $M_\odot$;

Z: Metallicity in [12+log(O/H)];

log sSFR: Specific SFR in yr^{-1};

$\boldsymbol{L_{20}}$: Sensitivity threshold, corresponding to the luminosity with 20% detection probability, estimated from average values;

$\boldsymbol{N_{src}}$: Number of observed X-ray sources within the D_{25};

$\boldsymbol{N_c}$: Number of X-ray sources corrected for incompleteness ;

$\boldsymbol{N_{f/b}}$: Number of foreground/background X-ray sources

Galaxy	Distance	T	Morph. Type	D_{25}	log SFR	log $M_\star$	**Z**	log sSFR	L_{20}	N_{src}	N_c	$N_{f/b}$
ESO097-013	4.21	3.3	spiral a,b	29.37	0.59	10.17	8.72	-9.58	35.81	93	73.70	4.91
ESO138-010	15.74	7.9	spiral c,d,m	17.37	-0.62	9.94	8.67	-10.56	37.75	5	5.02	0.88
ESO420-009	17.50	5	spiral c,d,m	1.69	-1.78	8.88	8.36	-10.66	37.31	4	3.00	0.05
ESO495-021	8.24	-2.6	lenticular	2.19	-0.20	6.15	8.36	-6.35	38.00	3	3.00	0.04
ESO501-023	7.48	8	spiral c,d,m	5.41	-3.53	7.40	8.04	-10.94	37.19	4	4.00	0.15
ESO548-029	17.50	2.5	spiral a,b	0.83	-1.49	8.97	8.38	-10.46	38.22	1	1.00	0.01
IC0010	0.75	9.9	Irregular	30.96	-1.38	8.57	8.04	-9.95	34.75	39	32.71	6.94
IC0239	14.19	6	spiral c,d,m	13.36	-1.24	9.02	8.40	-10.27	37.92	3	3.00	0.26
IC0342	3.40	6	spiral c,d,m	291.66	0.62	10.15	8.72	-9.53	36.12	62	50.97	30.68
IC0800	14.94	5.3	spiral c,d,m	1.30	-0.89	9.03	8.81	-9.92	38.23	1	1.02	0.00
IC1473	12.42	-2	lenticular	1.15	-1.38	8.86	8.35	-10.24	37.88	1	1.00	0.01
IC1727	7.39	8.9	spiral c,d,m	12.50	-3.53	7.19	8.05	-10.72	37.68	1	1.00	0.02
IC1729	19.45	-3.8	elliptical	2.18	-1.27	9.50	8.55	-10.77	38.10	2	2.00	0.02
IC2574	3.83	8.9	spiral c,d,m	56.48	-4.00	6.73	8.12	-10.73	36.51	10	10.18	3.77
IC3065	16.39	-2.2	lenticular	0.86	-1.79	9.02	8.40	-10.81	37.95	1	1.00	0.01
IC3259	18.19	8	spiral c,d,m	1.07	-0.72	9.15	8.70	-9.87	37.47	1	1.00	0.02
IC3267	17.63	5.9	spiral c,d,m	1.11	-0.76	9.08	8.75	-9.84	38.03	1	1.00	0.00
IC3292	15.76	-2.7	lenticular	0.70	-2.02	8.74	8.32	-10.77	37.42	1	1.00	0.02
IC3381	16.83	-4.1	elliptical	0.82	0.01	9.24	8.47	-9.23	37.97	1	1.00	0.00
IC3443	18.78	-5	elliptical	0.22		8.74	8.31		37.98	1	1.00	0.00
IC3470	16.08	-4.8	elliptical	0.71	-1.86	9.04	8.41	-10.90	37.93	1	1.00	0.01
IC3492	15.85	-3.8	elliptical	0.31	-2.43	8.17	8.15	-10.60	37.92	1	1.00	0.00
IC3583	9.59	9.6	Irregular	0.43	-1.39	8.45	8.23	-9.84	38.11	1	1.00	0.00
IC3612	14.65	-1.7	lenticular	0.52	-2.16	8.40	8.21	-10.56	37.85	1	1.00	0.00
IC4710	7.38	8.9	spiral c,d,m	8.24	-2.08	7.16	8.05	-9.24	36.64	5	5.07	0.32

Galaxy	Distance	T	Morph. Type	D_{25}	log SFR	log $M_\star$	**Z**	log sSFR	L_{20}	N_{src}	N_c	$N_{f/b}$
IC5325	18.11	4.2	spiral c,d,m	5.94	-0.08	6.46	8.20	-6.54	38.11	2	2.00	0.14
IC5332	8.39	6.8	spiral c,d,m	27.41	-2.05	8.64	8.28	-10.69	36.48	27	26.00	3.98
NGC0024	7.62	5.1	spiral c,d,m	11.66	-2.33	8.14	8.15	-10.48	36.51	11	11.00	1.21
NGC0045	6.70	7.8	spiral c,d,m	21.08	-0.77	9.42	8.53	-10.19	36.76	11	8.06	1.33
NGC0055	2.06	8.8	spiral c,d,m	71.43	-3.05	7.18	8.05	-10.23	35.43	72	69.40	19.87
NGC0205	0.87	-4.8	elliptical	122.14	-2.36	8.26	8.18	-10.63	35.37	15	15.56	7.32
NGC0221	0.77	-4.8	elliptical	29.57	-2.00	8.63	8.28	-10.64	34.44	16	8.00	2.40
NGC0247	3.64	6.9	spiral c,d,m	85.68	-0.77	9.47	8.54	-10.24	36.94	14	14.55	3.81
NGC0253	3.53	5.1	spiral c,d,m	96.35	0.65	10.43	8.76	-9.78	35.80	182	169.16	33.32
NGC0278	11.86	3	spiral a,b	4.25	0.02	10.02	8.69	-10.00	37.02	10	8.10	0.38
NGC0300	1.94	6.9	spiral c,d,m	199.01	-2.31	8.70	8.30	-11.01	35.47	77	74.23	50.48
NGC0337	19.06	6.7	spiral c,d,m	4.32	-1.23	8.40	8.21	-9.63	37.97	12	12.10	0.33
NGC0404	3.09	-2.8	lenticular	8.99	-2.00	9.20	8.58	-11.19	35.51	8	8.15	0.38
NGC0598	0.85	5.9	spiral c,d,m	1790.07	-2.13	8.40	8.21	-10.53	34.88	690	550.22	375.28
NGC0625	4.02	9	spiral c,d,m	10.52	-1.20	8.58	8.26	-9.78	35.91	8	6.10	0.45
NGC0628	10.04	5.2	spiral c,d,m	72.42	-0.15	10.08	8.70	-10.23	36.87	107	92.71	17.84
NGC0660	13.78	1.2	spiral a,b	6.05	0.60	10.16	8.64	-9.56	37.29	12	10.07	0.59
NGC0672	7.42	6	spiral c,d,m	14.92	-1.41	8.92	8.37	-10.33	37.69	1	1.00	0.01
NGC0685	17.29	5.4	spiral c,d,m	5.44	-0.66	9.63	8.59	-10.28	38.08	1	1.00	0.05
NGC0855	9.03	-4.8	elliptical	2.49	-1.97	8.10	8.14	-10.07	36.63	4	4.00	0.13
NGC0891	9.11	3.1	spiral a,b	30.96	0.25	10.65	8.78	-10.40	36.52	65	63.22	8.71
NGC0925	10.35	7	spiral c,d,m	48.40	-1.80	8.32	8.19	-10.12	38.09	7	7.01	0.96
NGC0949	10.29	3.4	spiral a,b	3.29	-0.93	9.34	8.50	-10.27	37.87	1	1.00	0.03
NGC0959	10.98	7.9	spiral c,d,m	1.63	-1.55	8.95	8.38	-10.50	38.00	1	1.00	0.00
NGC0988	15.71	5.9	spiral c,d,m	5.81	0.50	10.34	8.47	-9.84	37.91	3	3.00	0.11

Galaxy	Distance	T	Morph. Type	D_{25}	log SFR	log $M_\star$	**Z**	log sSFR	L_{20}	N_{src}	N_c	$N_{f/b}$
NGC0991	18.79	5.2	spiral c,d,m	1.52	-1.30	9.49	8.75	-10.79	38.08	1	1.00	0.01
NGC1012	16.24	0.3	spiral a,b	1.74	-1.06	8.94	8.38	-10.00	38.12	4	4.00	0.02
NGC1023	10.49	-2.6	lenticular	17.78	-1.29	10.61	8.77	-11.90	36.82	55	50.70	4.36
NGC1042	9.26	6	spiral c,d,m	6.53	-2.20	8.21	8.65	-10.41	36.94	8	8.10	0.36
NGC1052	19.20	-4.7	elliptical	4.82	-0.49	9.86	8.65	-10.35	37.40	38	34.06	1.04
NGC1055	18.86	3.1	spiral a,b	19.18	0.44	10.81	8.78	-10.37	38.06	6	6.00	0.77
NGC1058	9.46	5.1	spiral c,d,m	2.62	-0.99	9.32	8.50	-10.30	37.00	3	3.00	0.05
NGC1068	10.41	3	spiral a,b	24.48	1.37	10.57	8.79	-9.20	36.80	47	46.04	6.51
NGC1073	15.21	5.3	spiral c,d,m	6.21	-1.73	7.72	8.07	-9.45	37.76	3	3.00	0.15
NGC1097	15.45	3.3	spiral a,b	53.56	0.58	10.75	8.78	-10.18	37.88	30	30.40	7.03
NGC1156	6.37	9.8	Irregular	5.46	-1.49	8.99	8.39	-10.48	37.67	3	2.00	0.04
NGC1232	15.34	5	spiral c,d,m	30.75	-0.18	10.20	8.72	-10.38	37.06	47	56.60	7.73
NGC1291	8.01	0.1	spiral a,b	87.27	-0.45	10.36	8.75	-10.80	36.75	110	104.56	24.22
NGC1300	16.18	4	spiral a,b	14.25	-0.26	9.72	8.62	-9.98	37.38	22	22.17	2.96
NGC1313	4.31	7	spiral c,d,m	79.41	-1.36	9.05	8.41	-10.41	36.39	32	29.16	12.02
NGC1325A	17.60	6.9	spiral c,d,m	2.65	-2.26	8.30	8.19	-10.56	38.03	1	1.00	0.03
NGC1340	19.84	-4	elliptical	12.59	-0.82	9.94	8.67	-10.76	38.38	3	3.00	0.20
NGC1365	18.15	3.2	spiral a,b	57.93	0.91	10.91	8.78	-9.99	37.78	58	52.07	15.27
NGC1370	19.05	-3.7	elliptical	1.00	-1.07	9.41	8.53	-10.48	38.38	1	1.00	0.01
NGC1380	18.71	-2.3	lenticular	7.98	-0.17	10.71	8.78	-10.88	37.37	42	39.18	1.73
NGC1386	15.91	-0.7	lenticular	3.50	-0.12	10.12	8.71	-10.25	37.36	13	11.10	0.24
NGC1387	19.07	-2.8	lenticular	7.06	-1.84	10.49	8.77	-12.33	37.25	14	14.03	0.98
NGC1389	19.34	-2.8	lenticular	2.90	-1.99	10.35		-12.34	37.28	7	7.01	0.11
NGC1427	19.35	-4	elliptical	9.68	-0.75	10.18	8.72	-10.93	37.34	50	48.01	2.07
NGC1427A	10.86	9.9	Irregular	2.52	-1.42	8.61	8.28	-10.03	36.65	5	5.00	0.06

Galaxy	Distance	T	Morph. Type	D_{25}	log SFR	log $M_\star$	**Z**	log sSFR	L_{20}	N_{src}	N_c	$N_{f/b}$
NGC1493	11.32	6	spiral c,d,m	8.65	-2.82	7.81	8.08	-10.64	37.39	5	5.00	0.45
NGC1511	15.28	2	spiral a,b	4.19	0.35	9.79	8.63	-9.44	37.33	10	10.00	0.34
NGC1536	15.54	4.6	spiral c,d,m	1.59	-1.23	9.22	8.47	-10.46	37.93	1	1.00	0.01
NGC1549	17.56	-4.3	elliptical	17.53	-0.29	10.66	8.78	-10.95	37.43	59	55.51	4.93
NGC1553	17.53	-2.3	lenticular	21.08	-0.02	10.91	8.78	-10.93	38.22	3	2.00	0.19
NGC1569	3.07	9.6	Irregular	6.62	-0.06	8.57	8.26	-8.63	35.65	12	11.01	0.42
NGC1637	12.37	5	spiral c,d,m	6.84	-0.37	9.88	8.66	-10.24	37.03	16	10.20	0.69
NGC1640	19.05	3	spiral a,b	5.52	-0.93	10.10	8.71	-11.04	38.10	2	2.00	0.09
NGC1672	16.44	3.3	spiral a,b	26.23	0.53	10.55	8.77	-10.01	37.37	31	30.02	5.90
NGC1703	18.62	3.2	spiral a,b	5.28	-0.22	9.90	8.66	-10.12	38.10	4	4.00	0.15
NGC1705	5.46	-2.7	lenticular	2.12	-2.76	8.13	8.15	-10.89	36.09	2	2.00	0.10
NGC1800	8.02	8	spiral c,d,m	1.41	-2.12	8.59	8.27	-10.72	36.50	1	1.00	0.00
NGC1808	9.47	1.2	spiral a,b	7.94	0.64	10.03	8.69	-9.39	36.71	24	24.01	1.48
NGC2082	14.35	3.1	spiral a,b	2.90	-0.68	9.50	8.55	-10.18	37.87	2	2.00	0.05
NGC2337	11.52	9.8	Irregular	2.76	-1.54	8.82	8.34	-10.35	38.12	1	1.00	0.00
NGC2403	3.17	6	spiral c,d,m	157.71	-0.36	9.56	8.57	-9.92	35.95	118	99.16	37.88
NGC2500	10.05	7	spiral c,d,m	4.53	-2.69	7.65	8.06	-10.34	37.87	5	5.00	0.11
NGC2541	11.92	6	spiral c,d,m	3.79	-1.69	9.00	8.40	-10.69	38.03	1	1.00	0.00
NGC2681	16.50	0.4	spiral a,b	12.38	-0.76	9.64	8.59	-10.41	36.90	23	21.07	1.60
NGC2683	9.04	3	spiral a,b	20.08	-0.48	10.47	8.76	-10.95	36.98	16	16.00	3.07
NGC2748	19.44	4	spiral a,b	2.27	0.01	10.01	8.69	-10.00	37.53	10	10.00	0.20
NGC2787	7.42	-1	lenticular	4.59	-1.05	9.78	8.63	-10.83	36.70	18	18.45	0.75
NGC2841	14.51	2.9	spiral a,b	17.94	-2.36	9.74	8.62	-12.10	37.39	45	36.15	4.41
NGC2903	9.43	4	spiral a,b	49.53	0.38	10.53	8.77	-10.15	36.60	79	72.01	14.08
NGC2915	4.03	1.6	spiral a,b	1.40	-3.11	8.15	8.15	-11.26	36.40	1	1.00	0.01

Galaxy	Distance	T	Morph. Type	D_{25}	log SFR	log $M_\star$	**Z**	log sSFR	L_{20}	N_{src}	N_c	$N_{f/b}$
NGC2976	3.56	5.2	spiral c,d,m	13.61	-1.19	9.07	8.42	-10.26	36.42	8	8.00	1.30
NGC2997	11.46	5.1	spiral c,d,m	50.68	0.38	10.52	8.77	-10.14	37.04	64	64.30	13.92
NGC3031	3.59	2.4	spiral a,b	190.93	-0.48	10.01	8.69	-10.48	35.98	186	164.54	57.12
NGC3034	3.49	7.2	spiral c,d,m	44.04	0.85	10.01	8.69	-9.16	35.76	125	115.30	14.21
NGC3077	3.80	6.1	spiral c,d,m	17.66	-2.20	7.13	8.05	-9.33	35.79	18	18.01	2.50
NGC3079	19.02	6.4	spiral c,d,m	8.30	0.61	10.63	8.78	-10.02	37.46	26	25.04	1.66
NGC3115	10.18	-2.9	lenticular	15.92	-0.85	10.76	8.78	-11.61	36.33	157	135.23	4.63
NGC3125	14.98	-5	elliptical	0.92	-0.76	8.84	8.34	-9.60	37.04	4	4.00	0.02
NGC3184	11.16	5.9	spiral c,d,m	41.67	-0.26	9.54	8.56	-9.80	37.08	43	36.21	11.01
NGC3198	14.39	5.2	spiral c,d,m	9.33	-0.18	10.08	8.70	-10.26	36.94	17	17.07	1.13
NGC3239	8.05	9.8	Irregular	7.69	-0.66	9.47	8.54	-10.13	37.17	5	5.00	0.11
NGC3274	13.37	6.7	spiral c,d,m	1.03	-1.69	8.91	8.37	-10.60	38.27	1	1.00	0.00
NGC3287	15.40	7.6	spiral c,d,m	1.19	-1.60	8.20	8.76	-9.80	37.57	5	5.00	0.06
NGC3299	5.40	8	spiral c,d,m	1.87	-2.60	8.45	8.23	-11.05	36.99	1	1.00	0.02
NGC3310	18.57	4	spiral a,b	2.45	-0.45	9.02	8.40	-9.47	37.38	18	17.00	0.14
NGC3344	9.77	4	spiral a,b	33.49	-0.50	5.90	8.53	-6.40	36.87	31	30.04	7.12
NGC3351	10.01	3.1	spiral a,b	25.23	-0.28	10.31	8.74	-10.60	36.95	41	37.68	3.88
NGC3353	18.11	4.1	spiral c,d,m	1.04	-0.14	9.09	8.31	-9.23	37.67	5	5.00	0.05
NGC3368	10.83	2.1	spiral a,b	35.72	-0.56	10.62	8.77	-11.17	37.94	7	7.01	1.21
NGC3377	10.91	-4.8	elliptical	5.69	-0.96	9.90	8.66	-10.86	36.76	24	22.01	0.91
NGC3379	10.44	-4.8	elliptical	16.44	-1.10	9.52	8.56	-10.62	36.67	95	78.47	4.20
NGC3384	10.67	-2.6	lenticular	9.75	-1.16	9.53	8.56	-10.69	36.63	34	33.92	1.46
NGC3395	19.64	5.8	spiral c,d,m	1.11	-1.52	8.62	8.28	-10.14	37.90	7	6.00	0.07
NGC3412	11.24	-2	lenticular	6.74	-1.38	9.38	8.52	-10.76	37.40	7	7.00	0.52
NGC3413	15.83	-1.1	lenticular	1.34	-0.98	9.08	8.32	-10.06	38.36	2	2.00	0.01

Galaxy	Distance	T	Morph. Type	D_{25}	log SFR	log $M_\star$	**Z**	log sSFR	L_{20}	N_{src}	N_c	$N_{f/b}$
NGC3432	12.75	8.9	spiral c,d,m	12.10	-1.69	8.11	8.39	-9.80	38.27	2	2.00	0.01
NGC3445	17.22	8.8	spiral c,d,m	1.41	-1.00	9.01	8.40	-10.01	37.85	1	1.00	0.01
NGC3495	18.24	6.2	spiral c,d,m	3.67	-1.45	8.54	8.25	-9.98	38.17	1	1.00	0.01
NGC3507	14.74	3.1	spiral a,b	5.74	-0.42	10.15	8.72	-10.57	37.01	18	17.00	0.86
NGC3521	13.35	4	spiral a,b	29.17	0.57	10.98	8.77	-10.41	36.87	77	77.77	8.66
NGC3556	9.90	5.9	spiral c,d,m	5.19	0.12	9.97	8.68	-9.85	36.62	39	38.27	1.34
NGC3585	19.87	-4.8	elliptical	16.98	-0.17	10.74	8.78	-10.91	37.30	67	72.26	4.70
NGC3593	8.77	-0.4	lenticular	6.81	-0.95	9.14	8.44	-10.09	38.14	3	4.40	0.07
NGC3599	19.99	-2	lenticular	4.10	-1.51	9.09	8.43	-10.60	37.65	8	8.07	0.31
NGC3623	12.68	1	spiral a,b	11.80	-1.93	9.44	8.54	-11.38	38.10	4	4.00	0.25
NGC3627	10.41	3.1	spiral a,b	37.23	0.48	10.65	8.78	-10.17	36.83	77	71.08	11.32
NGC3628	10.48	3.1	spiral a,b	29.84	0.28	10.64	8.78	-10.36	36.65	42	41.00	7.73
NGC3631	18.32	5.1	spiral c,d,m	8.99	0.14	3.84	11.82	-3.70	37.14	36	32.00	1.81
NGC3877	15.53	5.1	spiral c,d,m	5.19	-0.05	10.29	8.90	-10.34	37.19	22	24.86	0.78
NGC3887	18.69	3.9	spiral a,b	10.11	-0.01	10.26	8.74	-10.27	38.14	4	4.00	0.22
NGC3922	16.98	-0.2	lenticular	0.97	-1.38	9.28	8.48	-10.65	37.71	1	1.00	0.01
NGC3928	15.66	-3.9	elliptical	1.36	-0.41	9.03	8.72	-9.44	38.12	1	1.00	0.01
NGC3938	16.98	5.1	spiral c,d,m	21.82	-2.62	7.46	8.05	-10.07	37.26	37	38.57	5.58
NGC4013	19.72	3.1	spiral a,b	4.67	-0.06	10.65	8.72	-10.71	37.31	21	21.07	0.69
NGC4026	14.71	-1.8	lenticular	3.67	-1.11	9.53	8.56	-10.64	37.61	4	4.00	0.12
NGC4037	17.22	3.3	spiral a,b	4.14	-1.71	8.64	8.37	-10.35	38.05	1	1.00	0.02
NGC4062	14.60	5.2	spiral c,d,m	5.22	-1.10	8.50	8.81	-9.60	38.19	1	1.00	0.02
NGC4088	14.96	4.7	spiral c,d,m	8.89	0.39	10.24	8.73	-9.85	37.46	24	22.00	1.77
NGC4096	12.18	5.3	spiral c,d,m	6.32	-1.24	8.60	8.85	-9.84	38.36	2	2.00	0.03
NGC4102	19.69	3	spiral a,b	3.92	-1.62	9.00	8.80	-10.62	38.17	2	2.00	0.05

Galaxy	Distance	T	Morph. Type	D_{25}	log SFR	log $M_\star$	**Z**	log sSFR	L_{20}	N_{src}	N_c	$N_{f/b}$
NGC4111	9.98	-1.3	lenticular	0.89	-2.30	9.36	8.51	-11.66	37.35	3	3.00	0.01
NGC4136	9.68	5.2	spiral c,d,m	4.01	-2.87	7.89	8.10	-10.76	36.91	11	9.38	0.28
NGC4150	13.62	-2.1	lenticular	2.07	-1.38	9.09	8.43	-10.48	38.15	4	4.00	0.03
NGC4151	7.79	1.9	spiral a,b	5.00	-0.22	9.78	8.47	-10.00	36.33	11	8.00	0.22
NGC4157	16.95	3.3	spiral a,b	6.09	0.25	10.50	8.77	-10.25	37.42	26	24.00	0.76
NGC4203	15.25	-2.7	lenticular	3.83	-1.60	9.69	8.61	-11.29	37.20	12	12.02	0.30
NGC4204	7.87	7.8	spiral c,d,m	12.91	-1.99	8.43	8.61	-10.42	37.72	2	2.02	0.05
NGC4207	16.12	7.7	spiral c,d,m	0.91	-1.02	8.90	8.74	-9.92	38.37	1	1.00	0.01
NGC4214	2.97	9.8	Irregular	28.18	-1.10	5.20	9.22	-6.31	36.06	27	22.54	5.80
NGC4217	19.06	3	spiral a,b	6.50	0.19	10.61	8.77	-10.42	37.30	24	22.06	1.20
NGC4236	4.40	8	spiral c,d,m	126.44	-3.02	8.02	8.12	-11.04	36.80	15	15.09	7.54
NGC4244	4.33	6	spiral c,d,m	92.23	-3.22	7.23	8.04	-10.45	36.03	12	9.28	5.23
NGC4251	19.17	-1.8	lenticular	2.26	-0.95	9.67	8.60	-10.62	37.96	7	7.03	0.22
NGC4254	14.06	5.2	spiral c,d,m	18.74	0.55	10.47	8.76	-9.92	37.90	12	12.39	1.35
NGC4258	7.31	4	spiral a,b	96.58	-1.23	9.08	8.42	-10.31	36.77	53	61.71	18.61
NGC4262	15.82	-2.6	lenticular	2.07	-1.19	9.71	8.61	-10.89	38.00	2	2.00	0.03
NGC4267	16.01	-2.7	lenticular	3.52	-2.09	8.80	8.33	-10.89	37.93	2	2.00	0.05
NGC4278	15.58	-4.8	elliptical	6.42	-2.58	9.81	8.64	-12.39	36.87	136	133.67	1.74
NGC4283	15.85	-4.8	elliptical	1.10	-1.43	9.34	8.50	-10.77	37.09	7	6.00	0.03
NGC4299	16.07	8.4	spiral c,d,m	1.61	-1.56	7.35	8.04	-8.91	37.95	1	1.00	0.02
NGC4303	12.78	4	spiral a,b	35.47	0.43	10.40	8.76	-9.97	37.13	46	41.13	8.34
NGC4309	17.56	-0.7	lenticular	1.39	-1.40	9.58	8.75	-10.98	38.02	1	1.39	0.03
NGC4310	17.30	-0.7	lenticular	1.16	-0.28	9.69	8.83	-9.98	38.29	1	1.00	0.00
NGC4314	18.10	1	spiral a,b	10.35	-1.43	8.84	8.35	-10.28	37.52	14	15.00	1.42
NGC4321	15.42	4	spiral a,b	26.78	0.54	10.83	8.78	-10.29	37.03	65	62.33	6.94

Galaxy	Distance	T	Morph. Type	D_{25}	log SFR	log $M_\star$	**Z**	log sSFR	L_{20}	N_{src}	N_c	$N_{f/b}$
NGC4328	16.67	-3.2	elliptical	1.54	-1.49	8.85	8.37	-10.34	37.93	1	1.00	0.04
NGC4340	18.37	-1.2	lenticular	3.96	-0.96	9.68	8.60	-10.63	38.05	1	1.00	0.04
NGC4342	17.31	-3.2	elliptical	0.63	-1.21	9.67	8.60	-10.88	37.28	7	7.00	0.03
NGC4371	16.96	-1.3	lenticular	5.52	-1.20	9.42	8.53	-10.63	38.02	7	7.02	0.42
NGC4374	17.72	-4.4	elliptical	37.49	-0.09	10.80	8.78	-10.89	37.48	101	88.95	10.29
NGC4377	17.76	-2.6	lenticular	1.55	-1.36	9.56	8.57	-10.91	37.82	3	3.00	0.07
NGC4379	15.59	-2.7	lenticular	2.23	-1.47	9.11	8.43	-10.58	37.90	1	1.00	0.00
NGC4382	17.42	-1.3	lenticular	29.17	-0.02		8.43		37.37	65	59.11	7.57
NGC4387	17.64	-4.8	elliptical	1.16	-1.51	9.27	8.48	-10.78	38.21	1	1.00	0.01
NGC4388	19.18	2.8	spiral a,b	5.44	-0.03	9.69	8.61	-9.72	37.62	10	10.46	0.68
NGC4393	11.31	6.7	spiral c,d,m	6.19	-1.80	9.23	8.47	-11.03	37.68	3	3.00	0.14
NGC4394	16.83	3	spiral a,b	9.16	-1.86	8.18	8.16	-10.04	38.01	5	5.00	0.47
NGC4395	4.82	8.8	spiral c,d,m	4.55	-2.12	8.37	8.20	-10.49	36.29	4	4.18	0.28
NGC4396	12.02	6.8	spiral c,d,m	2.44	-1.44	8.75	8.32	-10.19	38.45	1	1.00	0.00
NGC4402	15.07	3.2	spiral a,b	2.77	-1.80	8.22	8.75	-10.02	37.35	4	4.00	0.11
NGC4406	17.31	-4.8	elliptical	76.36	-0.10	10.99	8.77	-11.10	37.90	59	52.10	12.12
NGC4411B	17.66	6.2	spiral c,d,m	2.59	-1.33	8.92	8.37	-10.25	38.28	1	1.00	0.01
NGC4413	15.93	2.1	spiral a,b	2.39	-1.19	8.59	8.80	-9.79	38.27	1	1.00	0.01
NGC4414	17.62	5.2	spiral c,d,m	1.72	0.46	10.65	8.78	-10.19	37.91	16	16.13	0.16
NGC4417	15.71	-1.9	lenticular	2.65	-1.26	9.34	8.50	-10.61	37.41	8	8.00	0.23
NGC4419	13.55	1.2	spiral a,b	3.96	-0.55	9.53	8.56	-10.09	37.86	3	3.00	0.09
NGC4435	16.73	-2.1	lenticular	5.08	-1.13	9.62	8.59	-10.75	37.59	9	9.07	0.53
NGC4438	11.15	0.6	spiral a,b	28.90	-1.10	10.18	8.72	-11.28	37.03	29	28.01	5.94
NGC4442	15.32	-1.9	lenticular	5.47	-1.02	9.68	8.61	-10.70	37.91	7	7.39	0.37
NGC4449	4.18	9.8	Irregular	9.91	-0.97	9.25	8.48	-10.22	36.01	30	27.75	1.63

Galaxy	Distance	T	Morph. Type	D_{25}	log SFR	log $M_\star$	**Z**	log sSFR	L_{20}	N_{src}	N_c	$N_{f/b}$
NGC4457	17.38	0.3	spiral a,b	5.19	-1.08	9.23	8.47	-10.31	37.22	7	7.00	0.35
NGC4458	16.42	-4.9	elliptical	1.85	-1.65	8.75	8.32	-10.40	37.46	2	2.00	0.05
NGC4459	16.06	-1.6	lenticular	10.35	-0.72	10.64	8.78	-11.36	37.38	16	15.28	0.91
NGC4461	19.77	-0.7	lenticular	3.50	-2.47	8.41	8.22	-10.88	37.84	2	2.00	0.06
NGC4470	15.03	1.9	spiral a,b	0.87	-0.99	8.30	8.69	-9.30	37.74	2	2.00	0.02
NGC4472	15.91	-4.8	elliptical	67.12	-0.76	10.05	8.70	-10.81	37.00	386	357.63	20.69
NGC4473	15.47	-4.7	elliptical	8.41	-0.98	9.84	8.65	-10.82	37.37	31	27.11	1.83
NGC4478	16.83	-4.9	elliptical	1.96	-1.35	9.38	8.52	-10.73	37.79	3	3.00	0.07
NGC4483	16.73	-1.4	lenticular	1.10	-1.58	9.15	8.44	-10.73	37.96	1	1.00	0.02
NGC4485	8.91	9.7	Irregular	2.11	-3.76	7.95	8.11	-11.72	36.87	4	4.00	0.07
NGC4486	16.12	-4.3	elliptical	37.23	0.06	11.88	8.50	-11.83	37.19	231	208.00	12.01
NGC4486A	18.30	-5	elliptical	0.59	-1.23	9.52	8.56	-10.75	37.81	3	3.00	0.02
NGC4486B	16.30	-5	elliptical	0.11	-1.49	9.46	8.54	-10.94	37.76	1	1.00	0.00
NGC4490	9.56	7	spiral c,d,m	8.69	0.26	9.76	8.63	-9.50	37.05	27	26.03	1.35
NGC4494	16.71	-4.8	elliptical	14.09	-0.40	10.36	8.75	-10.76	37.43	30	29.22	2.85
NGC4498	14.68	6.4	spiral c,d,m	3.47	-0.83	7.59	8.06	-8.43	38.62	1	1.00	0.00
NGC4501	19.25	3.3	spiral a,b	29.71	0.55	11.12	8.75	-10.57	37.73	34	34.15	6.12
NGC4515	16.42	-3.2	elliptical	1.12	-1.69	9.02	8.40	-10.71	37.95	1	1.00	0.01
NGC4523	16.83	8.9	spiral c,d,m	1.12	-2.29	8.15	8.15	-10.44	37.80	2	2.00	0.02
NGC4526	15.33	-1.9	lenticular	13.49	-0.82	10.08	8.70	-10.90	37.16	30	30.15	2.29
NGC4527	13.82	4	spiral a,b	8.49	0.06	9.39	8.83	-9.33	37.83	7	7.04	0.45
NGC4528	15.69	-2	lenticular	1.07	-1.42	9.29	8.49	-10.71	37.96	2	2.00	0.03
NGC4550	14.87	-2	lenticular	1.75	-2.84	9.10	8.43	-11.94	37.52	8	8.38	0.19
NGC4551	15.92	-4.9	elliptical	1.69	-1.51	9.25	8.48	-10.76	37.66	2	3.85	0.06
NGC4552	15.51	-4.6	elliptical	51.04	-0.37	10.52	8.77	-10.89	37.04	165	165.90	16.01

Galaxy	Distance	T	Morph. Type	D_{25}	log SFR	log $M_\star$	**Z**	log sSFR	L_{20}	N_{src}	N_c	$N_{f/b}$
NGC4559	8.78	6	spiral c,d,m	39.98	-0.57	9.71	8.61	-10.28	37.26	10	8.00	0.70
NGC4561	17.80	7.2	spiral c,d,m	1.16	-0.55	9.18	8.35	-9.73	38.33	2	2.00	0.01
NGC4564	15.96	-4.6	elliptical	4.14	-1.18	9.64	8.59	-10.81	37.48	9	9.00	0.30
NGC4565	12.80	3.2	spiral a,b	38.01	-1.99	9.48	8.55	-11.48	36.89	61	57.37	8.23
NGC4569	9.86	2.4	spiral a,b	27.34	-0.28	10.36	8.75	-10.64	36.94	38	36.17	6.36
NGC4570	17.11	-1.9	lenticular	2.85	-1.01	9.81	8.64	-10.82	38.03	2	2.00	0.07
NGC4571	14.77	6.4	spiral c,d,m	9.27	-2.17	8.30	8.19	-10.47	37.93	2	2.00	0.22
NGC4578	16.79	-2.1	lenticular	3.43	-1.37	9.21	8.46	-10.59	37.96	2	2.00	0.07
NGC4579	17.07	2.8	spiral a,b	15.10	-0.85	9.86	8.65	-10.71	37.34	24	22.74	1.87
NGC4592	11.18	7.9	spiral c,d,m	3.90	-2.07	7.51	8.54	-9.58	38.01	1	1.00	0.01
NGC4594	9.63	1.1	spiral a,b	32.57	-0.49	11.09	8.76	-11.58	36.62	165	171.56	10.66
NGC4596	19.24	-0.8	lenticular	10.16	-1.50	9.55	8.57	-11.05	37.50	20	19.11	1.31
NGC4612	16.61	-2	lenticular	3.57	-1.36	9.35	8.51	-10.70	37.95	2	2.00	0.08
NGC4618	6.63	8.6	spiral c,d,m	6.40	-1.31	9.06	8.42	-10.37	36.96	7	7.02	0.42
NGC4621	15.31	-4.8	elliptical	11.45	-0.42	10.49	8.76	-10.91	37.26	44	44.93	2.82
NGC4624	15.53	-0.6	lenticular	16.03	-0.50	10.35	8.75	-10.85	37.97	6	6.00	0.53
NGC4625	11.72	8.7	spiral c,d,m	1.17	-1.97	7.95	8.79	-9.91	36.79	6	6.00	0.02
NGC4631	7.49	6.5	spiral c,d,m	24.94	0.32	10.07	8.70	-9.75	36.50	39	36.07	5.40
NGC4636	14.90	-4.8	elliptical	23.44	-0.33	11.14	8.75	-11.47	37.08	85	83.93	7.26
NGC4638	17.45	-2.6	lenticular	2.72	-2.80	7.98	8.26	-10.78	38.33	1	1.00	0.03
NGC4647	16.51	5.1	spiral c,d,m	5.09	-0.07	10.20	8.73	-10.27	37.18	53	40.38	1.11
NGC4649	16.55	-4.6	elliptical	28.96	0.25	11.06	8.76	-10.81	37.10	338	291.34	8.86
NGC4654	14.90	5.9	spiral c,d,m	9.22	-0.81	8.81	8.83	-9.62	38.28	8	7.00	0.15
NGC4660	15.32	-4.6	elliptical	2.59	-1.11	9.54	8.57	-10.65	37.90	6	6.00	0.10
NGC4666	16.18	5	spiral c,d,m	7.67	0.48	10.56	8.77	-10.08	37.99	10	10.00	0.39

Galaxy	Distance	T	Morph. Type	D_{25}	log SFR	log $M_\star$	**Z**	log sSFR	L_{20}	N_{src}	N_c	$N_{f/b}$
NGC4670	11.02	0.7	spiral a,b	0.63	-1.22	8.34	8.20	-9.56	37.30	3	3.00	0.02
NGC4688	17.06	6	spiral c,d,m	10.00	-0.51	9.52	8.56	-10.03	38.10	4	4.10	0.21
NGC4689	16.66	4.7	spiral c,d,m	8.59	-0.43	9.53	8.78	-9.96	38.01	3	3.02	0.32
NGC4691	18.21	0.3	spiral a,b	6.00	-1.07	8.86	8.68	-9.93	37.77	4	4.00	0.21
NGC4697	12.47	-4.5	elliptical	23.60	-0.42	10.53	8.77	-10.95	37.10	89	87.36	7.13
NGC4701	17.87	5.9	spiral c,d,m	1.75	-0.43	9.49	8.55	-9.92	37.91	1	1.00	0.02
NGC4710	17.60	-0.9	lenticular	3.89	-0.95	9.16	8.45	-10.12	37.41	9	8.01	0.37
NGC4713	15.12	6.8	spiral c,d,m	1.99	-1.72	8.01	8.68	-9.73	37.87	1	1.00	0.03
NGC4725	12.59	2.2	spiral a,b	54.06	-0.34	10.52	8.77	-10.85	37.14	54	52.43	13.94
NGC4736	4.64	2.3	spiral a,b	40.63	-0.28	10.38	8.75	-10.66	36.08	61	55.40	11.95
NGC4742	15.46	-4.6	elliptical	2.33	-0.93	9.80	8.64	-10.73	37.30	8	8.00	0.16
NGC4754	16.15	-2.4	lenticular	6.37	-1.06	9.61	8.58	-10.67	37.97	4	4.00	0.11
NGC4762	10.81	-1.8	lenticular	22.85	-1.45	9.11	8.43	-10.56	37.63	1	1.00	0.01
NGC4826	4.69	2.2	spiral a,b	44.04	-0.75	10.13	8.71	-10.88	36.38	39	36.02	9.27
NGC4900	17.30	5.1	spiral c,d,m	3.37	-1.90	8.58	8.27	-10.48	38.03	5	5.00	0.09
NGC4945	3.60	6.1	spiral c,d,m	73.77	0.21	10.19	8.72	-9.98	35.70	109	101.74	16.82
NGC5005	18.70	4	spiral a,b	5.77	-2.34	8.61	8.27	-10.95	38.05	1	1.00	0.07
NGC5054	17.98	4.2	spiral c,d,m	11.48	0.23	10.39	8.75	-10.15	37.80	11	11.30	1.35
NGC5055	8.92	4	spiral a,b	66.51	-1.14	9.30	8.49	-10.44	36.81	73	68.35	17.60
NGC5068	5.16	6	spiral c,d,m	39.25	-1.21	9.10	8.43	-10.30	36.34	23	22.32	6.61
NGC5102	3.61	-2.8	lenticular	28.05	-1.58	9.20	8.46	-10.78	35.93	9	9.00	2.78
NGC5128	3.52	-2.1	lenticular	401.67	0.02	10.90	8.78	-10.88	35.93	534	538.79	140.87
NGC5194	8.60	4	spiral a,b	125.57	0.65	10.73	8.78	-10.08	36.37	346	290.31	40.90
NGC5195	8.59	0.6	spiral a,b	18.79	-0.26	10.37	8.75	-10.63	36.43	27	22.64	2.46
NGC5204	4.79	8.9	spiral c,d,m	9.97	-3.20	7.40	8.04	-10.60	36.36	11	10.10	0.91

Galaxy	Distance	T	Morph. Type	D_{25}	log SFR	log $M_\star$	**Z**	log sSFR	L_{20}	N_{src}	N_c	$N_{f/b}$
NGC5236	4.78	5	spiral c,d,m	140.56	0.60	10.39	8.75	-9.79	35.98	277	258.63	43.60
NGC5248	13.38	4	spiral a,b	7.62	-1.22	9.03	8.41	-10.25	37.16	31	31.05	1.40
NGC5253	3.49	8.9	spiral c,d,m	8.35	-0.77	8.79	8.33	-9.56	35.78	16	15.07	1.43
NGC5273	16.22	-1.9	lenticular	2.76	-1.33	9.16	8.45	-10.49	38.32	1	1.00	0.02
NGC5408	5.11	9.9	Irregular	3.42	-0.83	8.09	8.50	-8.92	36.86	4	3.06	0.10
NGC5457	6.86	5.9	spiral c,d,m	434.38	-0.40	9.88	8.66	-10.28	36.51	442	384.36	141.62
NGC5474	6.91	6.1	spiral c,d,m	2.94	-2.48				36.57	10	10.00	0.37
NGC5585	8.10	6.9	spiral c,d,m	8.77	-2.97	7.34	8.04	-10.31	37.38	3	3.00	0.12
NGC5775	19.30	5.1	spiral c,d,m	2.45	0.44	10.45	8.76	-10.01	37.18	29	29.02	0.52
NGC5866	14.66	-1.3	lenticular	13.49	-2.32	9.35	8.51	-11.67	37.11	33	33.17	2.58
NGC5879	16.71	3.6	spiral a,b	4.24	-1.35	9.51	8.75	-10.86	36.94	9	9.00	0.32
NGC5949	12.47	4	spiral a,b	1.10	-2.06	8.04	8.13	-10.10	37.91	1	1.00	0.00
NGC6300	12.10	3.1	spiral a,b	14.25	0.13	10.39	8.75	-10.27	37.56	11	10.09	0.90
NGC6503	6.16	5.8	spiral c,d,m	9.24	-0.75	9.69	8.61	-10.44	36.79	11	10.42	0.47
NGC6689	13.39	6.4	spiral c,d,m	2.36	-1.59	9.03	8.41	-10.61	37.93	1	1.00	0.02
NGC6822	0.43	9.8	Irregular	179.83	-2.37	7.82	8.23	-10.19	34.33	43	31.11	19.95
NGC6946	5.52	5.9	spiral c,d,m	97.02	0.15	10.10	8.71	-9.95	36.34	134	116.41	29.47
NGC7013	15.91	0.5	spiral a,b	4.34	-0.67	10.46	8.76	-11.13	38.06	5	5.00	0.03
NGC7090	8.60	5	spiral c,d,m	10.23	-0.76	9.55	8.57	-10.31	36.88	12	14.01	0.84
NGC7314	17.38	4	spiral a,b	5.70	-0.04	10.19	8.72	-10.24	37.94	9	8.00	0.19
NGC7320	16.29	6.5	spiral c,d,m	2.81	-1.41	9.11	8.43	-10.52	37.14	4	4.00	0.20
NGC7331	14.40	3.9	spiral a,b	27.34	0.51	10.98	8.77	-10.47	37.22	51	52.46	4.96
NGC7424	11.48	6	spiral c,d,m	10.59	-0.98	6.76	8.11	-7.75	37.07	10	10.90	0.88
NGC7457	12.45	-2.7	lenticular	7.00	-1.07	9.72	8.61	-10.78	37.16	8	8.48	0.51
NGC7552	19.50	2.4	spiral a,b	10.71	0.80	10.56	8.77	-9.76	38.16	6	6.02	0.54

Galaxy	Distance	T	Morph. Type	D_{25}	log SFR	log $M_\star$	**Z**	log sSFR	L_{20}	N_{src}	N_c	$N_{f/b}$
NGC7741	13.93	5.9	spiral c,d,m	6.79	-2.11	8.06	8.13	-10.17	37.95	1	1.00	0.03
NGC7793	3.43	7.4	spiral c,d,m	48.96	-1.07	9.14	8.44	-10.21	35.88	46	41.57	11.22
NGC7814	14.39	2	spiral a,b	6.44	-1.76	9.41	8.53	-11.17	37.25	13	11.07	0.92
PGC003853	11.52	7	spiral c,d,m	10.42	-1.79	9.16	8.45	-10.95	37.41	3	3.00	0.34
PGC009892	3.42	-3	elliptical	0.31	-2.45	10.43		-12.88	36.04	18	18.00	0.05
PGC010217	3.48	4	spiral a,b	0.38	-0.16	9.94	8.67	-10.10	36.55	2	2.00	0.01
PGC013343	19.52	-2.8	lenticular	0.84	-1.98	8.82	8.34	-10.80	37.74	1	1.00	0.00
PGC029653	1.40	9.9	Irregular	18.40	-2.18	8.04	8.12	-10.22	35.30	11	11.08	2.37
PGC039904	16.98	6.5	spiral c,d,m	0.18	-2.42	7.95	8.11	-10.37	38.75	1	1.00	0.00
PGC042884	16.54	-4	elliptical	0.33		8.40	8.21		37.95	1	1.00	0.00
PGC044532	9.89	9	spiral c,d,m	4.33	-3.34	7.93	8.10	-11.27	37.24	6	6.00	0.31
PGC135072	19.73	-5	elliptical	0.37	-1.93	8.91	8.37	-10.84	37.45	1	1.00	0.01
PGC2793573	13.78	-5	elliptical	0.10		7.90	0.00		37.32	1	1.00	0.00
SDSSJ161534.10+192734.8	4.06	-5	elliptical	1.34		6.70	8.36		36.02	5	5.00	0.09
UGC05720	15.42	9.8	Irregular	0.77	-0.28	6.81	8.10	-7.09	37.52	3	3.00	0.02
UGC06988	15.70	9.6	Irregular	0.41	-1.59	8.14	8.59	-9.73	37.48	1	1.00	0.00
UGC08041	15.14	6.9	spiral c,d,m	4.78	-0.86	9.02	8.66	-9.88	37.96	1	1.00	0.01
UGC10310	15.85	9.2	spiral c,d,m	4.07	-2.05	7.49	8.05	-9.54	38.74	1	1.00	0.00
UGC11466	15.09	4	spiral a,b	1.04	-0.42	9.60	8.58	-10.02	38.22	1	1.03	0.01

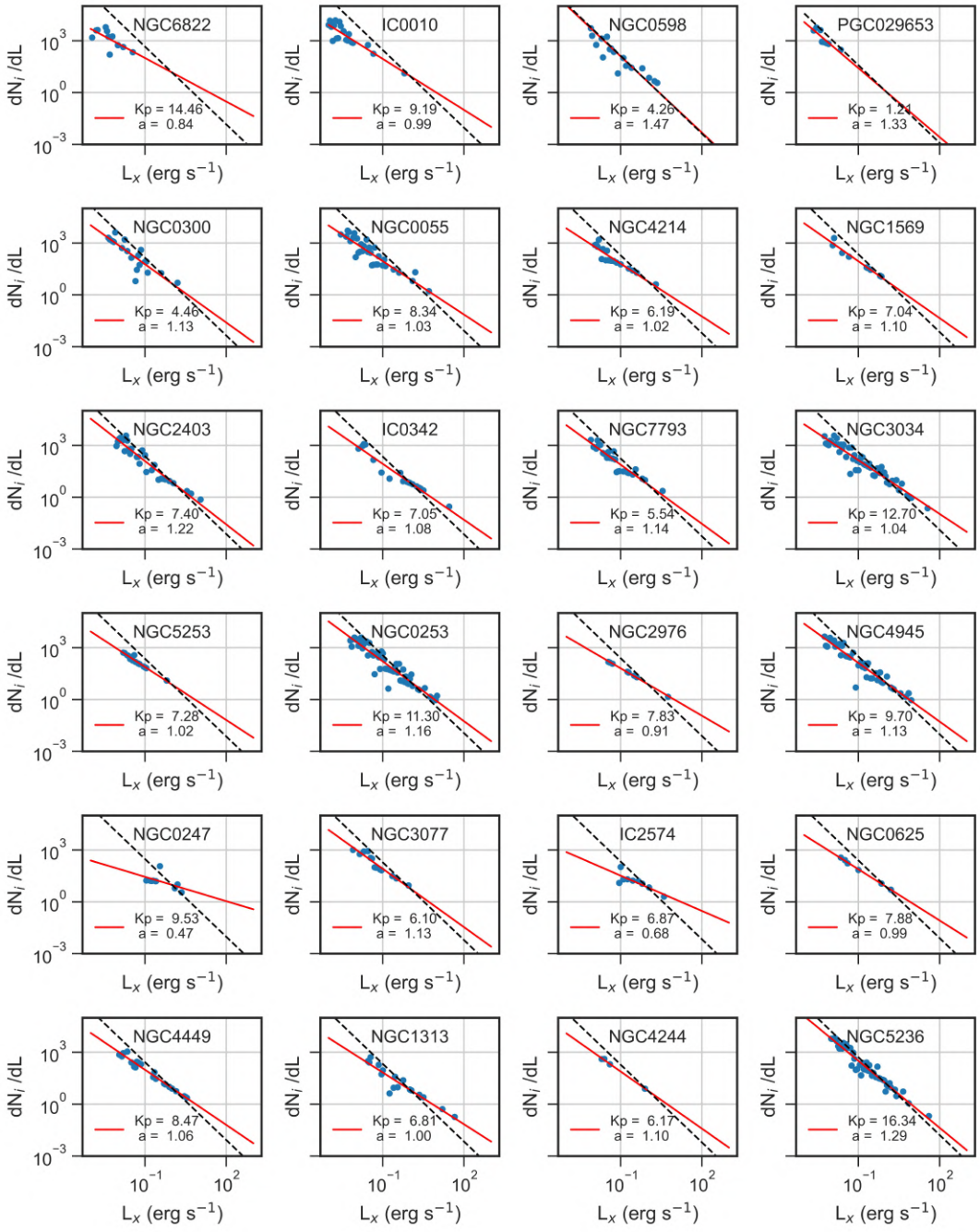

Figure 5.1: XLFs of star-forming galaxies

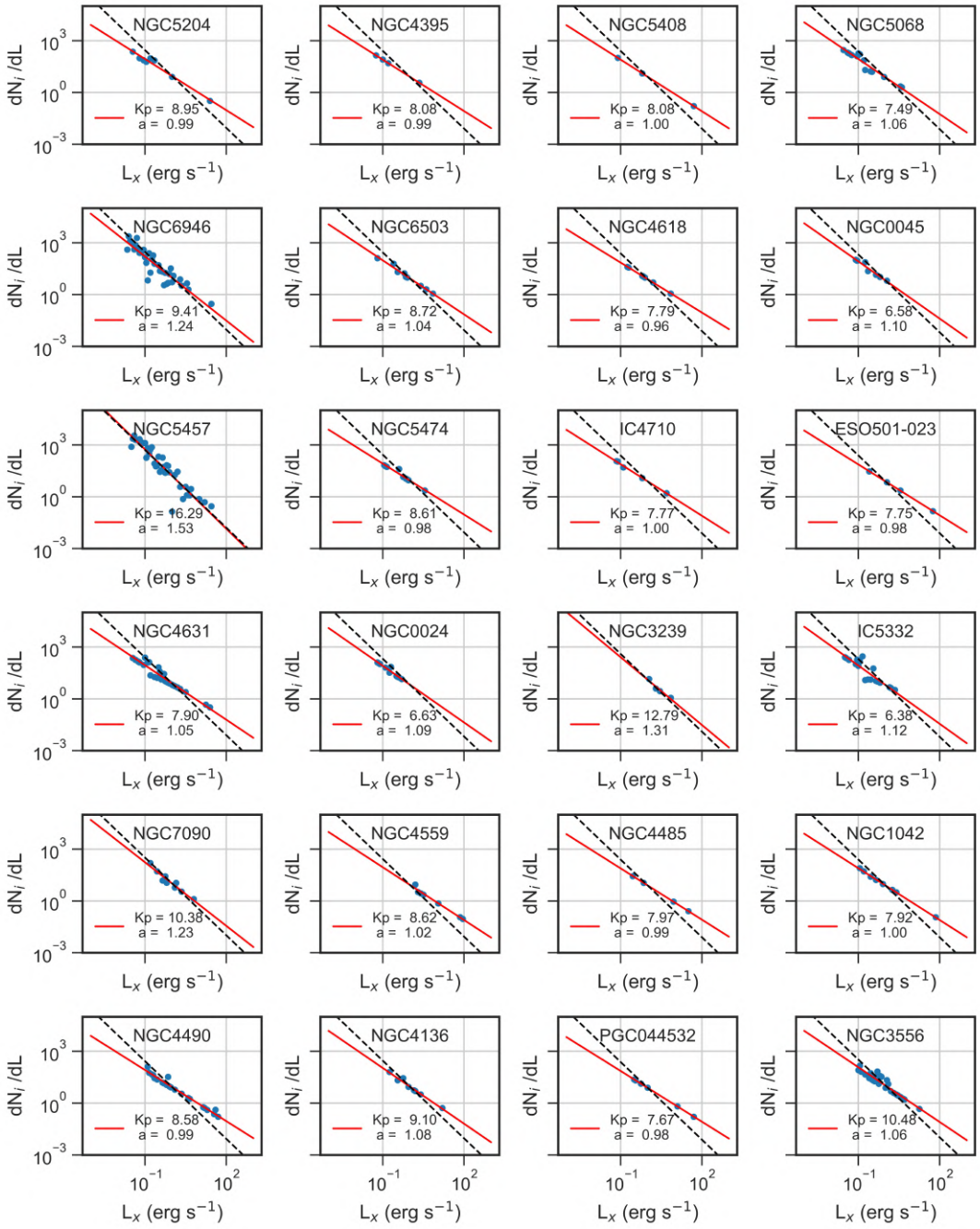

Figure 5.1: XLFs of star-forming galaxies (continued)

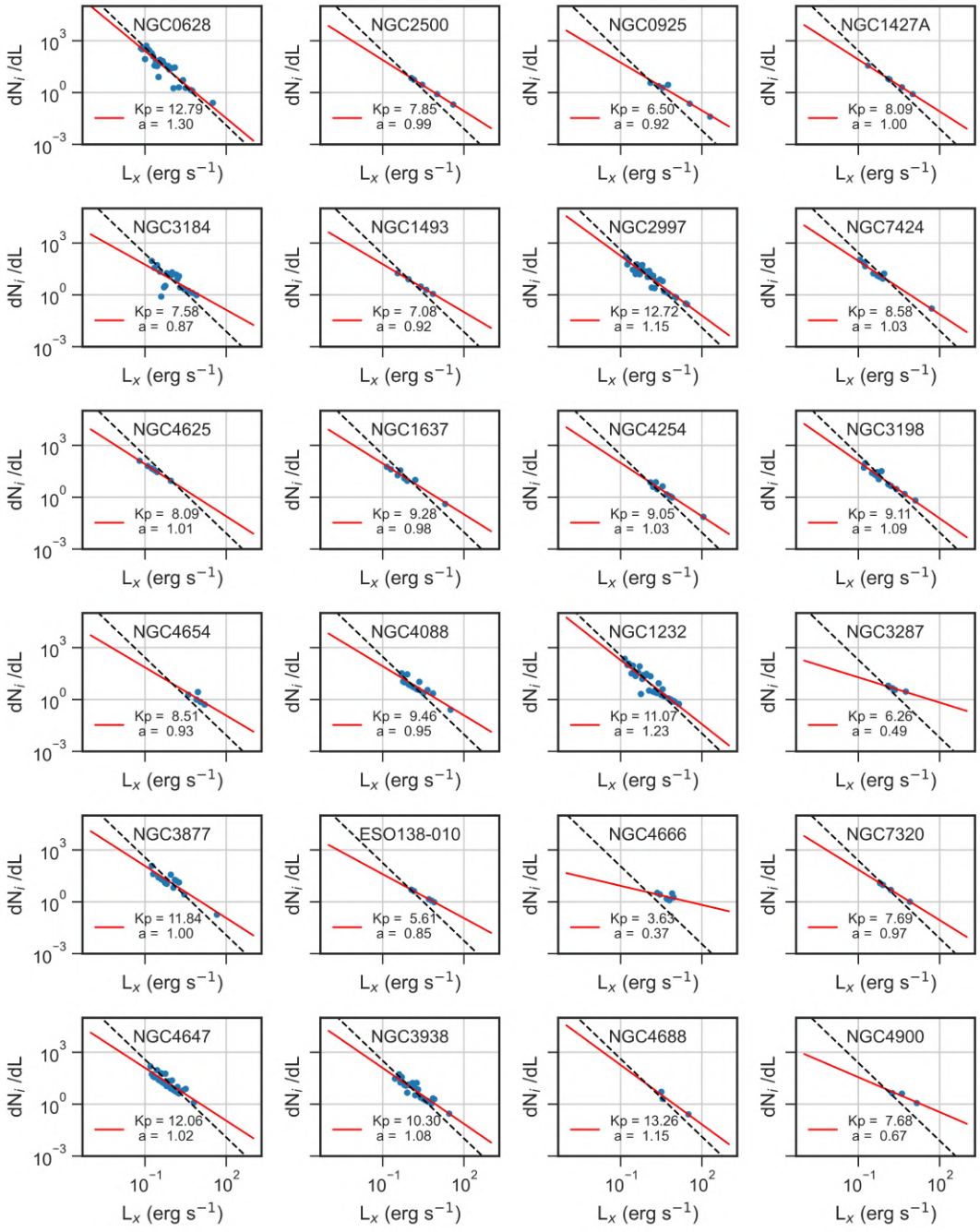

Figure 5.1: XLFs of star-forming galaxies (continued)

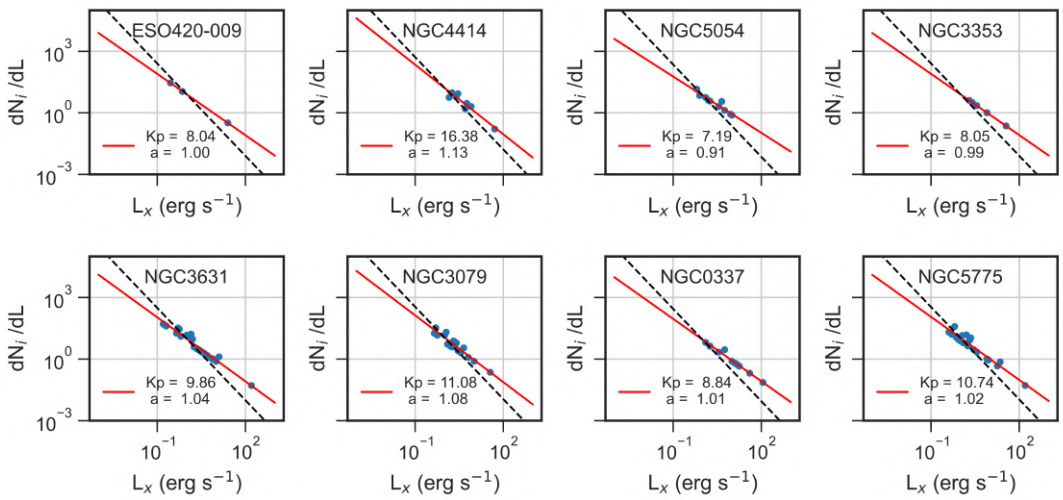

Figure 5.1: XLFs of star-forming galaxies (continued)

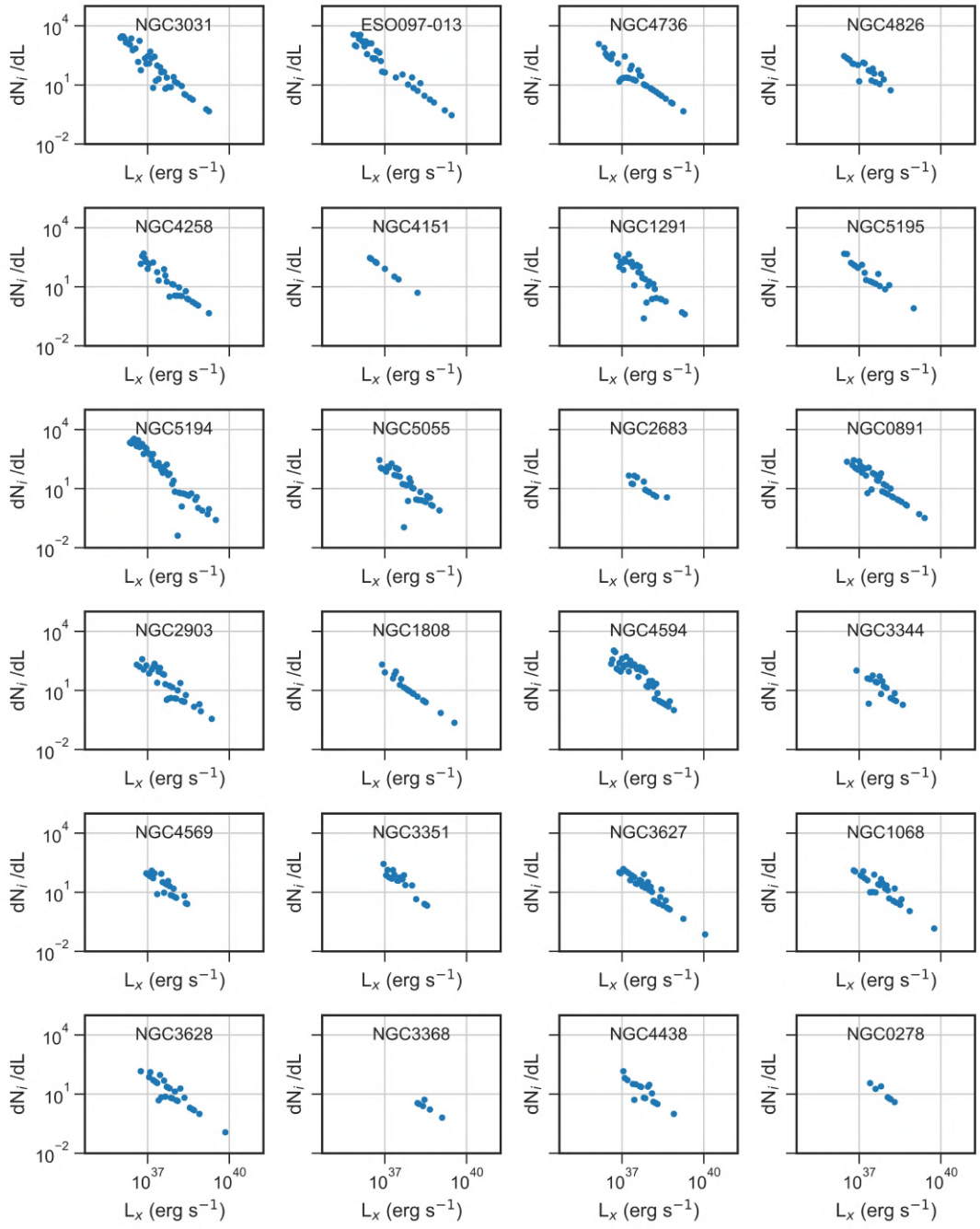

Figure 5.2: XLFs of spiral a,b galaxies

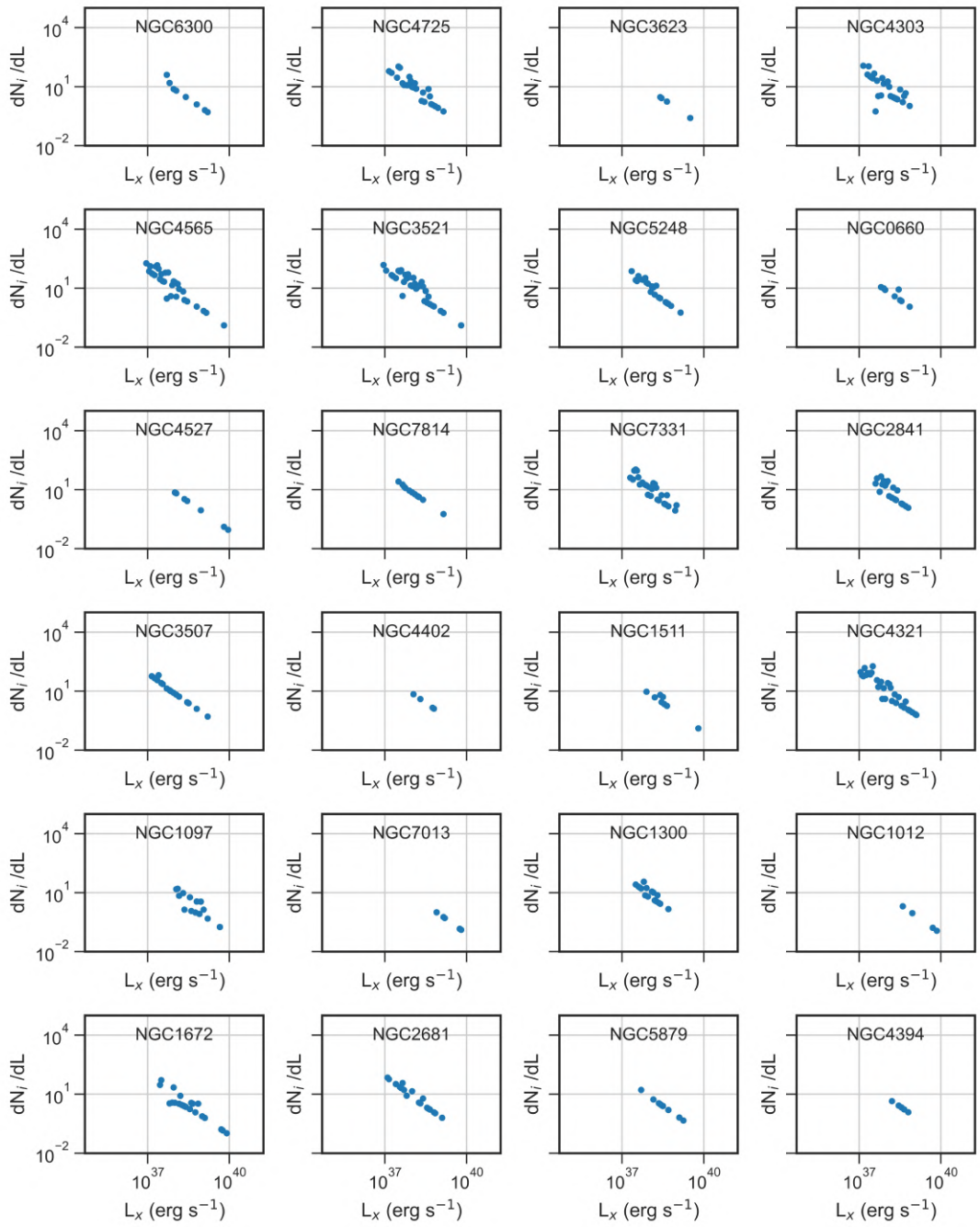

Figure 5.2: XLFs of spiral a,b galaxies (continued)

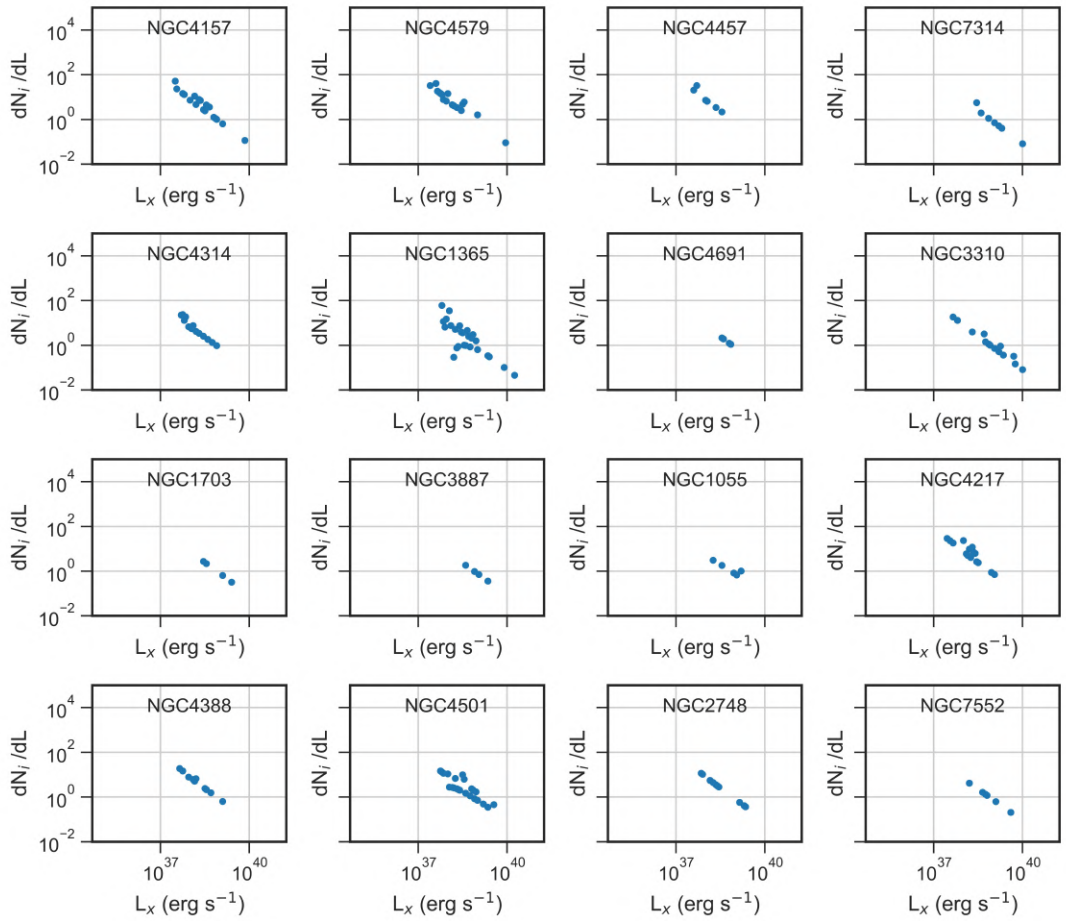

Figure 5.2: XLFs of spiral a,b galaxies (continued)

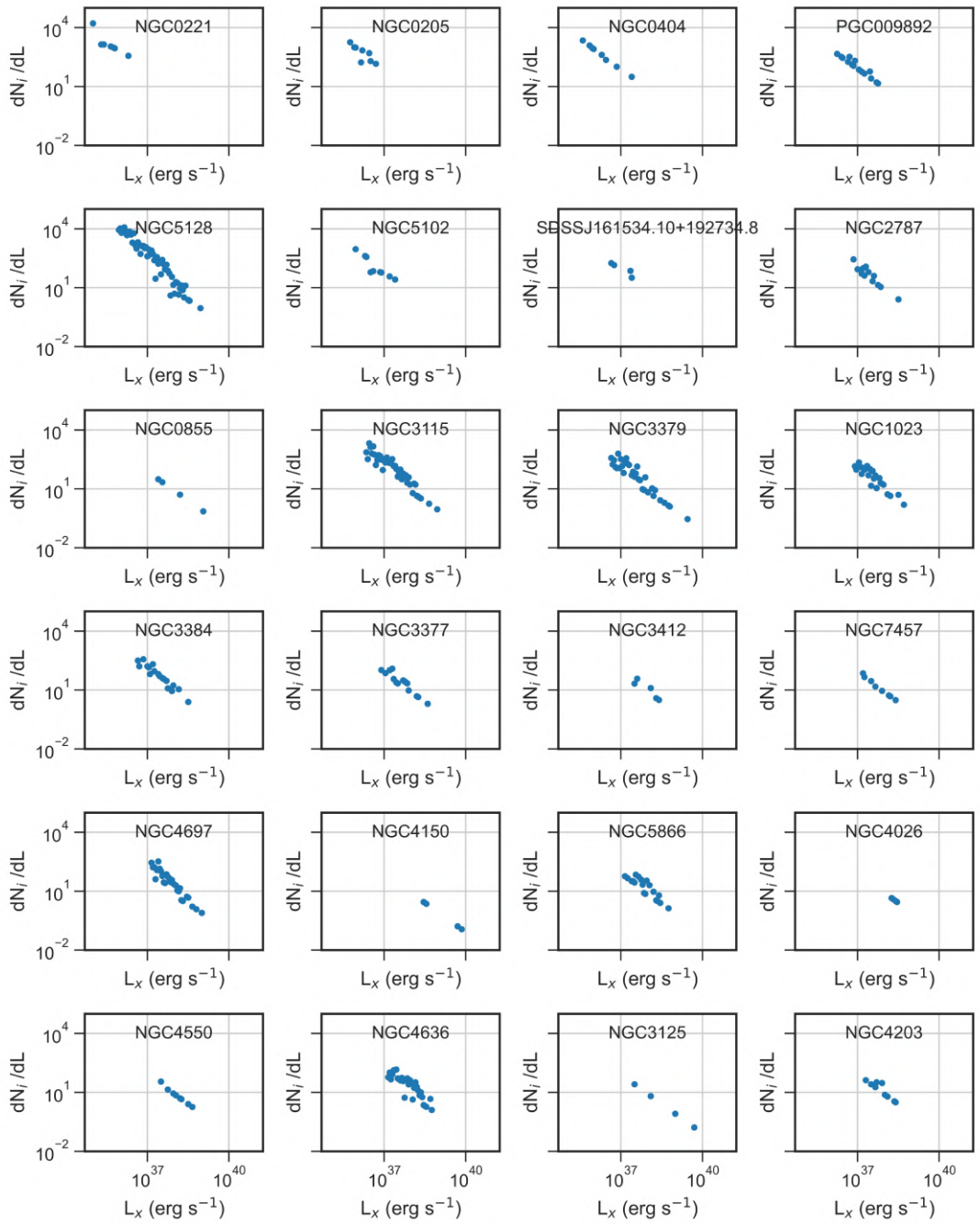

Figure 5.3: XLFs of early type galaxies

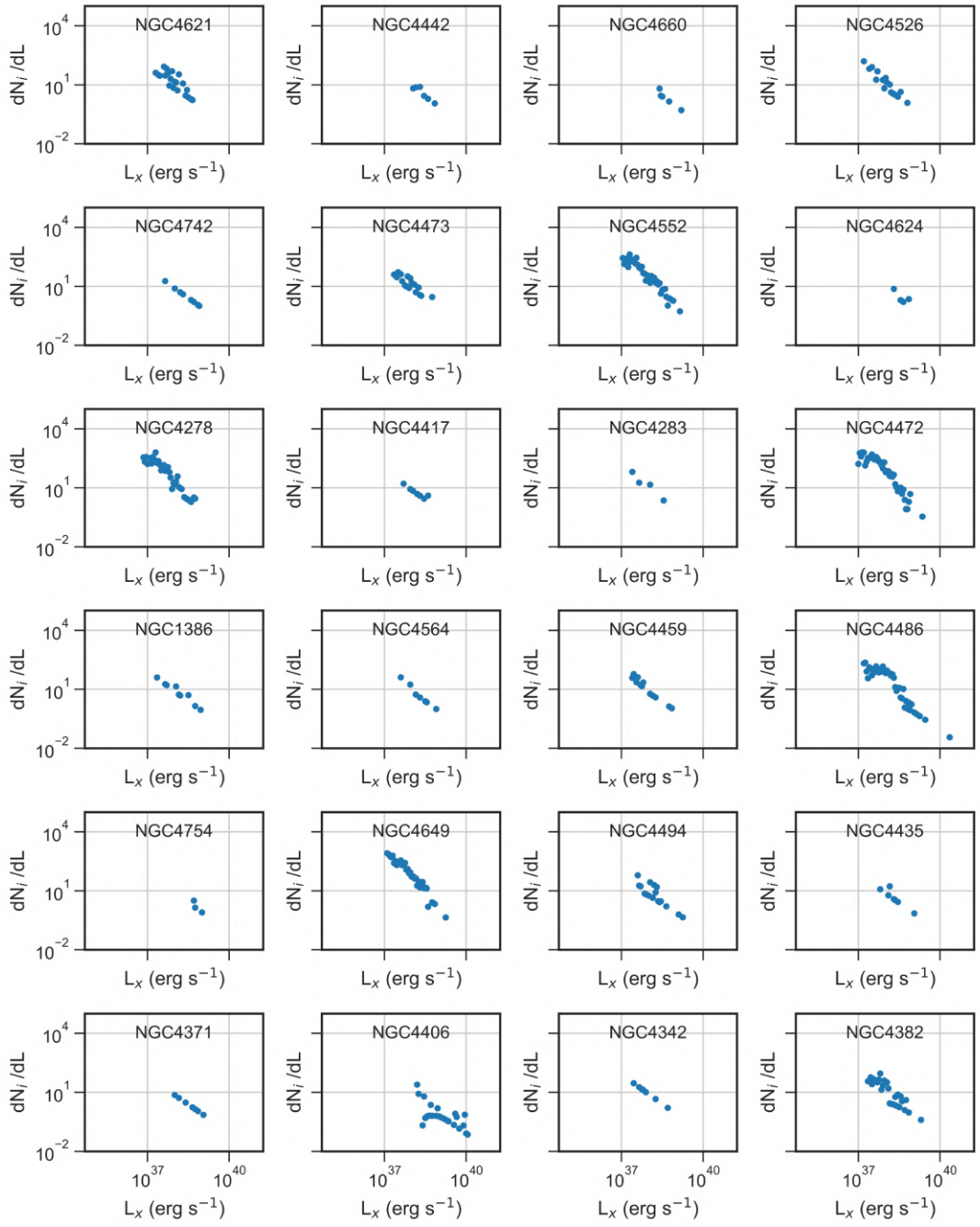

Figure 5.3: XLFs of early type galaxies (continued)

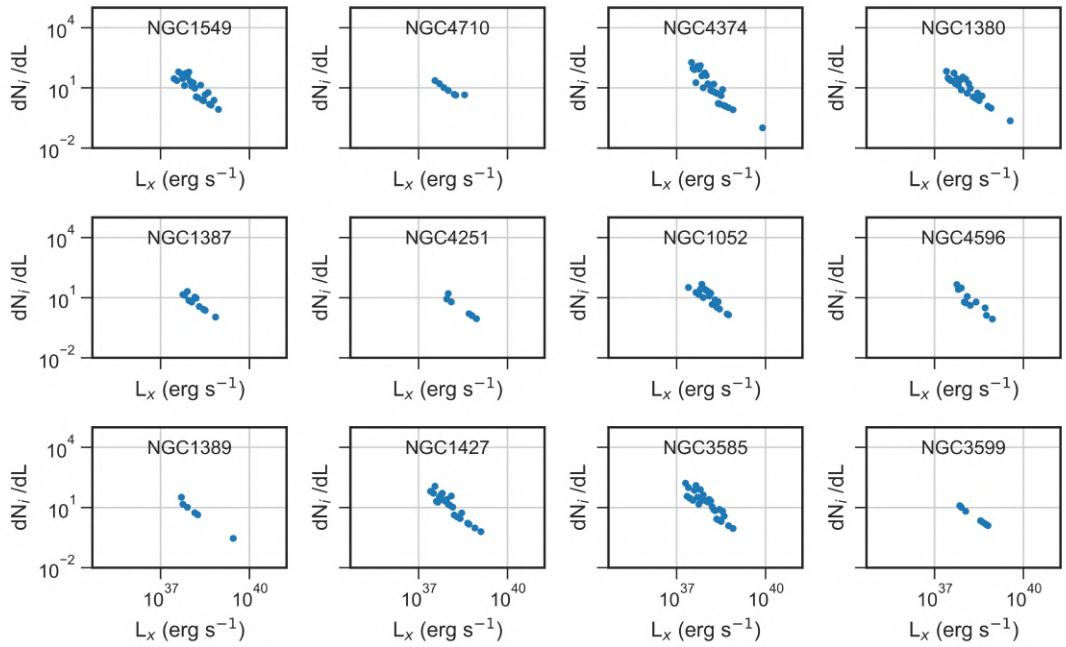

Figure 5.3: XLFs of early type galaxies (continued)

This page intentionally left blank